8-2020

Manufacturing of carbon-based hybrid nanocomposites with engineered functionalities via Laser Ablation Synthesis in Solution (LASiS) techniques

Erick Leonardo Ribeiro
eribeiro@vols.utk.edu

To the Graduate Council:

I am submitting herewith a dissertation written by Erick Leonardo Ribeiro entitled "Manufacturing of carbon-based hybrid nanocomposites with engineered functionalities via Laser Ablation Synthesis in Solution (LASiS) techniques." I have examined the final electronic copy of this dissertation for form and content and recommend that it be accepted in partial fulfillment of the requirements for the degree of Doctor of Philosophy, with a major in Chemical Engineering.

Bamin Khomami, Major Professor

We have read this dissertation and recommend its acceptance:

Bamin Khomami, Dibyendu Mukherjee, Philip D. Rack, Joshua Sangoro, Mahshid Ahmadi

Accepted for the Council:

Dixie L. Thompson

Vice Provost and Dean of the Graduate School

(Original signatures are on file with official student records.)

MANUFACTURING OF CARBON-BASED HYBRID NANOCOMPOSITES WITH ENGINEERED FUNCTIONALITIES *VIA* LASER ABLATION SYNTHESIS IN SOLUTION (LASiS) TECHNIQUES

A Dissertation Presented for the

Doctor of Philosophy

Degree

The University of Tennessee, Knoxville

Erick Leonardo Ribeiro

August 2020

ACKNOWLEDGEMENTS

The years that I have spent as a Ph.D student at the University of Tennessee have been, beyond a shadow of doubt, a life changing experience. It truly amazes me when I look back in time and realize how much I have grown in this period, not only in the professional sphere but also from a personal perspective. As a first-generation college graduate from a humble Brazilian working-class family, the completion of a postgraduate degree represents for me more than an academic achievement, in fact, it is indeed the realization of a dream. To this end, I would like to express my gratitude toward the individuals and institutions that have contributed for the concretization of such accomplishments. Firstly, I would like to thank my primary academic advisor, Dr. Khomami, for the extraordinary guidance, mentorship, and unceasing support throughout this program, in addition for serving as a personal reference in regard to leadership, ethics, and professional standards. I would like to equally thank Dr. Mukherjee for constantly encouraging me through his inspiring passion for science, along with the innumerous contributions from his remarkable work as my Ph.D. co-advisor. Likewise, I would like to express my gratitude toward Prof. Sangoro, Prof. Rack, and Prof. Ahmadi for their willingness to serve as members in this defense committee, and for providing the valuable remarks that have greatly benefited the quality of the work presented here. Additionally, I would like to acknowledge the investment and financial support during the initial four years of this program provided by the Brazilian Ministry of Education through the Science without Borders (SWBs) initiative. Subsequently, I give special thanks to my current and former colleagues; Dr. Sheng Hu, Dr. Ali Davari, Kiman Park, Elijah Davis, and Mahshid Mokhtarnejad, who contributed collectively for the establishment of an extraordinary work environment, which in turn have played an essential role in my progress throughout this program.

I also would like to show my appreciation for my beloved family's never-ending support; such sincere relentless encouragement has given me the strength and motivation to persevere, especially in the face of difficulties. Finally, I would like to immensely give thanks to my mother, Maria do Carmo Ribeiro, for being my best-friend, role-model and

for always endorsing my dreams; her actions have taught me that the combination of honesty, hard-work and perseverance can lead us to marvelous outcomes.

ABSTRACT

Hybrid composite nanomaterials have long been fabricated and extensively used in our daily lives. In the past decades, with rapid development of nanotechnology, these class of material have gained even more attention owing to their outstanding properties which directly results in their prospects to revolutionize technological development in many fields, ranging from medicine to electronics. Nevertheless, for certain applications, including electrochemical energy storage/conversion devices, the chemically inert nature of these materials creates obstacles and thus requires their coupling with other active species. This thesis explores the use of Laser Ablation Synthesis in Solution (LASiS) in tailoring promising strategies and pathways for the synthesis of hybrid nanocomposites in various carbonaceous matrices; more specifically, this dissertation presents (1) synthesis of metal-oxide/ reduced-graphene-oxide hybrid nanocomposites and the rational-design of their structure–property for selective improvements in electrocatalytic/ and or supercapacitive properties, (2) fabrication of nanoparticles within Metal-Organic Frameworks (MOFs) and characterization of their performance as electrocatalysts for Oxygen Reduction Reaction (ORR). For each synthetic route, a comprehensive analysis of reaction pathways, formation mechanisms and structure-property relationship is developed taking into account elemental, structural, physicochemical and morphological characterizations of the final products, setting the ground for the use of LASiS for rational design and synthesis of a wide library of diverse hybrid nanocomposites structures in future.

TABLE OF CONTENTS

vii

LIST OF FIGURES

CHAPTER ONE

MANUFACTURING OF CARBON-BASED NANOCOMPOSITES *VIA* LASER ABLATION SYNTHESIS IN SOLUTION (LASIS)

Introduction

The manufacturing and design of nanostructured materials (NSM) have gained tremendous interested over the past decades; many efforts have been made towards the development of methodologies and synthetic routes to enable the precise control over the physicochemical properties of these structures[1-3]. Quantum effects associated with the nanoscale along with the astonishing surface-to-volume ratio in NSM give this class of materials unique properties when compared to their bulk counterparts, opening the door for a multitude of novel applications in innumerous fields including medicine[4-6], energy[7-10] and electronics[11, 12]. In that scenario, carbon-based nanostructures have been specifically investigated due to unique mechanical, chemical, electrical and thermal properties[13, 14]. Carbon atoms can covalently bond to each other in different hybridization states (sp, sp^2 and sp^3), giving rise to a myriad of allotropes with unique properties including carbon nanotubes, fullerenes, graphene, buckyballs and graphite[15]. This versatility combined with the high abundance and availability of carbon in our planet have encouraged scientists and engineers from different fields of studies to continue the development and search for novel carbon-based materials. A major issue commonly faced, however, is closely related to the chemical inertness of pristine carbon materials; uses in certain sensing, catalytic and electrochemical systems such as energy storage and conversation system, for instance, would require these materials to chemically to interact with other components, which is impractical in many conditions[16, 17]. To address this, some researchers have relied on coupling these carbon-based nanostructures to other components, in particular 0D/1D metal and metal oxide nanomaterials, generating hybrid architectures with enhanced functionalities[18-20]. Nevertheless, the nanoscale in these materials also imposes another

central issue during the fabrication of such structures: in order to decrease the high surface energy arising from the high surface-to-volume ratio, nanomaterials in colloidal solutions commonly undergo agglomeration[21,22]. Other phenomena such as NMs electrostatic interactions, or hydrogen bonding can further exacerbate the agglomeration processes, compromising the novel properties of these materials[23]. As an attempt to tackle the aforementioned challenges, some synthesis routes often opt for surfactant or binding agents as a strategy of surface treatment, nevertheless, these agents can contaminate the active surface of NMs and strongly diminish their performance in practical applications[24]. To this end, relatively inexpensive, environmental-friendly, rapid and yet, high-throughput methods and synthetic routes for the fabrication of functional NSMs architectures, specifically, for carbon-based functional hybrid composites, allowing control over size, morphology and functionalities without the utilization of undesired binding agents/surfactants, are still limited. Laser-based synthesis of nanomaterials is emerging as a great candidate for the design of many hierarchical architectures based on functional NSM. This growing interest is a direct result of the many advances made in the past decade towards the better understanding of the mechanisms that drive the formation of materials under those conditions. The interest in this particular technique stems from the major advantages that the high-energy technique offers; the extreme temperatures and pressures in the interior of the laser-induced plasma plume favors non-equilibrium pathways which are inviable using conventional wet chemistry routes[25]. Although many studies have investigated the synthesis of different NSMs via LASiS[26, 27], reports focused specifically the fabrication of NSM/carbon-based architectures are still elusive.

Carbon-based nanomaterials

The electronic configuration arising from their unique atomic arrangement gives to carbon the ability to form single, double or even triple covalent bonds among themselves or with other elements. These unique sp sp^2 and sp^3 hybridizations states, along with the potential of forming extensive molecular chains through polymerization, allows carbon to co-exist in nature in the form of many different thermodynamically stable arrangements[15].

Diamonds, characterized by a sp^3 hybridization state of carbon, and graphite, a typical sp^2 hybridization, are a few examples of the common forms of carbon allotropes that have been known by humankind for centuries. Despite the long familiarity of our society with carbon-based materials, it was only a few decades ago, with the developments in the field of nanotechnology, that the unique properties of carbon allotropes in the nanoscale started to be investigated[28]. The discovery of graphene in 2004 by Andre Geim and Konstantin Novoselov is up-to-date one of the most significant breakthroughs in the history of carbon materials and has greatly motivated the interest on the research of carbon-based architectures within the international scientific community. Graphene is as an atom-thick two-dimensional (2D) sheet-like material consisting of sp^2 hybridized carbon atoms arranged in a hexagonal (or honeycomb) structure[15]. This specific sp^2 hybridized hexagonal structure can in fact serve as building-blocks to another nanoscale forms of carbon allotropes, such as carbon nanotubes and fullerenes[18]. Moreover, the unique electronic structure of graphene arising from the sp^2 hybridization states along with the typical nanoscale dimensions give rise to its astonishing properties, including high specific surface area (up to 2630 cm^2/g), high intrinsic electron mobility (up to 200,000 cm^2/Vs), high thermal conductivity (up to 5000 W/mK), optical transmittance (up to 97.7%), chemical stability and quantum Hall effect at ambient temperature[18]. Such extraordinary features have triggered the curiosity of scientists and engineers and as a result, inspired the applications of graphene in a myriad of fields, ranging from electronics to biomedical sciences. To this end, the reports and patents on the applications of graphene-based systems have experienced a significant increase in the past decade, with projections indicating the continuance of this rising trend in the next years[29]. Such facts demonstrate that the discovery of graphene has not only revolutionized the technological development in recent years, but it is also expected to contribute significantly to the scientific and technical progress over the next generations. Herein, the interested in exploring the fabrication of functional nanocomposites predominantly consistent of carbon-based nano-architectures arises from the wide-availability of this element in the nature, combined with aforementioned remarkable properties resulting from the unique effects observed in the nanoscale form of these materials.

3

Laser Ablation Synthesis in Solution (LASiS)

Fabrication of NSM are often characterized by techniques based on chemical synthetic routes consisting of multiple stages, many of which involve precise control of synthesis parameters such as reaction temperature and pressure, requiring the use of a sophisticated experimental set-up[2,30]. Additionally, in these methodologies, common coalescence events driven by the characteristic high-surface energy of NSMs, often makes the use of surfactants or capping agents indispensable. To this end, NSMs obtained *via* such routes are frequently; (1) subject to surface contamination, requiring additional purification procedures before their applications in many systems, and (2) produced at the cost of a massive waste generation, creating practical challenges for their sustainable mass production. In this scenario, Laser Ablation Synthesis in Solution (LASiS) have gained increasing attention in the past years, owing mainly to its inherent low-cost, simple and environment friendly experimental operation. The LASiS experimental set-up basically consist of a high-energy laser source in which the generated-beam is aligned toward a liquid-immersed metal target. Commonly, pulsed-laser beams are utilized for the purposes of nanomaterials fabrication *via* LASiS, continuous-wave (CW) laser sources, on the other hand, are generally limited secondary post-processing techniques. During the LASiS procedure, the liquid-immersed metal target is subjected to an incoming high-energy pulsed laser beam; which induces the thermal evaporation of this metal phase, giving rise to a liquid-confined plasma plume. As the resulting plasma-plume expands into the liquid environment, a cavitation bubble is generated, which in turn also expands until, after hundreds of microseconds, it finally collapses. In terms of temporal evolution, the events that lead to the formation of the LASiS-based NSMs are immediately initiated at the emergence of the aforementioned plasma plume. The supersaturation of the metal monomers arising from the drastic conditions in the laser-induced plasma plume (temperatures and pressures close to 10^3 K and 10^6 Pa, respectively) leads to the formation of a secondary-phase through the nucleation phenomena[31-34]. In fact, these extreme conditions can promote non-equilibrium pathways, resulting in the formation of metastable species that are unconceivable through alternative techniques [31]. Following the nucleation

4

events, a growth stage progresses until the just-formed NSMs are ejected into the solution due to the collapse of the cavitation bubble. Once in solution, the stabilization of the LASiS-formed NSMs is obtained by the virtue of mutual repulsive interactions arising from their inherent plasma-generated charge screening effects. This specific mechanism eliminates the requirement for any surfactant or capping agent, thus avoiding the above-mentioned complications associated to their use. Despite the many advantages in the fabrication of NSMs *via* LASiS over conventional methodologies, a few particular drawbacks are also generally associated to this technique. The limited selection in terms of the LASiS target-solution pair, for instance, imposes crucial obstacles in controlling the composition of all LASiS-derived NSMs. To address this issue, Mukherjee et al. recently developed the Laser Ablation Synthesis in Solution-Galvanic Replacement Reaction (LASiS-GRR) technique (*Pat. No.: US 2017/0296997 A1*), characterized by the incorporation of ionic species in the initial liquid solution, which subsequently, can partake chemical-redox pathways at the plasma-liquid interface during the ablation process, giving rise to the formation of NSMs with selected elemental compositions[35].

Application of LASiS-synthesized nanocomposites

The increasing global demand for clean and sustainable energy sources has triggered significant impetus towards the research and development of electrochemical energy storage and conversion systems such as anion exchange membrane fuel cells (AEMFCs) and supercapacitors[36,37]. Although the very elegant operation mechanism inherent of fuel cell devices holds a great promise in terms of sustainable energy conversion, the typical rate-determining and sluggish oxygen reduction reactions (ORR) at the cathode creates the need for highly active and cost-effective catalysts, resulting in obstacles in terms of the large-scale utilization of such devices[38]. On the other hand, supercapacitors, including electrochemical double-layer capacitors (EDLCs) and faradaic supercapacitors (pseudo-capacitors), have concurrently gained prominence due to their superior power densities and longer life cycles comparing with typical batteries, however, despite such remarkable features, these devices are still generally characterized by much lower energy densities than

5

traditional energy storage methodologies, which in turn imposes innumerous constraints in terms of their practical applications[39]. In this regard, the aim of this dissertation is to efficiently apply LASiS in the rational design of nanocomposites predominantly consistent of earth-abundant elements, namely carbon, oxygen and transition metals, for enhancements in the above-mentioned energy storage and conversion systems. To this end, a brief description of the operation mechanism as well as particularities of each application system assessed in this dissertation is presented in the following sections.

Anion Exchange Membrane Fuel Cells (AEMFCs)

Anion exchange membrane fuel cells (AEMFCs) are electrochemical devices that have the ability to convert the chemical energy, from fuel and oxidizers, into electricity, generating water as a by-product[40]. This process is achieved through two semi-redox reactions, the oxygen reduction reaction (ORR) at the cathode (Reaction 1), and the hydrogen oxidation reaction (HOR) at the anode (Reaction 2)[41]. In this configuration, hydrogen gas is supplied in the anode, where it reacts with hydroxyl species generating water and producing four free electrons. The electrons are then transported to the cathode through an external circuit, where along with oxygen, and water they partake in the ORR reaction, generating a hydroxyl radical as the final product[40-41]. As compared to the different variations of fuel cell devices, such as polymer exchange membrane fuel cells, for instance, AEMFCs exhibit a few advantages, including superior reaction kinetics, higher energy efficiency and lower operating temperatures[42]. Despite the great potential of fuel cells towards sustainable energy generation, a few intrinsic limitations of these systems still constrain their widespread utilization.

$$Anode\ Reaction\ (1)\ H_2 + 2OH^- \rightarrow 2H_2O + 2e^-$$

$$Cathode\ Reaction\ (2)\ O_2 + 2H_2O + 4e^- \rightarrow 4OH^-$$

$$Overall\ Cell\ Reaction\ (3)\ 2H_2 + O_2 \rightarrow 2H_2O$$
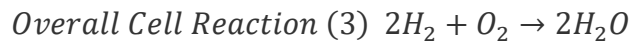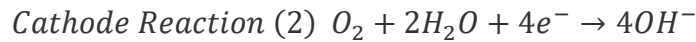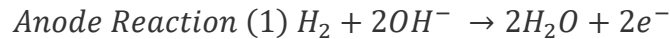
One of the major challenges in such devices is related to the unfavorable thermodynamically conditions, typical of ORR pathways. The sluggish kinetics of this

reaction makes the use of electrocatalysts indispensable for the practical applications of fuel cells[41]. At this stage, materials based on metallic platinum (Pt) are commonly regarded as the most efficient electrocatalysts towards ORR[43, 44], however, the low availability and inherent high-cost of this element along with its low-stability under the common fuel cell operational conditions, impose critical limitations in terms of the large-scale utilization of such materials[45]. To this end, many efforts have been made toward the design of ORR electrocatalysts that can reduce the utilization of Pt, as well as endure the typical fuel-cell operational conditions, while maintaining their overall performance. Fig. 1.1 illustrates the operation mechanism of a typical AEMFCs, the anion exchange membrane between the electrodes serves as a both; separator and ionic conduction media. Additionally, catalyst and gas diffusion layers are present in each one of the electrodes.

Supercapacitors

Supercapacitors (or ultracapacitors) are energy storage devices characterized by much higher energy density than conventional capacitor systems[46]. The increasing attention on these devices stems for their ability to undergo multiple charge-discharge processes at ultrafast rates, resulting in the production of astonishing amounts of power, which in turn could potentially serve as the efficient power-source for many electric-based systems[46]. In fact, the intrinsic power-density of a typical supercapacitor can overcome a state-of-art battery by orders of magnitude, however, in terms of energy-density, the correlation is the opposite; the charge-storage capacity of supercapacitors is typically much inferior to ones observed in batteries[47]. To address this issue, many efforts have been made focusing on the design of novel-materials for enhancements in the overall capacitance of these aforementioned devices. The rational design of materials to compose the electrode of supercapacitors must be, in fact, inspired by the operation mechanism that is intended for the resulting device. In reality, supercapacitors can be classified based on their operational energy-storage mechanism as either electrochemical double layer supercapacitors (EDLCs), or faradaic supercapacitors (commonly denoted as pseudocapacitors)[48]. EDLCs are characterized by the energy-storage *via* the charge separation across a thin interface between an electrolyte and the electrode, this later commonly composed of a highly porous

7
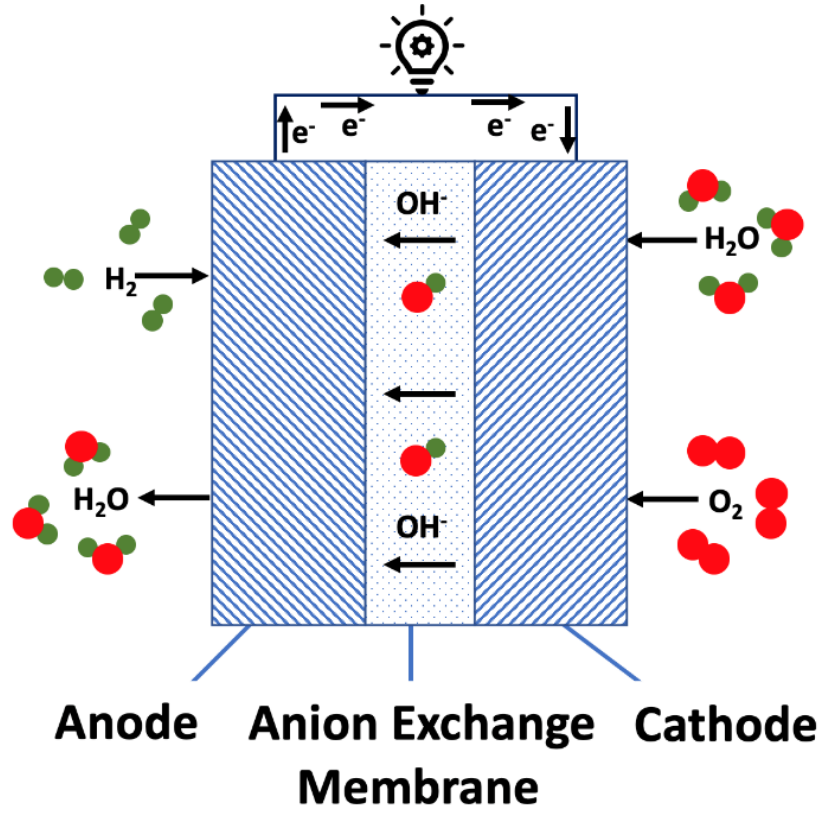
Figure 1.1. Typical AEMFC working principle

material[49, 50]. Faradaic supercapacitors, on the other hand, rely on charge-transfer processes arising from Faradaic reactions between the electrode material and the electrolyte, presenting similarities to batteries from a mechanist operational perspective[51, 52]. Although the design of a supercapacitor is determined by the particularities of its configuration, the use of nanoscale-based materials have demonstrated to greatly enhance the intrinsic features of devices from both classifications[51, 53-55.]

LASiS experimental set-up and methodologies

In terms of experimental set up, the fabrication of all the nanocomposites reported in this dissertation were carried out through a system consisting of a laser-source along with an in-house-built jacketed-reactor cell, as schematically represented in Fig. 1.2. Specifically, Q-switched Nd:YAG pulsed laser source was utilized (Manufacturer: Brilliant Inc.; Model: Brilliant Easy) providing a laser beam with wavelength of 1064 nm and 4ns long pulses with an energy of 330 mJ per pulse at a repetition rate of 10 Hz. The generated beam is focused on the surface of a specific metal target, which in turn is immersed in the selected liquid solution. The metal target-liquid pair is contained in the interior of a sealed stainless steel jacketed-reactor cell, the temperature in the core of the reactor-cell can be precisely determined through a connected-thermostat, and subsequently controlled by means of circulation of heating-exchange fluids (hot or cold water) through the external walls of this compartment. A high damage threshold tested laser window is used to seal reaction-cell, while the two-perforating canals allow selected-purge gases (commonly high-purity N_2) to flow in-and-out of the system.

Dissertation Outline

The main goal of this dissertation is to investigate the fabrication of functional carbon-based hybrid nanocomposites *via* LASiS, specifically focusing on the systematic synthesis–structure–property characterizations and their relationship in the performance of these materials

9

for applications in selected electrochemical energy storage and conversion systems, namely oxygen reduction reaction (ORR) catalysis and faradaic supercapacitive devices. As illustrated in Fig. 1.3, this study proposes two main synthesis routes: (1) Fabrication of reduced graphene-oxide (rGO)/Metal Oxide hybrid nanocomposites and (2) Synthesis of Metal-Organic Framework (MOF) and their functional composites. For each case, this work aims towards the fundamental understanding of the role of solution-phase parameters (*e.g.*, reagents concentration and temperature) along with laser properties in driving the chemistry for the formation process during LASiS. Furthermore, structural, elemental and morphological characterizations are proposed in order to gain a deep understanding of the synthesis–structure–property relationship of the final products.
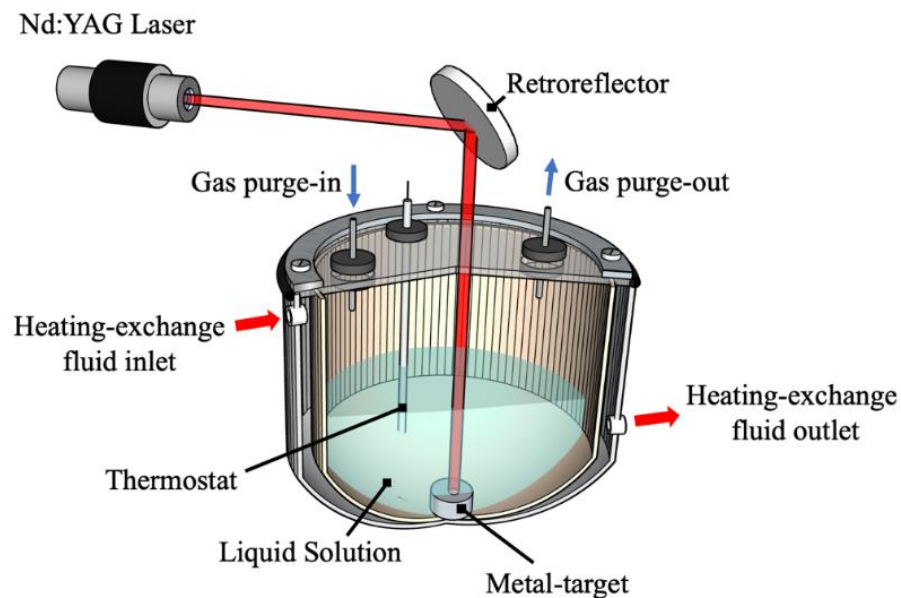
Figure 1.2. Schematic representation of LASiS experimental set-up

Figure 1.3. Outline of the current dissertation

CHAPTER TWO

LASER-INDUCED SYNTHESIS OF ZIF-67: A FACILE APPROACH FOR THE FABRICATION OF CRYSTALLINE MOFS WITH TAILORED SIZE AND GEOMETRY

This chapter is based on the submitted article: *"Laser-induced synthesis of ZIF-67: a facile approach for the fabrication of crystalline MOFs with tailored size and geometry"* by Erick L. Ribeiro, Seyyed Ali Davari, Sheng Hu, Dibyendu Mukherjee, and Bamin Khomami.

Introduction

Metal-Organic Frameworks (MOFs) are a class of crystalline and highly porous hybrid materials self-assembled through the coordination of metal ion nodes to organic linkers[56]. Such networked structures are tunable with near infinite possible combinations of nodes and linkers. Furthermore, MOFs are highly permeable with pore sizes ranging from 0.3 to 10 nm^2 that can provide astonishing porosities (over 90%)[57-58] and surface areas (over 10,000 m^2/gm)[59]. Currently, there exist over 20,000 MOFs that have been characterized[60], and the field is rapidly growing. Thus far, MOFs have been utilized for gas storage[61], fluid separations[62], sensing[63], catalysis[64], luminescence[65], and photovoltaics[66]. Recently, a considerable amount of research efforts have been employed specifically around the synthesis of Zeolitic Imidazolate Frameworks (ZIF), a subclass of MOFs, wherein Co^{2+} or Zn^{2+} ions are bonded through N atoms of imidazole molecules to form unique crystalline-scaffold-like architectures[67]. ZIF morphologies and structures can be tuned by tailoring the synthesis conditions, making it an excellent candidate for a wide range of applications[68-69]. Zinc 2-methylimidazolate (ZIF-8) was first synthesized *via* solvothermal method using dilmethylformamide (DMF) as a solvent[70]. Nonetheless, typical solvothermal techniques require high temperature conditions apart from the inherent need

12

for solvent exchange routes to remove the DMF molecules that can remain confined inside the framework pores due to their large sizes when compared to the apertures for the soldalite (SOD) cage[71]. Cobalt 2-methylimidazolate (ZIF-67) is isostructural with ZIF-8, and by virtue of the similar structure and organic linkers, both crystals have an analogous formation mechanism[72]. Furthermore, in recent years various other techniques such as microwave[73], ultrasound[74], mechanochemical[75], and numerous other fabrication methodologies have also been extensively studied and developed to synthesize ZIF structures. Nevertheless, despite all these efforts, to date very few sustainable, rapid and yet, high-throughput methods have been reported that can facilitate systematic tailoring of ZIF geometries, crystal structures and sizes in the race for the rapid screening of a wide library of MOFs fabrication with desired engineering functionalities.

In fact, for the particular application of MOF synthesis, one can easily envision the potential use of LASiS in tailoring promising strategies and pathways for the synthesis of active metal NPs encaged in MOF structures that can exhibit unique functionalities even under extreme environments. In fact, previous studies have demonstrated that NPs can either serve as nucleation sites for the growth of MOF crystals, or they can be incorporated into the frameworks of the MOF materials[76]. Such encapsulation strategies can be of paramount importance in active and harsh environments where NPs need to be stabilized within the MOF structures to minimize their aggregations while conserving their properties. To this end, Lu et al.[76], have reported the fabrication of a wide range of NPs confined within ZIF-8 crystals that go onto exhibit active catalytic, magnetic and optical properties. Although LASiS provides a remarkably facile and rapid route for such NP encapsulations in MOF, the first step towards making such designer materials demands a fine control on the size and shape of the parent MOF network produced via LASiS. Hence, in this work, we report for the first time LASiS-driven fabrication of ZIF-67 as a model system for MOF designs with tailored size and morphology. The objective of this chapter is to establish a fundamental understanding of the role of solution-phase parameters (e.g., reagents concentration and temperature) along with laser properties in driving the chemistry for the coordination complexation process during LASiS-based MOF formation, as illustrated in Fig. 2.1.
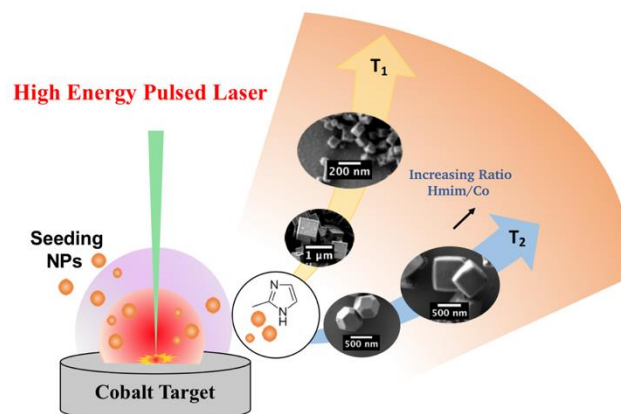
Figure 2.1. Graphical Abstract of the Laser-induced synthesis of ZIF-67

Experimental procedure

Laser-based synthesis of MOF-structures

All chemicals and precursors were purchased from Sigma-Aldrich. Cobalt pellets were obtained from Kurt J. Lesker (99.95% purity, 1/4" diameter×1/4" height). LASiS experiment was performed in the previously discussed reactor-cell. For the synthesis of ZIF-67 structures, the desired amount (60, 120, 180 and 240 mg) of 2-methylimidazole (Hmim) was dissolved in 6 mL of potassium hydroxide solution (3 mol·L-1 KOH in deionized water) before transferring into the LASiS reactor cell. The solutions were maintained at 65 °C during for the entire experiment. The target metal was ablated using an unfocused 1064 nm pulsed Nd-YAG for different ablation times (2-5 min). To ensure complete crystallization of the MOFs, the suspension was maintained at 65 °C for 12 hours. The products were then collected by centrifuging at 4700 rpm for 15 min and decanted after washing two times with methanol. For the sake of comparison, the same procedure was repeated at a different synthesis temperature.

Characterizations

For the detailed morphological characterization of the final products, Scanning electron microscopy (SEM) images were obtained using a Philips XL-30ESEM equipped with an energy dispersive X-ray spectroscopy. Inductively coupled plasma optical emission spectroscopy (ICP-OES) (Perkin Elmer, Optima 4300 DV) was used to measure the metal cobalt concentrations in the solutions for each ablation time, where cobalt chloride salts were used as standards to obtained the calibrations curves. For the detailed crystallographic caractherization of the final products, X-ray diffraction (XRD) was carried out on a Phillips X'Pert-Pro diffractometer equipped with a Cu Ka source at 45 kV and 40 mA. Fourier transformed infrared (FTIR) spectrum was recorded using a Nicolet 6700 FT-IR Spectrometer in the wavenumber range of 400 to 3000 cm^{-1}. For the thermal stability analysis of the final products in different heating atmospheres Thermogravimetric analysis (TGA) was carried out under a Nitrogen atmosphere using a Perkin Elmer Thermal Analyzer at a heating rate of 5 °C min^{-1}.

Results and discussion

Herein we report here the development of a general methodology to synthesize MOF structures using LASiS. Specifically, we present the results that depict our approach in understanding the influence of reaction parameters along with laser properties on the final MOF size and geometry. In doing so, we have studied the synthesis of ZIF-67 under a variety of experimental conditions for LASiS. Firstly, X-Ray Diffraction (XRD) analysis was carried out in order to investigate the purity and crystallinity of the as-synthesized structures. To this end, Fig. 2.2a shows the XRD patterns for the products synthesized using 2 min of ablation with 40 mg·cm^{-3} of Hmim. The diffraction patterns obtained are clearly indexed to the standard ZIF-67 crystal structure patterns. Thus, the formation of a pure-phase material is confirmed *via* comparisons with the simulated patterns. FTIR spectra for the products synthesized under the aforementioned conditions are indicated in Fig. 2.2b. The spectral bands observed at 687 cm^{-1} and 754 cm^{-1} are ascribed to the out-of-plane bending of the Hmim ring, whereas the peaks around 900 cm^{-1} and 1350 cm^{-1} are assigned to the in-plane bending. It is well-known that the band at 1678 cm^{-1} corresponds to the bending of the N-H in the Hmim molecule, while the peak at 1581 cm^{-1} is associated to the N-H vibrations in the same structure. Added to this, the intense peak observed at 1524 cm^{-1} is attributed to the stretching of the Hmim aromatic ring and the bands at 2930 and 3124 cm^{-1} arise from the Hmim aliphatic and aromatic C–H stretching, respectively. Finally, Thermogravimetric analysis (TGA) for the synthesized ZIF sample, shown in Fig. 2.2c, clearly indicates the high thermal stability of these frameworks up to ~380 °C, where a weight loss of approximately 62.5 % is observed. This can be associated to the decomposition of the Hmim molecules in the ZIF-67 crystals, wherein the initial weight loss is attributed to the removal of water and free organic linker molecules that remain trapped inside the framework pores.

A mechanistic picture of the laser-induced MOF formation

Having verified the structural characteristics of the ZIF-67 crystals synthesized here, we turn our attention to elucidate the role of LASiS parameters in tailoring the synthesis of
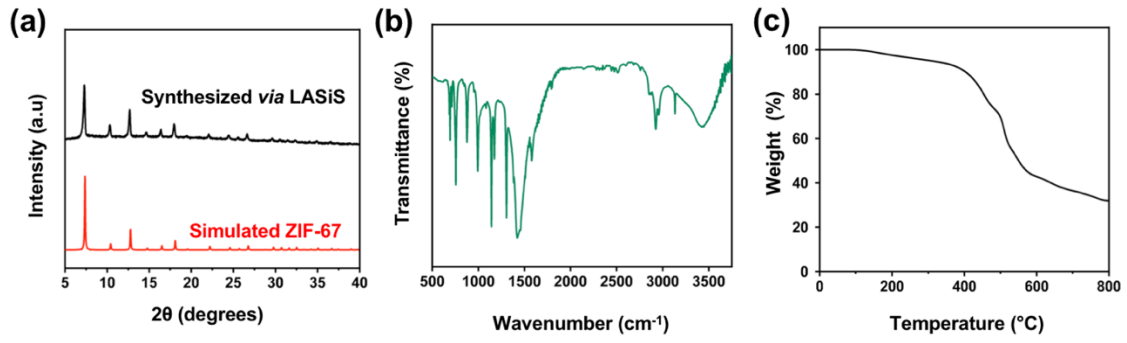
Figure 2.2. (a) XRD pattern (b) FTIR spectra and (c) TGA thermographs of the frameworks synthesized under 2 min of ablation and Hmim concentration of 40 mg/mL

these MOF materials. Herein, we present a detailed mechanistic picture for the governing reaction pathways initiated by the high-energy laser ablation that give rise to the framework formations. To this end, the chemical stages of ZIF-67 production *via* LASiS are illustrated in Fig. 2.3. Initially, the pulsed laser beam thermally vaporizes the metal target in solution to generate a plasma plume with extremely elevated temperatures and pressures (~10^3 K and 10^6 Pa, respectively), which is confined by the surrounding liquid environment. The extreme conditions inside the plasma plume leads to supersaturation of vaporized metal monomers that ultimately nucleate to form the seeding Co nanoparticles (NPs) within an oscillating cavitation bubble formed by the shock waves emanating from the expanding plasma plume. This bubble ultimately collapses causing the NPs to undergo a collisional quenching that subsequently leads to reactions with the solution-phase species at the bubble–liquid interface. During our synthesis technique, the metallic Co NPs nucleated from the ablation process are rapidly oxidized by species present in the aqueous solution resulting in the production of Co^{2+} ions driven by the relative redox potentials: (O_2 / OH^- 0.40 V vs. SHE.) / (Co / Co^{2+} -0.28 V vs. SHE)[34].

In a previous study, Ozturk et al.[32] had proposed the reaction pathways that lead to the formation of ZIF-67 structures. According to the proposed mechanism, the MOF formations consisted of three main reaction steps: (1) coordination of Co^{2+} centers by the Hmim molecules, (2) deprotonation of Hmim, and finally (3) oligomerization by bridging separated Co^{2+} centers via the deprotonated Hmim. Correspondingly, in our methodology, once the initiation of the Co^{2+} ion generations is caused by the oxidation of the LASiS-produced metallic Co NPs, the subsequent solution-phase reaction steps follow the proposed mechanisms as described by Ozturk et al. Based on these considerations and taking into account the LASiS experimental system, it is reasonable to suggest that immediately upon the formation of Co^{2+}, the Hmim molecules present in the solution initiate the coordination of these metal centers giving rise to the deprotonation and subsequently oligomerization that leads to the formation of the framework structures. In terms of the solution-phase, the elevated hydroxyl concentration in the system associated to the initial KOH is necessary considering that the Hmim deprotonation is not feasible at a lower pH due to the high value of its pK_a (pK_a(Hmim) = 14.2)[68].

Effect of organic linker concentration along with ablation time

During the synthesis of these frameworks, both solution-phase and laser parameters are expected to play an important in terms of the final products. A common observation in most previous MOF formation studies have been the obvious role played by the stoichiometric ratio of the organic linkers to metal ions in tailoring the different structural architectures in MOF materials[77-78]. While the linker concentration in our system can be adjusted by simply varying the quantity of Hmim initially injected into the reactor cell, the metal ion concentrations can be accurately regulated by varying the ablation time for a constant laser pulse energy. Based on this approach, taking into consideration the Co concentrations obtained for each ablation time (Fig. 2.4a), the molar ratios of organic linker (Hmim) to metal ion (Cobalt) for each of the LASiS experimental conditions used in this study are represented in Fig. 2.4b. The colored elliptical forms display the respective values/ranges of the Hmim:Co molar ratios obtained for the various combinations of linker concentrations and ablation times. Here, the ratios within a range of 15 units are grouped under the same area. Guided by these ratio maps, the final morphologies of the ZIF frameworks are analyzed using Scanning Electron Microscopy (SEM), as depicted in Figure 4a. The images reveal the well-known cubic crystalline geometry of ZIF-67 with a broad size distribution ranging from several ~10 - 100 nms, depending on the specific combination of the linker concentration and ablation time used. The SEM micrographs clearly show a decreasing trend in the average framework sizes when the concentration of Hmim is increased while maintaining the ablation time constant. For instance, for the 5 min ablation time, the synthesized ZIF structures reach dimensions close to ~300-800 nm range for the lowest Hmim concentration. On the other hand, the frameworks are observed to reach a range of ~75 - 200 nm at the highest Hmim concentrations.

For a more comprehensive analysis, a detailed and quantitative size distributions for the aforesaid experimental conditions are presented in Fig. 2.5b. These histograms indicate good agreements with the visual inspection provided by the SEM images in Fig. 2.5a. In general, the most accepted models for the formation of crystalline structures are based on the hypothesis that these phenomena occur via two separated events: nucleation and growth.
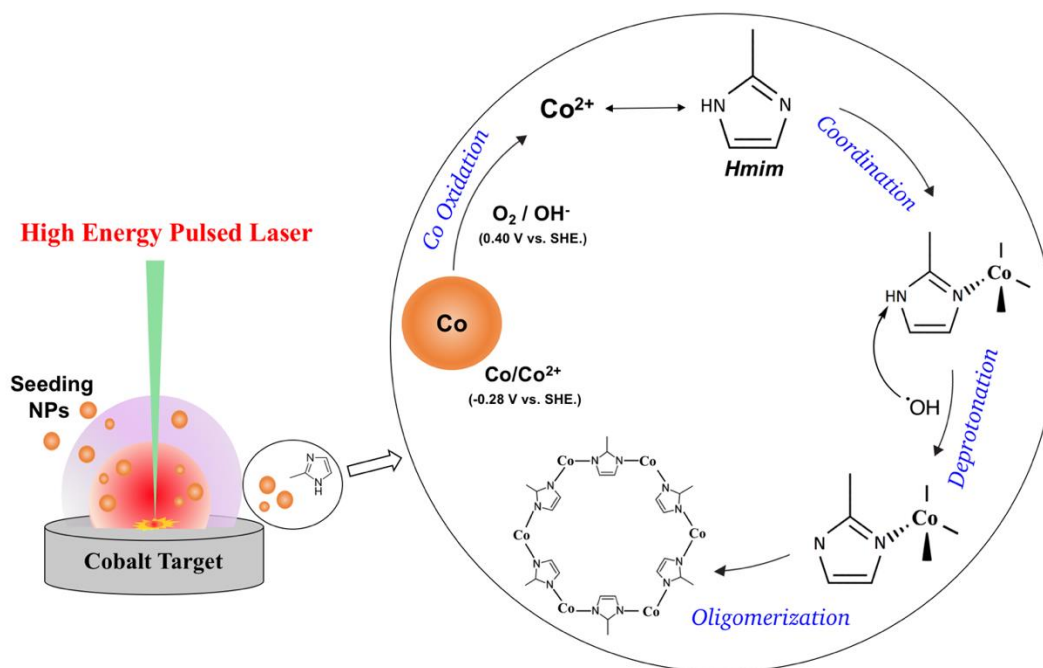
Figure 2.3. Proposed mechanism for the laser-induced ZIF-67 formation
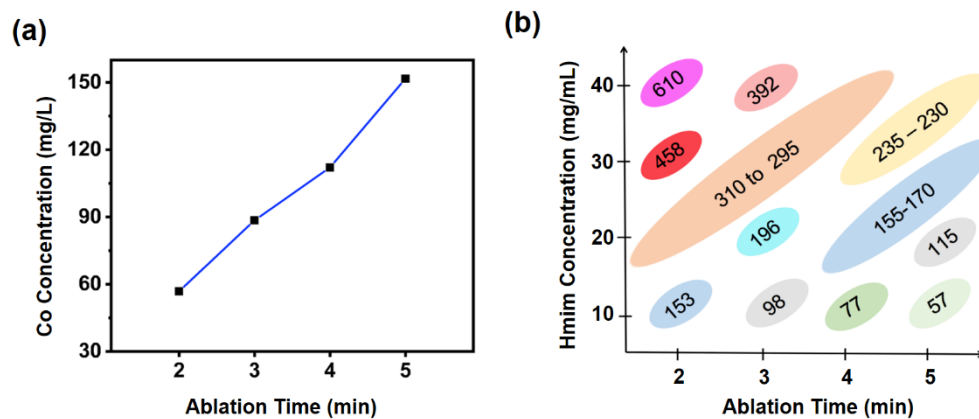
Figure 2.4. (a) ICP-OES Co concentration as a function of ablation time (b) Stochiometric ratio of Hmim to Cobalt for the various experimental conditions used
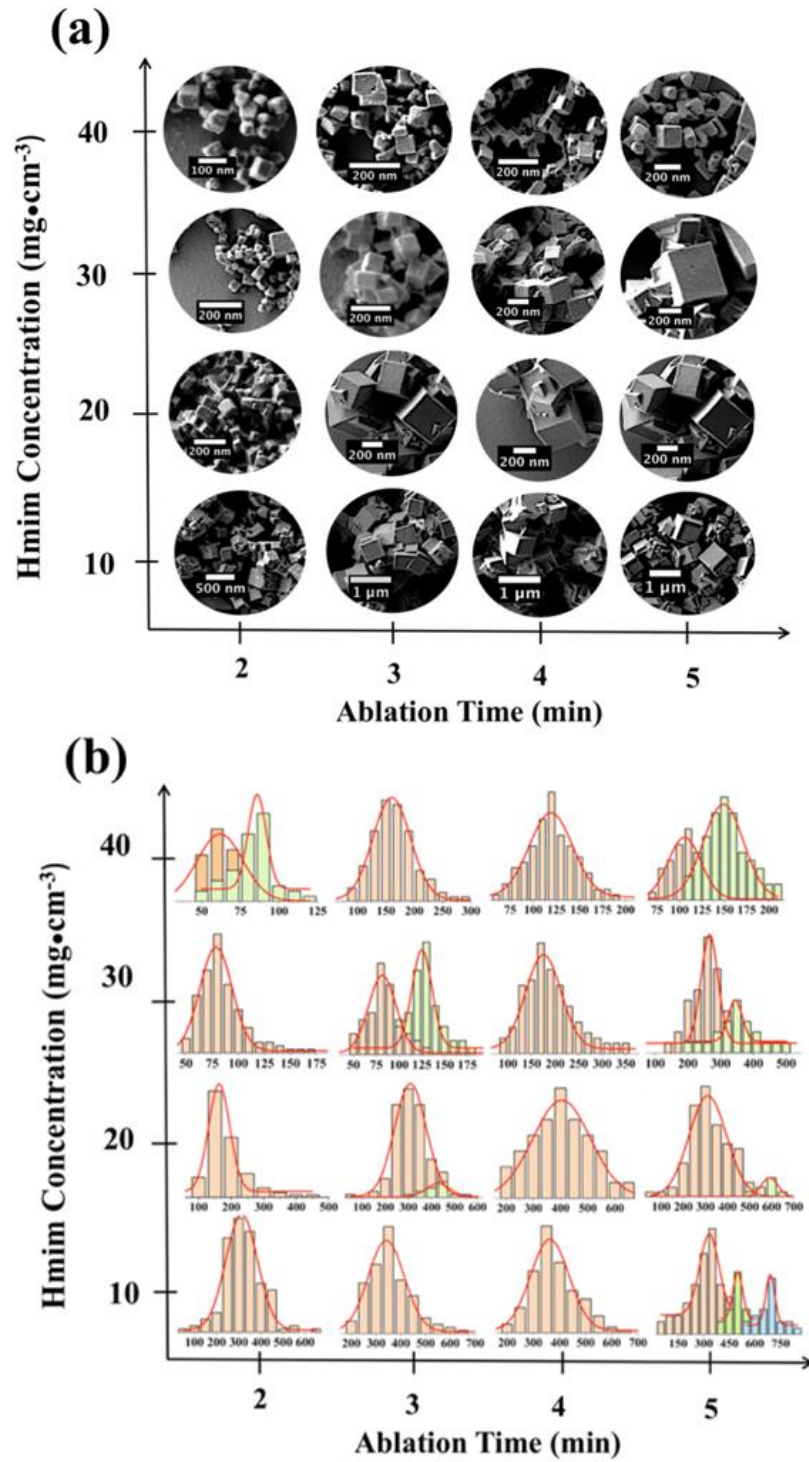
Figure 2.5. (a) SEM micrographs and (b) framework size distribution for the various experimental conditions used

LaMer and coworkers[79-80], specifically proposed the concept of burst nucleation, which has been widely applied for the study of crystal formation since its first publication in 1950. According to LaMer's model, the nucleation events take place immediately when the concentration of monomers in the system reaches a critical supersaturation value *(C$_{max}$)*. At this stage, the burst nucleation occurs forming simultaneously a population of nuclei, bringing the monomers concentration below the supersaturation condition and finally ending the nucleation phenomena. The second stage is characterized by the growth of the just-formed nuclei via diffusion of monomers. Sugimoto *et al.*[81-82] later on developed a simple analysis that extended LaMer's model; the proposed modeling suggests a linear relationship between the population of nuclei *(p$_T$)* and monomers supply rate *(Q)*. For our system *Q* can be interpreted in terms of the oligomerization rate, which is closely related to the deprotonation step.

In summary, for our MOF system we observe two different phenomena: **(I)** increase in the average MOF size while increasing ablation time for a given Hmim concentration, and **(II)** decrease of average size with the increase of the Hmim concentration for a constant ablation time. These observations can be rationalized taking into consideration the above-mentioned LaMer's and Sugimoto's models along with the stoichiometric ratio of Hmim:Co^{2+}. For case **I**, for instance, the higher initial Hmim concentration indicates a greater number of Co^{2+} being coordinated by Hmim molecules. In turn, larger existence of these coordination centers can be associated with an increase in the Hmim deprotonation rates which promotes higher oligomerizations and hence, higher nuclei formations as predicted by Sugimoto's model. This tendency to promote nucleation generates a large number concentration of MOFs with relatively limited sizes; particularly, if one takes into consideration that a vast majority of the Hmim/Co materials will form individual nuclei rather than participate in the growth stage. For the later case **(II)** a more detailed analysis is needed considering that the system becomes more complex as the increase in the concentration of Co^{2+} does not take place instantly, but rather, it occurs step-wise wherein as the ablation time increases. We hypothesize that this constant increase in the metal ion concentration induces the nucleation burst to take place more than once, generating multiple populations of framework that undergo the growth process during different

periods of time, giving also rise, in certain cases, to a multimodal size distribution (Fig. 2.5b). An illustration of the proposed analysis can be seen in Fig. 2.6 as the concentration of monomers in the system rises over time as a result of the ongoing oligomerization process, it eventually reaches a C_{max} value causing the first nucleation event *(Nucleation Event I),* where a population of nuclei in the system *(P_1)* is formed. At this stage the concentration of monomers drops below C_{max} and from this point forward P_1 will undergo the growth process increasing continuously the size of the frameworks over time. During this phase, the oligomerization process has not been completely suppressed, in fact the continuous increase of the metal ion concentration in the system by the constant pulsed laser will enhance the monomers formation process, elevating these species concentration. Once the system reaches the critical supersaturation condition for the second time, *Nucleation Event II* will take place giving rise to P_2. Herein, P_2 will initiate the growth process, although since this process has initiated earlier for P_1 it is natural to expect that at this stage the average framework size of P_1 will greater than P_2 . This sequence will take place N times, until the oligomerization is suppressed by the cease of ablation process resulting in the termination of the cobalt species supply to the system. Hence, one could plausibly argue that the multimodal phenomena are observed at the transition stages in between two unimodal MOF size distributions.

These observations can in fact be analyzed as follows: once the ablation time increases for a given concentration of organic linker (higher Co concentration). we observe appearance of the secondary peaks as the overall size distributions shift to the higher peak modal values. Fig. 2.5b clearly shows the occurrence of bimodal (e.g., 40 mg·cm^{-3}/ 2 min and 30 mg·cm^{-3}/ 3 min cases) and even trimodal size distributions (e.g., 10 mg·cm^{-3}/ 5 min) for certain synthesis conditions. These phenomena can be ascribed to the presence of N populations of frameworks with different size distribution. The expected evolution of the frameworks size distribution in the system is presented in Fig. 2.6, as above mentioned, it can be noted that when the ablation time increases, we can observe the emergence of distinct modal peaks in the overall frameworks size distribution. Nevertheless, as the ablation time continues to increase, it is expected that two or more modal peaks will merge to form one single unimodal size distribution. These phenomena can be justified in terms
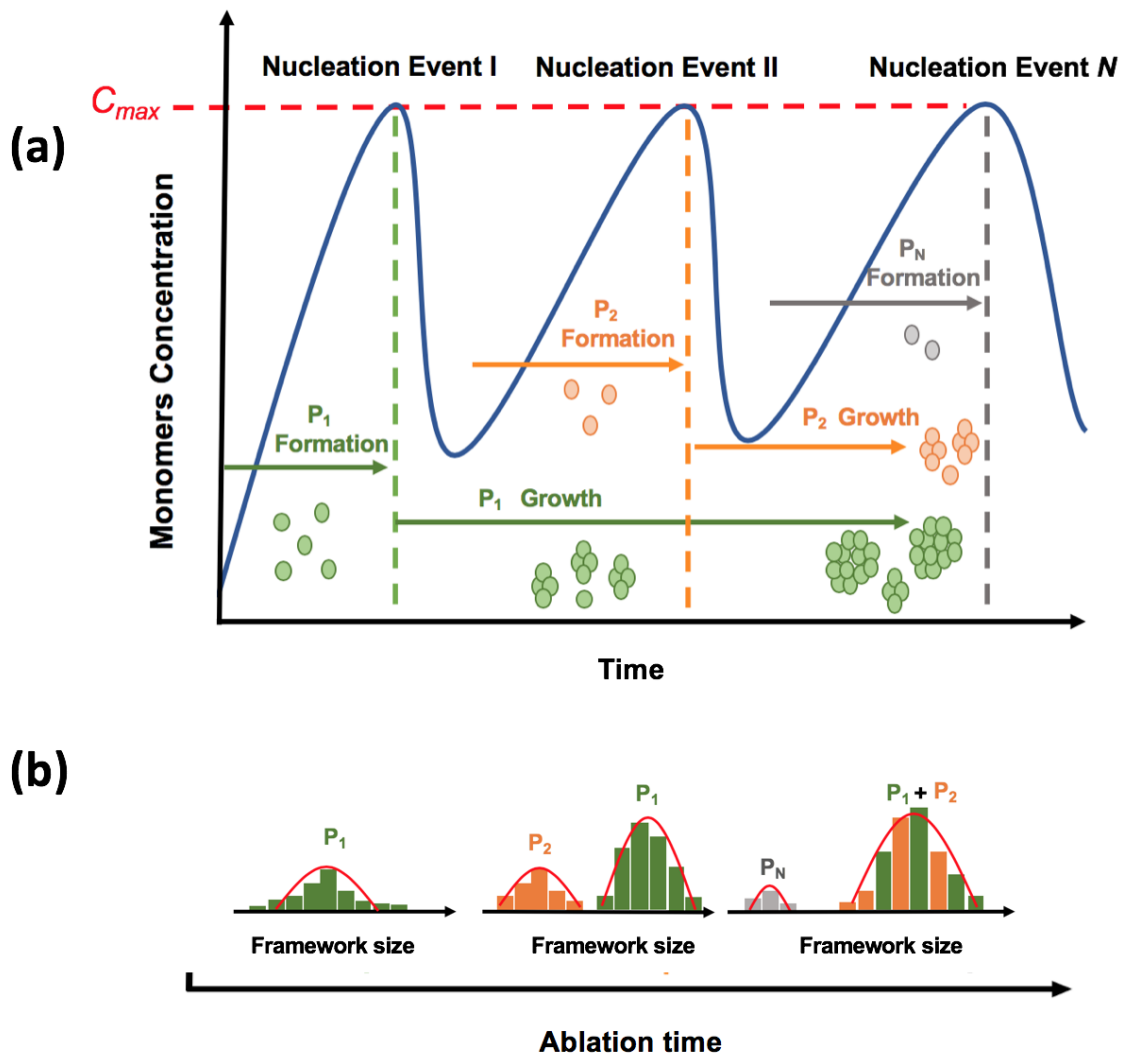
Figure 2.6. (a) Proposed sequence of nucleation events and (b) Expected evolution of the overall framework size distribution as the ablation time increases at a constant Hmim concentration.

of the variation in the frameworks growth rate. The growth of frameworks is driven by the diffusion of monomers from the solution to the frameworks surface, as the dimensions of these species reach greater values the thickness of the boundary layer also increases[82], suppressing the diffusion of monomers and consequently limiting the attachments associated with the growth process. In this regard we can rationalize that the rate of growth in a given population will decay as the MOF species become larger. Therefore, it is not hard to imagine that if enough monomers are available in the solution, smaller MOFs will grow at a faster rate and eventually as the growth rate of the larger frameworks decreases, all the MOF species will reach similar dimensions leading to a unimodal size distribution.

Effect of the solution temperature

In our effort to investigate the influence of synthesis temperatures on the LASiS-based MOF fabrications, here we analyze the formation of the frameworks under the identical set of experimental conditions as before, but for a different synthesis temperature. We study the final MOF products for different Hmim concentrations using 5 min as the ablation time, while maintaining the system at 25 °C. The results, as indicated in Fig. 2.7, show a gradual decrease in the average framework size (observed from inset size distributions) as the concentration of Hmim increases. These findings also corroborate our results obtained in the previous sections for the synthesis carried out at 65 °C. However, when carefully inspected, the products formed at lower temperature (25 °C) show larger average framework sizes when compare to the sizes obtained for the same set of previous experimental conditions at the higher temperature (65 °C). These observations clearly support the strong temperature dependence of the nucleation rates, and, as discussed earlier, a higher nucleation rate yields greater number of MOF structures with lower average sizes. The results at the lower temperature LASiS also indicate a distinct change in the MOF morphologies with increasing linker Hmim concentrations. Thus, for the lowest Hmim concentration, the MOF frameworks generate a truncated rhombic dodecahedron morphology with {100} and {110} faces expressed (Fig. 2.7a). On the other hand, as the Hmim concentration increased, the frameworks exhibit progressively smaller cubic morphologies with the {100} faces expressed (Fig. 2.7b-d). The synthesis temperature can

25

modify the attachment energy and hence, the rates of attachment during crystallization, which in turn, have a strong relationship to the morphology of the final crystal structure. This morphological control of the frameworks presents a remarkable advantage for MOF synthesis. It becomes immediately apparent that by adjusting the morphology it is possible to modify the orientation of the pore apertures and functional groups, thereby regulating their accessibility and hence, the degree of interaction with the species of interest.

Conclusions

We have presented here a systematic study of LASiS-based synthesis of MOF structures, specifically using ZIF-67 as the model MOF system. Our results provide fundamental insights into the mechanistic roles of solution-phase parameters and laser properties, heretofore not investigated in detail for laser-induced MOF formation routes. Specifically, we proposed a sequence of reaction pathways during the LASiS technique that is initiated by high-energy laser-driven ablation of a metal target resulting in the nucleation of metal NPs that subsequently undergo solution-phase oxidation to generate Co^{2+} ions. The large population of the metal ions coordinates with active sites on the Hmim molecules in the solution-phase that is immediately followed by the Hmim deprotonation and subsequent oligomerization reactions resulting in the final MOF crystal nucleation and growth phenomena. The organic linker to metal ion stoichiometric ratio, as controlled by the initial Hmim concentrations and ablation time for the LASiS technique, have been shown to bear substantial influence on the sizes of the framework. These results indicate that a higher Hmim concentration under a given laser ablation time yielded MOFs with smaller average sizes, while an increase in the ablation time using a constant Hmim concentration produced structures with larger average sizes. These findings have been rationalized based on the deprotonation rates; specifically, a higher Hmim to Co^{2+} stoichiometric ratio accelerates the Hmim deprotonation, inducing an enhanced oligomerization and hence, nucleation rates. We hypothesize that the enhancement in the nucleation rate is achieved at the expense of the framework sizes formed, while bearing in mind that most of the Hmim/Co centers participate in the formation of new nuclei and only a limited amount of material contributes

26

to the growth of existing MOF structures. We also investigated the role of the synthesis temperature during the LASiS process on the MOF formations. Our results indicate that the MOF morphology can be tailored by optimizing the temperature for a given set of experimental parameters during LASiS via modulating the attachment energy and rates of attachment during the MOF crystallization process. In summary, the present study lays the groundwork for LASiS as a facile, environmental-friendly and efficient technique for the rational design and synthesis of a wide library of diverse MOF structures in future.

CHAPTER THREE

FACILE MANUFACTURING OF MOF-DERIVED PLATINUM-COBALT NANOCOMPOSITES IN CARBONACEOUS MATRICES AS HIGH PERFORMING OXYGEN REDUCTION REACTION (ORR) ELECTROCATALYST *VIA* LASIS IN TANDEM WITH GALVANIC REPLACEMENT REACTION (LASIS-GRR)

This chapter is based on the submitted article: "*Facile manufacturing of MOF-derived PtCo/Co$_3$O$_4$ nanocomposites in carbonaceous matrices as high-performance Oxygen Reduction Reaction (ORR) electrocatalysts via Laser Ablation Synthesis in Solution-Galvanic Replacement Reaction (LASiS-GRR)*" by Erick L. Ribeiro, Elijah M. Davis, Mahshid Mokhtarnejad, Sheng Hu, Dibyendu Mukherjee, and Bamin Khomami.

Introduction

Renewable energy research and development has become a central theme in our dynamic and rapidly expanding societies. The continuous growth in the global economy combined with a constant increase of the population mandates more than ever, the development of low-cost, efficient, yet environment-friendly energy alternatives that can empower the global anthropogenic technological developments over the next decades[83-85]. In this scenario, anion exchange membrane fuel cells (AEMFCs) have gained tremendous attention owing to their ability to efficiently convert chemical energy, from fuels and oxidizers, into electrical energy through a clean and elegant process, with water-vapor as a byproduct[4-5]. The feasibility of these devices, however, relies on the utilization of highly active and stable catalysts that can accelerate the thermodynamically unfavorable Oxygen Reduction Reaction (ORR) at the fuel cell cathode[86-87]. Traditionally, Pt-rich materials have been employed as ORR electrocatalysts due to their superior activity when compared to other catalysts; nonetheless, the low-stability, scarcity and the overwhelming cost of

28

such materials impose serious obstacles for their large-scale utilization, both from an economic and supply chain perspective[88-89]. To this end, many efforts have been made toward the design of advanced-materials that can reduce Pt usage while maintaining superior electrocatalytic performance and high stability[90-93]. MOF structures are, on the other hand, one of the most promising classes of materials known to date for the design of advanced functional composites, owing to their versatility arising from their countless unique chemical arrangements, as well as their crystalline nature and remarkable porosity[94-98]. As such, the understanding gained through the laser-induced synthesis of MOFs, along with our previous reports on the LASiS-based synthesis of intermetallic electrocatalytic nanoparticles, have paved the way and revealed the tremendous potential of LASiS for the design of MOF-derived functional NCs. Herein, we explore coupling LASiS in tandem with Galvanic Replacement Reaction (LASiS-GRR) methodology to take advantage of the ensuing coordination-complexation chemistry during the laser-induced MOF synthesis route to generate a series of catalytic intermetallic nanoparticles encapsulated within the MOF structure. In turn, the highly robust and porous MOF scaffolds enable post-processing treatments to produce highly active electrocatalytic NCs. Specifically, in this report we present a methodology for the synthesis of Pt-Co bimetallic nanoparticles that are readily encapsulated within a ZIF-67 structure. As illustrated in Fig 3.1, this chapter is aimed toward the investigation of LASiS-based synthetic routes on the fabrication of MOF-derived nanocomposites with low Pt-loading, yet, outstanding ORR performance.

Experimental procedure

Laser-based synthesis of MOF-derived nanocomposites

All chemicals and precursors were acquired from Sigma-Aldrich and Cobalt pellets were purchased from Kurt J. Lesker Company (95% purity, 1/4" diameter×1/4" height). LASiS experiments were performed in an in-house built laser ablation reactor-cell, as described in the previous chapters. For the synthesis of Pt-rich nanoparticles encapsulated in ZIF-67 structures, three different concentrations of potassium tetrachloroplatinate (II) (K_2PtCl_4) (>99.9%) K_2PtCl_4 solutions (namely 63, 95 and 125 mg·L^{-1}) were prepared by the
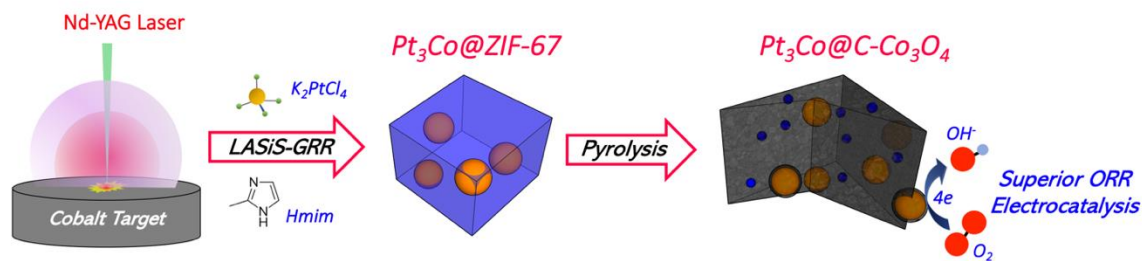
Figure 3.1. Graphical abstract of the facile manufacturing of MOF-derived Platinum-Cobalt nanocomposites in carbonaceous matrices as high-performing Oxygen Reduction Reaction (ORR) electrocatalysts *via* LASiS in tandem with Galvanic Replacement Reaction (LASiS-GRR).

dissolution of a given amount of the salt in 40 mL of potassium hydroxide solution (3 mol·L^{-1} KOH in deionized water). Thereafter, 1.6 g of 2-methylimidazole (Hmim) was added to each solution and stirred until complete dissolution. The LASiS procedure was initiated by transferring the desired solution into the reactor cell through the injection unit, followed by the ablation of the Co metal target using the unfocused 1064 nm pulsed Nd-YAG laserfor 15 min. To ensure complete crystallization of the MOFs, the suspension was left aging for 24 hours. The products were then collected by centrifuging at 4700 rpm for 15 min and decanted after washing two times with methanol, yielding samples 125-Pt$_3$Co@ZIF-67, 95-Pt$_3$Co@ZIF-67 and 63-Pt$_3$Co@ZIF-67 for the initial concentrations of the K$_2$PtCl$_4$ solutions of 63, 95 and 125 mg·L^{-1}, respectively. For the sake of comparison, a Pt-free NC (ZIF-67) was prepared by the same procedure, excluding the addition of K$_2$PtCl$_4$.

Post-treatments: For the synthesis of all bimetallic NCs, the products from the methanol wash were pyrolyzed at 750 °C under N$_2$ atmosphere for 3 hours. Finally, the samples were cooled down at room temperature for approximately 6 hours, generating the 125-Pt$_3$Co@C-Co$_3$O$_4$, 95- Pt$_3$Co@C-Co$_3$O$_4$, 63- Pt$_3$Co@C-Co$_3$O$_4$ and C-Co$_3$O$_4$ NCs respectively from the pyrolysis of 125-Pt$_3$Co@ZIF-67, 95-Pt$_3$Co@ZIF-67 and 63-Pt$_3$Co@ZIF-67, and ZIF-67.

Characterizations

Scanning electron microscopy (SEM) images were obtained using a Philips XL-30ESEM capable of performing energy dispersive X-ray spectroscopy. Inductively coupled plasma optical emission spectroscopy (ICP-OES) (Perkin Elmer, Optima 4300 DV) was used to measure the Pt concentrations for each NC, where K$_2$PtCl$_4$ solutions were used as standards for the calibrations. X-ray diffraction (XRD) was carried out on a Phillips X'Pert-Pro diffractometer equipped with a Cu Ka source at 45 kV and 40 mA. A Zeiss Libra 200MC monochrome transmission electron microscope (TEM) was used with an accelerating voltage of 200 kV for regular TEM for sample characterizations in tandem with a high-resolution transmission electron microscopy (HRTEM). Elemental mappings were obtained from electron energy loss spectroscopy (EELS) analysis with a resolution of

0.1 eV measured at full width of half maximum (FWHM) of zero-loss peak in vacuum. Raman spectra were obtained using an NT-MDT NTEGRA instrument with a 532 nm laser beam.

Electrochemical tests

The rotating disk electrode (RDE) setup was purchased from Pine instruments, LLC. A conventional, three-compartment electrochemical cell comprising a saturated double junction Ag/AgCl electrode as the reference electrode, and a platinum coil as the counter electrode were used for all the EC tests. All potentials in this work are reported in reference to the reference hydrogen electrode (RHE).

Oxygen Reduction Reaction (ORR) tests

A glassy carbon RDE with a diameter of 5 mm was used as the working electrode, 1 M KOH solution was used as the electrolyte. 20% Pt/C from BASF was used as the standard catalyst for all comparisons. For preparing the working electrode, 2 mg of the synthesized hybrid NCs (HNCs) after the above-mentioned post-treatments were suspended in 0.5 mL ethanol and 25 µL of 5 wt% Nafion solution (Sigma-Aldrich, density 0.874 g·mL^{-1}) *via* 30 min of ultrasonication. Thereafter, 25 µL of the prepared catalyst ink was coated on the RDE where the catalyst loading density was calculated to be ~30 µg·cm^{-2}. For all ORR experiments, stable voltammogram curves were recorded after scanning for 15 cycles in the corresponding potential region. The dynamics of the electron transfer process in ORR were analyzed through the rotating disk voltammetry (RDV) at different speeds based on the Koutecky–Levich (KL) equation:

$$\frac{1}{J} = \frac{1}{J_K} + \frac{1}{J_L} = \frac{1}{J_K} + \frac{1}{B\omega^{\frac{1}{2}}}$$

$$B = 0.62nFC_0D_0^{2/3}v^{-1/6}$$

Where J, J_K, and J_L are the measured, kinetic and diffusion limiting current densities respectively, n is the electron transfer number, F is the Faraday constant, C_0 and D_0 are the dissolved O_2 concentration the O_2 diffusion coefficient in the electrolyte respectively, v is the kinematic viscosity of the electrolyte, ω is the angular rotation of the electrode and B is the Levich constant. All Tafel plots were generated using the kinetic current J_K as determined from:

$$J_K = \frac{J \times J_L}{J_L - J}$$

Cyclic Voltammetry (CV) measurements

The cyclic voltammetry (CV) profiles were obtained between 0.05 V and 1.10 V *vs* RHE at a scan rate of 100 mV·s^{-1}, using a N_2-saturated 1 M KOH solution as the electrolyte. The Pt-phase electrochemical active surface area (ECSA) of each sample was determined by integrating the charges in the hydrogen under potential desorption (H_{upd}) region from each corresponding CV, where a pseudo-capacity of 220 μC·cm^{-2} was assumed for the correction of the double layer current.

Results and discussion

Structural and morphological characterizations of the LASiS-based nanocomposites

$Pt_3Co@C-Co_3O_4$ NCs were synthesized *via* LASiS-GRR using three different K_2PtCl_4 salt concentrations, namely 125, 95, and 63 mg·L^{-1}, yielding the 125-$Pt_3Co@C-Co_3O_4$, 95-$Pt_3Co@C-Co_3O_4$, and 65-$Pt_3Co@C-Co_3O_4$ NCs respectively. The SEM micrograph of sample 125-$Pt_3Co@ZIF$-67 (before pyrolysis) is shown in Fig. 3.2a. The SEM image depicts formation of interconnected cubic ZIF-67 structures of a few hundred nanometer size. These MOF cubical structures are also evidenced in the TEM images for the same sample (see Fig. 3.2b). A higher-magnification image, Fig. 3.2c, of the 125- $Pt_3Co@ZIF67$ products is shown in the micrograph obtained *via* High-Resolution TEM (HRTEM). Fig. 3.2c clearly shows formation of a dense population of spherical-shaped nanoparticles

33

embedded in the ZIF-67 matrix, which indicated complete incorporation of the LASiS-derived nanoparticles within the concurrently formed MOF structures. The subsequent pyrolysis of this sample leads to formation of a hierarchical structure with uniformly decorated nanospheres (see, Fig. 3.3a). The structure is composed of spatially distributed nanoparticles embedded in a carbon matrix, i.e., dark dots in the TEM micrographs seen in Fig. 3.3b. HRTEM analysis further reveals the structural details of the final NC, namely formation of a nanoparticle with lattice fringes of 2.22 Å, ascribed to the (111) lattice space of Pt_3Co[99], which is partially encapsulated by a highly-graphitized carbon shell as indicated by the 3.38 Å characteristic graphitic interlaminar spacing (Fig. 3.3c)[100-102]. High angle annular dark-field (HAADF) contrast image of a typical matrix-dispersed nanoparticle in the 125-Pt_3Co@C-Co_3O_4 NC is shown in Fig. 3.3d. To further scrutinize the structural details in these systems, electron energy loss spectroscopy (EELS) was performed in the area denoted by the dotted yellow lines in Fig. 3.3d; the corresponding spectra is depicted in Fig. 3.3e. The presence of characteristic carbon K-edge peaks are evident in Fig. 3.3e. More specifically, at $\simeq$ 290 eV, corresponding to the 1s states transitions to σ^* orbitals, and at $\simeq$ 285 eV, on the account of transitions from 1s to π^* orbital, which in turn reveal the presence of sp^2 bonding in the carbonaceous phase of the analyzed area. Similarly, the peak observed at $\simeq$ 323 eV in Fig. 3.3e can be ascribed to the delayed Pt $N_{4,5}$ edge[103], while the peaks at $\simeq$ 782 ev and $\simeq$ 798 ev correspond, respectively, to the delayed Co L_2 and L_3 edges[104]. In order to gain a better understanding of the spatial-dependence of the elemental composition of this NCs, highly resolved spatial information provided by the EELS intensity maps, were acquired from the spectrum-image of the area indicated by the dotted lines in Fig. 3.3d (see Fig. 3.3e).

The elemental mapping presented in Fig. 3.3f indicates a heterogeneous elemental distribution in the nanoparticle bimetallic phase; the color scheme in the metallic region reveals a structure characterized by a Pt-rich outer layers and a bimetallic core. Fig. 3.3f also shows the local concentration of elemental carbon that is encapsulating the bimetallic Pt-Co nanoparticle core, further corroborating with the above-mentioned presumption of existing carbon-based architectures. i.e., graphitic-coating and carbon-formed matrices that surround the metal-rich centers in the NCs.
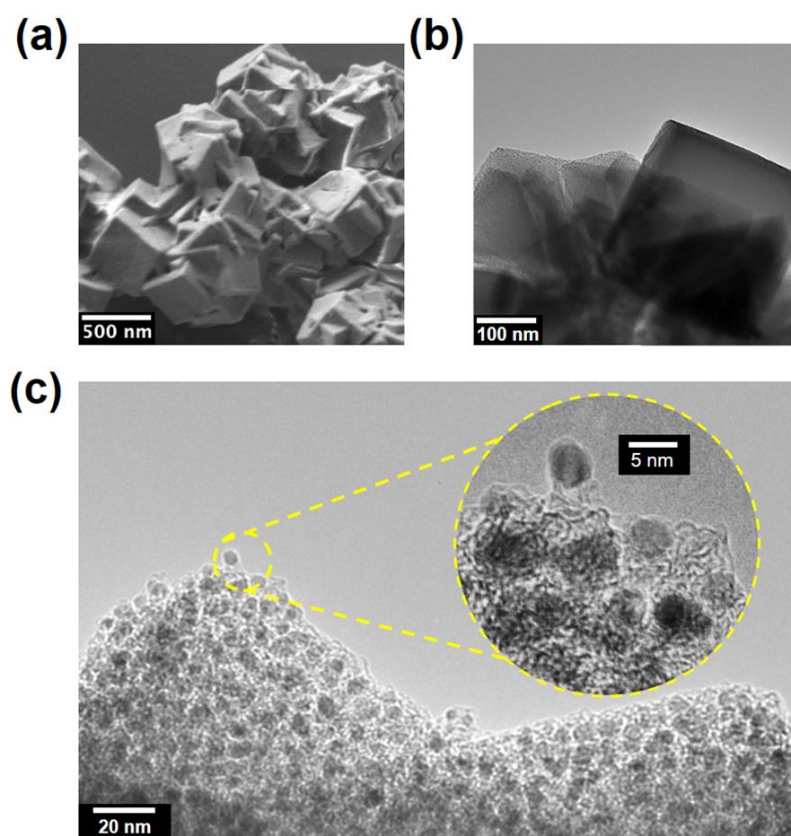
Figure 3.2. Representative (a) SEM (b) TEM and (c) HRTEM micrographs of 125-Pt$_3$Co@ZIF-67.
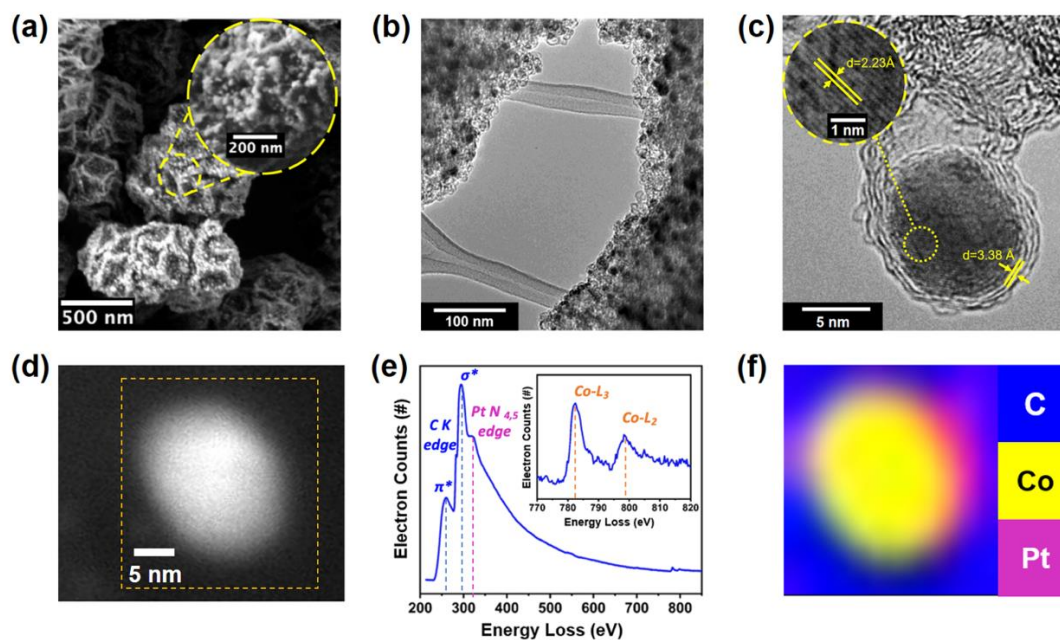
Figure 3.3. (a) SEM micrograph of a typical 125-Pt$_3$Co@Co$_3$O$_4$ composite (b) TEM micrograph of a characteristic section of the 125-Pt$_3$Co@Co$_3$O$_4$ composite (c) HRTEM micrograph of a graphene-encapsulated Pt-Co bimetallic nanoparticle in the 125-Pt$_3$Co@Co$_3$O$_4$ composite with characteristic Pt$_3$Co (111) (inset) and graphene (111) lattice spacing (d) HAADF-TEM image of a typical 125-Pt$_3$Co@Co$_3$O$_4$ matrix-dispersed nanoparticle, inset marked by dotted yellow lines indicates the area analyzed in the (e) EELS spectra and (f) EELS-generated elemental mapping

To further investigate the composition and crystallinity of these prototypical structures, x-ray diffraction (XRD) patterns were obtained for the 125-Pt$_3$Co@ZIF67 and 125-Pt$_3$Co@C-Co$_3$O$_4$ NCs, as shown in Fig. 3.4a. In the diffraction patterns obtained for sample 125-Pt$_3$Co@ZIF67, the existence of a highly-crystalline ZIF-67 phase is confirmed by the presence of peaks ascribed to the diffraction patterns characteristic of this framework[104-105]. However, these same ZIF-67 characteristic patterns can no longer be observed in the XRD data obtained for the 125-Pt$_3$Co@C-Co$_3$O$_4$ NC, indicating that the pyrolysis post-treatment led to complete thermal decomposition of the imidazole based-frameworks. In addition to that, the XRD patterns for the 125-Pt$_3$Co@C-Co$_3$O$_4$ NC reveal the large presence of highly crystalline cobalt oxide phases (Co$_3$O$_4$)[106] in of ultra-small crystallite clusters ($\simeq$ 3 nm), as estimated from the full width half maximum (FWHM) of the observed-diffraction peaks for Co$_3$O$_4$ based on Scherrer's equation.

The absence of distinguishable Co$_3$O$_4$ nanocrystals in our Pt$_3$Co@C-Co$_3$O$_4$ NCs TEM analyses can be rationalized in terms of the technical limitations in identifying such small structures when encompassed by a dense 3-dimensional (3D) carbonaceous matrix. The acquisition of high-resolution and well-defined TEM images requires the incoming electron beam to be precisely focused on the image plane containing the desired analysed area, which in turn becomes more difficult as the sample thickness increases and consequently amplifies electron scattering phenomena. As a result, the high magnification required for the TEM imaging of such small phases demands very delicate electron beam focusing conditions that become virtually inconceivable due to the extreme difficulty in identifying the precise orientation of the image plane to capture the exact positioning of these ultra-small crystals.

In light of these considerations, it is reasonable to infer that these poor imaging conditions could have generated artefacts, such as distortions and weak contrast variations, consequently concealing the Co$_3$O$_4$ presence in the 125-Pt$_3$Co@C-Co$_3$O$_4$ NCs. On the other hand, in terms of the x-ray diffraction analyses, both the diffraction patterns for samples 125-Pt$_3$Co@ZIF67 and 125-Pt$_3$Co@C-Co$_3$O$_4$, as shown in Fig. 3.4a, clearly exhibit a subtle peak at around $2\theta = 40.3$ °. The presence of the aforementioned peak can in fact be ascribed to the diffraction arising from the Pt-Co (111) plane[33].
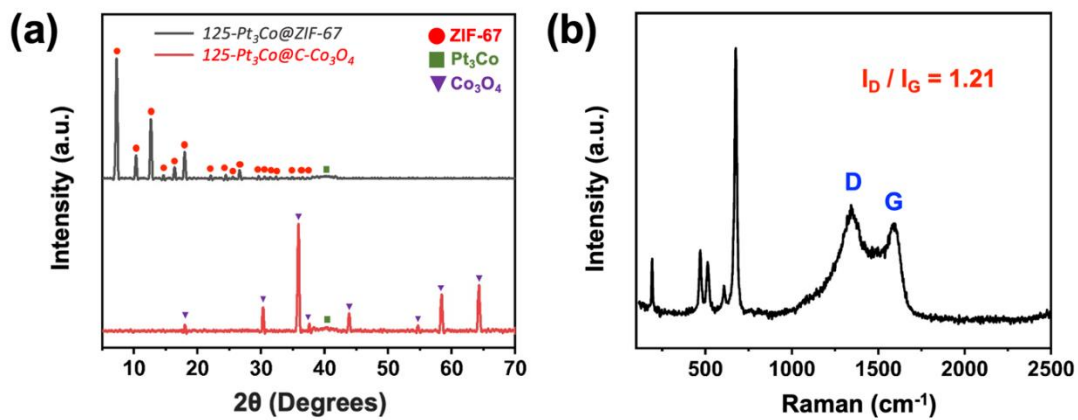
Figure 3.4. (a) XRD diffraction patterns of (i) 125-Pt$_3$Co@ZIF-67 and (ii) 125- Pt$_3$Co@C-Co$_3$O$_4$; (b) Raman Spectra of 125-Pt$_3$Co@C-Co$_3$O$_4$

Apart from their agreement with our previous TEM observations indicating the presence of Pt-Co phases in the 125-$Pt_3Co@C-Co_3O_4$ nanoparticles, these results further confirm the early nucleation of these phases in the 125-$Pt_3Co@ZIF67$, demonstrating that the alloying phenomena ensues during the laser ablation step itself, and does not originate from the post-processing treatments, as discussed in detail in the later sections.

In fact, crucial crystallographic information of the observed Pt-rich phases can be acquired from the aforementioned Pt-Co (111) diffraction pattern, consequently providing a better understanding regarding the structure-property relations of such phases in the LASiS-derived NCs. To that end, in order to overcome the low signal-to-noise ratios arising from the reduced concentrations of the Pt-Co phases, low-scan-rate XRD analyses of the 63, 95 and 125-$Pt_3Co@C-Co_3O_4$ samples are carried out with the 2θ values ranging from 38.5° to 41.5 ° (shown in Fig. 3.5a). These slow-scan diffraction data are used here along with the Vegard's law to estimate the alloyed Pt:Co ratios as 9.1:1, 9.5:1, and 7.4:1 for the 63, 95, and 125-$Pt_3Co@C-Co_3O_4$ samples respectively. These observations corroborate the Pt weight percentages estimated in the final products obtained from ICP-OES measurements. As expected, higher initial K_2PtCl_4 concentrations yielded greater Pt loadings in the $Pt_3Co@C-Co_3O_4$ NCs (Fig. 3.5b)

Finally, for a comprehensive understanding of the structural nature of the as-manufactured LASiS-based NCs, Raman spectra of the 125- $Pt_3Co@C-Co_3O_4$ sample in Fig. 3.4b clearly depict four distinct peaks at 677, 517, 470 and 193 cm^{-1} that can be ascribed to the A_{1g} and F_{2g} modes of the Co_3O_4 phase[41]. Furthermore, the two broad peaks at 1351 and 1604 cm^{-1} are assigned, respectively, to the D and G characteristic carbon peaks[108], resulting from the massive presence of C in the aforementioned NCs. More specifically, the D peak arises from the *k*-point mode phonons of A_{1g} symmetry while the G peak is related to the E_{2g} phonon of C_{sp2} vibrations, further confirming the presence of carbon in both amorphous and graphitic phases. Quantitative estimations of the presence of such carbon phases can be obtained based on the D/G peaks intensity ratios (I_D/I_G) [108], as indicated in Fig. 3.4b, where a higher (I_D/I_G) ratio suggests higher existence of disorder/defects arising from the presence of amorphous phases, relative to graphitic phases. A summary of the results obtained for the ICP-OES and XRD analyses is shown in Fig. 3.5.

39

(a)

(b)
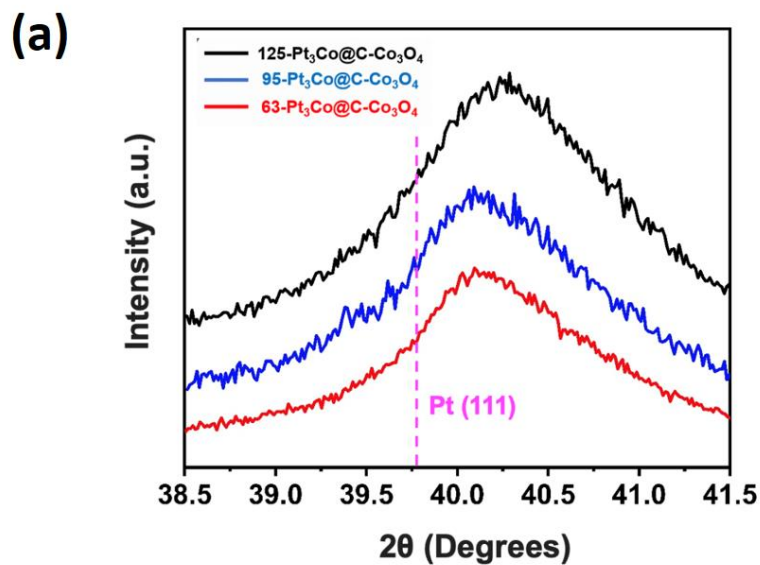
Sample	2θ Pt-Co (111)	Pt:Co (Vegard's Law)	Pt (%Weight) ICP-OES
125-Pt₃Co@ZIF-67	40.27 °	7.388	5.20
93-Pt₃Co@ZIF-67	40.14 °	9.499	4.42
65-Pt₃Co@ZIF-67	40.13 °	9.713	4.16

Figure 3.5. (a) Slow-scan XRD of 125, 93 and 65-Pt$_3$Co@C-Co$_3$O$_4$ NCs in the Pt-Co (111) diffraction region (b) Summary of (i) characteristic 2θ Pt-Co (111) diffraction peak; (ii) estimated Pt:Co alloying ratio from Vegard's law; and (iii) weight percentage of Pt for samples 125, 93 and 65-Pt$_3$Co@C-Co$_3$O$_4$

Laser-driven formation mechanistic insights

As previously described in the methodology section, the LASiS system herein comprises an Nd-YAG laser source directed towards a solid cobalt target, which in turn is immersed into a liquid solution (containing KOH, Hmim and K_2PtCl_4). The process is initiated when the first pulse of the high energy laser beam interacts with the Co target to start the complete thermal vaporization and dissociation of the Co atoms/ions that, in turn, creates a liquid confined plasma plume with extremely high temperatures and pressures ($\sim 10^3$ K and 10^6 Pa)[76]. Supersaturation of the metal monomers arising from the extreme conditions in the plasma plume leads to the nucleation of seeding Co nanoparticles within an oscillating cavitation bubble, generated from the expanding plasma plume that expands and propagates an ultrasonic shock wave[31]. While the exact non-equilibrium pathways governing these systems are still a subject of debate, recent studies have facilitated some preliminary understanding regarding the critical steps during the laser ablation process under liquid environments. More specifically, spatio-temporal analyses of laser-induced plasma emissions have pointed out the early presence of solution species in the interior of the cavitation bubble[109-113]. The coexistence of solution and ablated phases inside the cavitation bubble enable these species to participate in reaction pathways that can be promoted by the extreme localized temperatures and pressures. Taking into account the redox potential of Co/Co^{2+} (-0.28 V *vs.* SHE) and $PtCl_4^{2-}$/Pt (0.76 V *vs.* SHE), the nucleated Co nanoparticles are expected to undergo Galvanic Replacement Reaction (GRR) generating ionic cobalt and metallic Pt, as shown in equation 1 below:

$$Pt^{2+} + Co \rightarrow Pt + Co^{2+} \qquad\qquad (1)$$
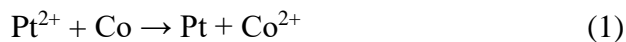
Nonetheless, due to the high local density of Co nanoparticles and the rate-limiting kinetics of the GRR process, only a portion of the nucleated Co nanoparticles is likely to take part in the reaction pathway depicted in Eq 1. The coexistence of Co and Pt metallic nanoparticles in such extreme conditions leads to the formation of secondary nanostructures through the alloying phenomena, giving rise to the appearance of the Pt-Co bimetallic nanoparticles, as extensively evidenced in our characterizations. The details for

41

the alloying process during LASiS-GRR have also been described in detail in our earlier works [31-35]. Upon the collapse of the cavitation bubble, the remaining unreacted Co nanoparticles undergo oxidation by the solution species driven by their respective relative redox potentials: (O_2/OH^- 0.40 V *vs.* SHE) / (Co/Co^{2+} −0.28 V *vs.* SHE)[27]. Thereafter, the existing Co ions in the solution, either from GRR or from oxidation by the solution species, become the ionic precursors for the reaction pathways leading to the formation of ZIF-67 structures (the details for this process are also described in details in our previous work[114]). Specifically, the just-formed Co^{2+} ions are immediately coordinated by Hmim molecules, which, in turn, are rapidly deprotonated leading to the oligomerization event, typically characterized by the connection of two Co^{2+} centers *via* a deprotonated Hmim molecule. The presence of Pt-Co bimetallic nanoparticles originated from the earlier laser ablation stages is expected to decrease the free energy barrier for the heterogeneous nucleation of ZIF-67[49] on the surfaces of the aforementioned nanoparticles. In order to test this hypothesis, we have analyzed the size distribution of the MOFs synthesized in both the presence and absence of K_2PtCl_4, maintaining all the other conditions (ablation time, KOH and Hmim concentration) unchanged. The size distributions depicted in the insets of the SEM micrographs shown in Fig. S3 indicated that the overall MOF sizes significantly decrease when K_2PtCl_4 is introduced to the system, indicating that the presence of Pt-Co nanoparticles originated from the GRR in tandem with the alloying events play a major role in the early onset of the nucleation rates of the ZIF-67. Distinct morphological changes in the ZIF-67 structures can be additionally observed in Fig. 3.6. It was observed that MOFs synthesized in the absence of K_2PtCl_4 presented large truncated rhombic dodecahedron morphologies, while the introduction of K_2PtCl_4 in the initial reaction system resulted in cubic-shaped ZIF-67 structures. In fact, these observed reductions in the framework sizes, along with the clear morphological changes, support our hypothesis of an enhanced nucleation and growth rate of the MOF species in the presence of the seeding Pt-Co nanoparticles, as discussed previously[114]. The incorporation of the aforementioned nanoparticles by the growing MOF phase also significantly hinders the aggregation and coalescence of the nanoparticles in the system owing to their stabilization inside the MOF matrix. Finally, the post-pyrolysis treatments of the LASiS-synthesized materials induce

42

the thermal decomposition of the original ZIF-67 structures, producing an interconnecting carbon-based matrix decorated with ultra-small Co_3O_4 crystals and spatially dispersed bimetallic Pt-Co nanoparticles. Local observations of graphitic shell formation around the Pt-Co nanoparticles are attributed to the interfacial catalytic graphitization of carbon on the metal surfaces during the high-temperature pyrolyzation[117].

Functional characterizations

The oxygen reduction reaction (ORR) electrocatalytic activities for the $Pt_3Co@C$-Co_3O_4 NCs are finally investigated with rotating disk electrode (RDE) measurements using 1 M KOH as the electrolyte solution. Unlike the vast majority of reports on ORR electrocatalysts in alkaline media that are typically based on RDE operating in 0.1 M solutions of alkali hydroxides, herein, the selection of an electrolyte containing significantly higher hydroxyl concentrations (1 M KOH) was intentional in order to carry out stringent tests on the stability of the LASiS-based NCs under harsh and extreme alkaline conditions of the ORR electrocatalysis operations. Apart from demanding greater electrocatalyst robustness to endure the extreme corrosive environments of the electrolyte, ORR electrocatalysis operations under higher alkaline concentrations are typically more challenging owing to the reduced oxygen solubility and diffusivity in the electrolyte, as well as increased coverage of the electrocatalyst surfaces by the OH_{ad} species[118-119]. To this end, the electrochemical evaluation of the LASiS-based electrocatalysts in a higher alkaline concentration provides a more rigorous assessment of the suitable ORR electrocatalytic performance of our as-manufactured NCs. Fig. 3.7a shows the ORR polarization curves for all the NCs and the commercial Pt/C ORR catalyst (C-Pt). The results depicted in Fig. 3.7a clearly show the superior ORR performance of the LASiS-synthesized NCs when compared to standard Pt/C catalytic systems. Such remarkable performance is even observed for the Pt-free NCs (C-Co_3O_4), displaying a significant 40 mV positive shift in terms of half-wave potential ($E_{1/2}$) as compared to the C-Pt systems. These results indicate that the C/Co_3O_4 matrix, derived from the pyrolysis of the ZIF-67 structures, might also play a significant role in the ORR performance of the $Pt_3Co@C$-Co_3O_4 NCs. These results confirm the importance of the supporting matrix in these composites.
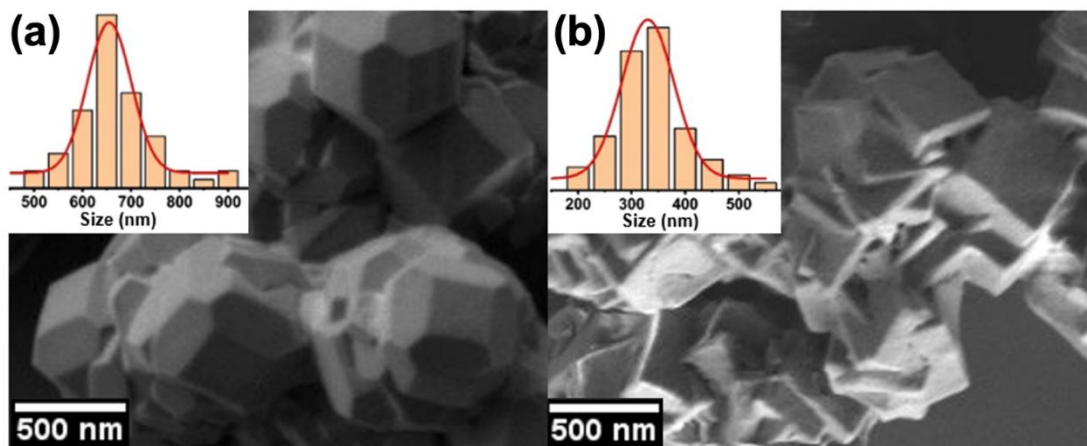
Figure 3.6. SEM micrographs of ZIF-67 synthesized in (a) absence of K_2PtCl_4; and (b) presence of 125 mg/L K_2PtCl_4
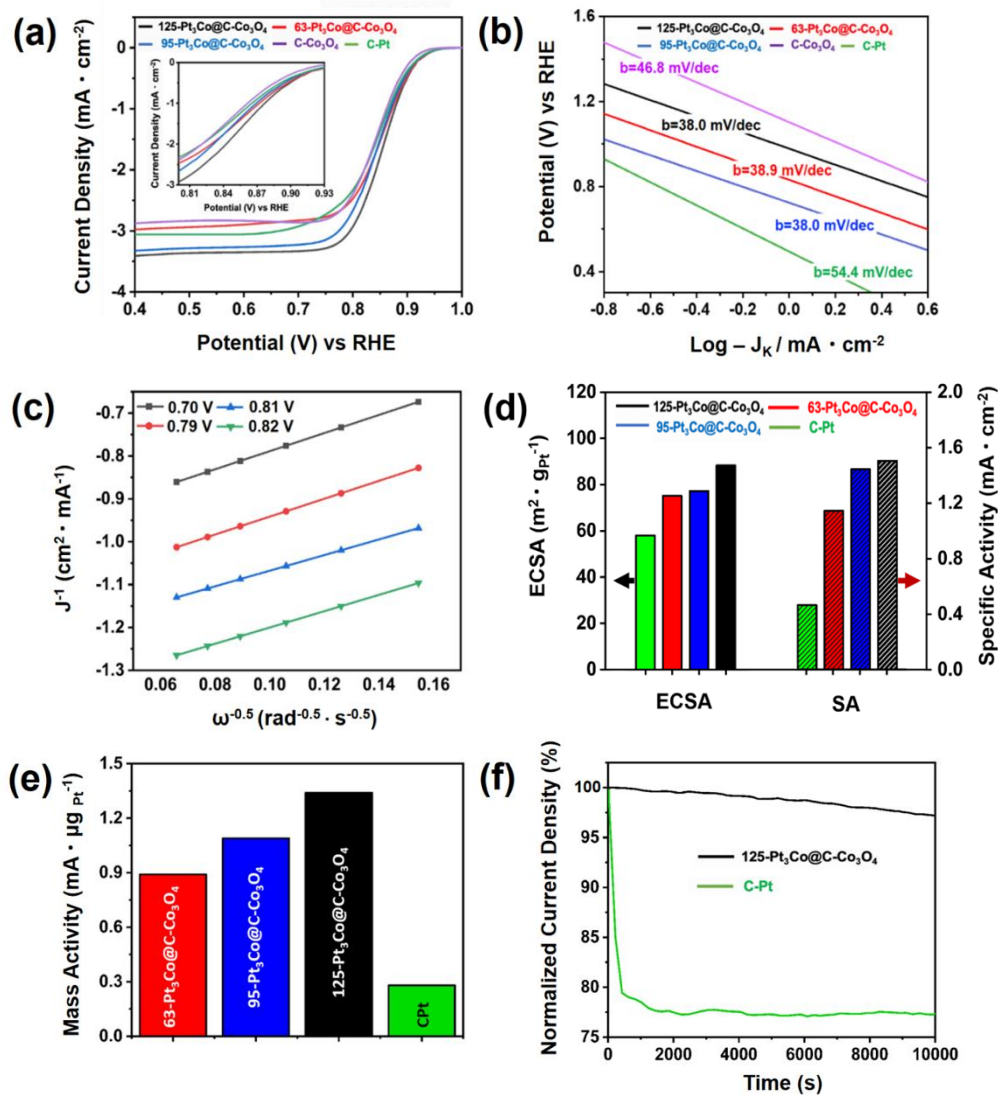
Figure 3.7. Electrochemical data for LASiS-based nanocomposites ORR electrocatalytic activities (a) Linear sweep voltammograms (LSV) for ORR polarization curves in 1M KOH saturated with dissolved O_2 at 1600 rpm and scan rate of 5 mV/s; (b) Corresponding Tafel plots; (c) Koutecky-Levich plots from rotating disk voltammogram (RDV) of 125-$Pt_3Co@C$-Co_3O_4 at different potentials (0.70-0.82 V) indicating four electron transport process for ORR; comparison of (d) ECSA and specific activity; and (e) mass activity at 0.85 V ; (f) Stability comparison at 0.85V of 125-$Pt_3Co@C$-Co_3O_4 and C-Pt at 0.85 V *via* chronoamperometry test.

As such, the matrix itself exhibits excellent catalytic activity that can symbiotically enhance the ORR performance of the $Pt_3Co@C$-Co_3O_4 NCs through a co-operative catalysis with the Pt-Co nanoparticles, similar to the spill-over effects described in our earlier works[32-33]. In fact, the catalytic activities of carbon-based materials in alkaline electrolytes for the 2-electron reduction of oxygen to peroxide intermediates have also been suggested in previous studies[119-120]. Added to this, the introduction of a 3d transition metal to the carbon matrix here is likely to result in a synergistic configuration between these metal centers and the carbonaceous support, owing to the strong interaction between these two phases. Specifically, in the C-Co_3O_4 matrix radical oxygen intermediates resulting from the O_2 activation on the carbon surfaces are able to spill over to the Co_3O_4 phases, where they can be further reduced completing the typical 4-electron ORR pathway[121-122]. Moreover, the structural 3D nanoarchitecture provided by the C-Co_3O_4 support creates a network that can promote isotropic ion diffusion and charge transfer, both highly desirable characteristics for an efficient ORR electrode[123].

Furthermore, the results depicted in Fig. 3.7a demonstrate the ability of the Pt-Co nanoparticles to further enhance ORR performance of the NCs despite their relatively low concentrations. Fig. 3.7a clearly indicates that, among all the samples, 125-$Pt_3Co@C$-Co_3O_4 NCs demonstrate the highest ORR activity, both in terms of the onset potential (E_{onset} = 0.95 V) and the diffusion-limited current. This outstanding ORR performance is also evident from our half-wave potential analyses, indicating that the 125-$Pt_3Co@C$-Co_3O_4 NCs present an outstanding 60 mV positive half-wave shift as compared to the state-of-art commercial Pt catalysts (C-Pt). In addition, CV analyses of the $Pt_3Co@C$-Co_3O_4 NCs (Fig. 3.8) reveal the presence of similar electrochemical features to the ones commonly observed in pristine Pt electrocatalysts. Specifically, the NCs voltammograms exhibited peak currents in the H_{upd} and OH adsorption regions (0.05 – 0.4 V and 0.6 – 0.85 V *vs* RHE), respectively, suggesting a significant presence of Pt-rich exposed surfaces in all the $Pt_3Co@C$-Co_3O_4 samples. Such exposed surfaces are associated to the existence of defects in the encapsulating graphitic shells of the bimetallic Pt-Co nanoparticles in these NCs. Relative to the C-Pt electrocatalyst, however, anodic shifts can be clearly observed in the Pt-OH_{ad} peaks of all the $Pt_3Co@C$-Co_3O_4 NCs.

These specific shifts indicate a reduction in the desorption free energy of OH species that are adsorbed onto the Pt-rich surfaces, which in turn is ascribed to the effects of the Pt-Co alloying configuration in the metallic phase of the electrocatalytic nanoparticles dispersed throughout the NCs. Additionally, the synthesized NCs displayed minor peak currents approximately at 0.7 V (anodic scan) and 0.5 V (cathodic scan), both absent in the C-Pt voltammogram.The appearance of this peak pair is associated to the formation of platinum-cobalt-(hydro)-oxide (Pt-CoO$_x$H$_y$)[124], further confirming the presence bimetallic Pt-rich phases in these NCs. The Pt-phase electrochemical active surface area (ECSA) values obtained from the integration of the charges in the H$_{upd}$ region from each CV curve are displayed in Fig. 3.7d. The outstanding ECSA for all the Pt$_3$Co@C-Co$_3$O$_4$ NCS reveal the ability of their unique nanoarchitectures to efficiently enhance the available Pt surface area-to-mass ratio. In a similar manner, the mass-activities measured at 0.85 V potential for the 125-Pt$_3$Co@C-Co$_3$O$_4$ NCs demonstrate a nearly 5-fold enhancement as compared to the C-Pt catalysts. This is closely followed by the 4-fold and 3-fold enhancements recorded for the 93-Pt$_3$Co@C-Co$_3$O$_4$ and 65-Pt$_3$Co@C-Co$_3$O$_4$ NCs, as displayed in Fig. 4e. The Tafel plots (Fig. 4b) for the kinetic-diffusion region of the ORR polarization curve display lower values for the slopes for all the Pt$_3$Co@C-Co$_3$O$_4$ NCs when compared to the standard Pt/C commercial catalyst. This is particularly evident for the 125- Pt$_3$Co@C-Co$_3$O$_4$ NCs, displaying a slope of 38.0 mV/dec as compared to the 54.4 mV/dec for the C-Pt case. These results indicate an enhanced ORR charge transfer kinetics for all the LASiS-based NCs, specifically ascribed to the highly conductive nature of the matrix support arising from an abundance of interconnected sp^2 hybridized carbonaceous clusters. In addition to these data, the well-known Koutecky–Levich plots for the 125- Pt$_3$Co@C-Co$_3$O$_4$ NCs (Fig. 4c) exhibit a linear behavior with constant slopes over the potential range analyzed (0.70 - 0.82V). Based on these slopes, the quantification of the number of electrons transferred during the ORR catalysis yielded a near 4-electron transport process in the mixed kinetic-diffusion region, demonstrating the activation of the more energetically favored 4-electron reaction pathway. Such findings suggest that the encapsulation of the Pt-Co nanoparticles by graphitic layers, as previously shown in Fig. 3.3c, does not impose a significant barrier for the charge transfer that takes place between the electrocatalytic active sites and solution

47

species during ORR. In fact, previous studies based on density functional theory (DFT) have shown that when graphene-like structures are adjoined to certain metals substrates (e.g. Al, Ag, Cu, and Pt), the interaction among these phases is sufficiently low to induce any change in the graphitic electronic structure, thereby preserving their outstanding electronic properties[125]. In addition to that, this configuration can, in fact, shift the Fermi level of carbon materials with respect to the conical point by approximately 0.5 eV, resulting in an alternation of its work function[126-127]. While a complete understanding on the influence of such complex configurations in the ORR electrocatalytic activity of these structures is still elusive, beyond the scope of the present study, lowering the work function can only benefit the ORR electrocatalytic activity of the aforementioned materials. A reduced work function diminishes the energetic barrier for the charge transfer between the carbon structure and the surface-absorbed O_2 species, consequently facilitating the formation of OOH (typically considered as the rate-determining step during ORR). As an attempt to better elucidate the structure-property relations in all our $Pt_3Co@C-Co_3O_4$ NCs manufactured here, we take into consideration the Pt:Co alloyed ratios estimated from our earlier diffraction analyses based on Vegard's law. Our investigations indicate that the NCs with the highest lattice shrinkages (i.e., the 125-$Pt_3Co@C-Co_3O_4$ NCs) exhibit the best ORR activity. It should be noted here that such observations might further evidence the presence of exposed Pt_3Co surfaces, as indicated earlier by the CV measurements, suggesting that a balanced Pt:Co ratio with a higher degree of Pt-Co alloying in the nanoparticles can enhance the overall ORR performance of the NCs. These correlations can be rationalized in terms of the well-studied Pt-Co alloying phenomena that have been traditionally associated with the enhancements in the ORR electrocatalytic activities of Pt-rich bimetallic nanoparticles[128]. Shifts in the interfacial electronic energy levels arising from the Pt-Co alloying can result in changes in the adsorption properties, some of which are expected to positively affect the ORR activity of the LASiS-based NCs. As compared to bare-Pt catalysts, for instance, the results obtained from the CV analyses indicated a reduction in chemisorption energy of OH solution species adsorbed onto the Pt-rich surfaces of all the $Pt_3Co@C-Co_3O_4$ NCs. In fact, alterations in energy levels arising from the Pt-Co alloying configuration are well-known to suppress the adsorption of OH species

(OH_{ads}) on Pt-rich surfaces, consequently preserving a higher number of available active sites and greatly enhancing the rate of electrocatalysis [129-131]. In addition to that, the affinity of the Pt-Co alloyed surfaces for O_2 species is enhanced owing to changes in its 5d orbital vacancies that facilitates the transport of π electrons from O_2 to Pt[132-133]. In this regard, a higher degree of Pt-Co alloying in the NPs would simultaneously promote the adsorption of O_2 and desorption of OH_{ads} species on the Pt-rich surfaces, thereby greatly accelerating their ORR kinetics. These unique configurations, along with the synergistic spill-over effects offered by the carbonaceous and cobalt-oxide phases in the C-Co_3O_4 matrix, give rise to a unique set of co-operative electrocatalytic processes, which in-tandem with an efficient interfacial transport culminate in the extraordinary ORR activities observed for all the LASiS-based $Pt_3Co@C-Co_3O_4$ NCs. In terms of practical applications, the long-term stability of Pt-based electrocatalysts for ORR still remains a major challenge, particularly in highly concentrated alkaline media. Degradation of the catalyst arising from the harsh environment imposed by the electrolyte combined with the commonly observed nanoparticle sintering phenomena, such as Ostwald ripening, often result in a loss of electrochemical surface area leading to a substantial decline in the observed ORR performance. To test the electrocatalytic stability of these LASiS-driven NCs, chronoamperometry measurements at 0.85 V in an O_2-saturated 1 M KOH aqueous solution reveal excellent long-term durability of the 125-$Pt_3Co@C-Co_3O_4$ NC structures as seen from Fig. 3.7f. The electrodes prepared with the 125-$Pt_3Co@C-Co_3O_4$ NCs displays a minor current density reduction of less than 3% in terms of its initial value after 10000 cycles under continuous operation. On the other hand, under the same conditions, the commercial Pt catalysts suffered a dramatic deterioration of $\simeq$ 21% in its initial current density within the first 200 cycles, reaching an overall $\simeq$ 23% loss during the 10000 cycles operation. The superior long-term stability observed in the 125-$Pt_3Co@C-Co_3O_4$ NCs can be ascribed to the role played by the C/Co_3O_4 matrix as a mechanical support and scaffold for the catalytic nanoparticles. Thus, the integration of these nanoparticles into the matrix provides them an enhanced physical stabilization, which in turn, limits their mobility and consequently hinders common catalytic degradation routes such as surface contaminations

49

and loss of electrochemical surface area from aggregation/coalescence and/or, particle detachment phenomena.

Conclusions

We have applied here the tandem LASiS–GRR technique along with post-processing pyrolysis treatments for the fabrication of low-Pt loading NCs comprising Pt-Co bimetallic nanoparticles encapsulated in a Co_3O_4-infused carbonaceous matrix. Specifically, the fabrication technique employed the systematic pyrolysis of the ZIF-67 MOF scaffolds encapsulating the Pt-Co alloyed nanoparticles, both of which were simultaneously synthesized out of a series of well-orchestrated laser-driven reaction pathways enabling the coordination-complexation events. Detailed structural, morphological and elemental analyses reveal the formation of a carbonaceous matrix decorated with ultra-small Co_3O_4 crystallites and dispersed Pt-Co alloyed nanoparticles, which are in turn, partially coated by a highly graphitized carbon shell. The as-manufactured NCs exhibit superior ORR electrocatalytic activities in harsh alkaline media. LASiS-based NCs obtained *via* three distinct Pt-precursor initial concentrations are evaluated as ORR electrocatalysts. Specifically, the NCs synthesized in 125 mg·L^{-1} K_2PtCl_4 solutions indicate a remarkable 5-fold increase in their mass activities as compared to the state-of-art commercial Pt catalysts. These outstanding performances are attributed here to the electrocatalytic enhancements arising from the Pt-Co nano-alloyed configurations along with co-catalytic co-operations resulting from the unique synergistic spill-over effects facilitated by the Co_3O_4 crystallites present in the carbon matrix support. In summary, we have reported here the simple yet elegant application of a well-synchronized LASiS-GRR technique for the facile synthesis of Pt-Co bimetallic NCs in C/Co_3O_4 support matrices that go on to exhibit remarkable and robust ORR electrocatalytic activities under extreme alkaline conditions. The findings presented here open up a myriad of possibilities for the use of LASiS-GRR along with suitable precursors in the rational design of unique MOF-derived functional nanoarchitectures.
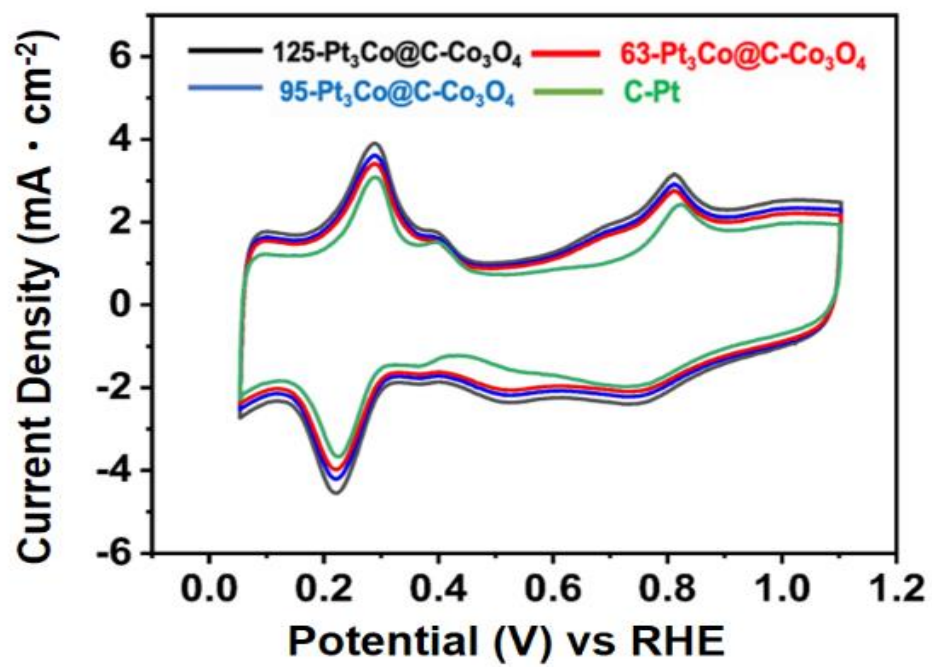
Figure 3.8. Cyclic voltammetry curves performed at a scan rate of 100 mV/s in a N_2-saturared 1M KOH solution.

CHAPTER FOUR

HYBRID NANOCOMPOSITES OF NANOSTRUCTURED COBALT OXIDE INTERFACED WITH REDUCED/NITROGEN-DOPED GRAPHENE OXIDE FOR SELECTIVE IMPROVEMENTS IN ELECTROCATALYTIC AND/OR SUPERCAPACITIVE PROPERTIES

This chapter is based on the submitted article: *"Hybrid nanocomposites of nanostructured Co_3O_4 interfaced with reduced/nitrogen-doped graphene oxides for selective improvements in electrocatalytic and/or supercapacitive properties"* by Erick L. Ribeiro, Sheng Hu, Seyyed Ali Davari, Mengkun Tian, Dibyendu Mukherjee, and Bamin Khomami.

Introduction

Graphene and reduced graphene oxide (rGO) have been well-characterized as the classical two-dimensional (2-D) materials with unique honey-comb lattice structures that exhbit unique physicochemical properties along with high electrochemistry surface area and thermal/electrical conductivity[134]. Addtionally, efforts have been directed towards chemically reacting GO with nitrogen-containing species to synthesize nitrogen-doped GO (NGO) that are known to exhibit higher electron mobility and chemical compatibilies as compared to other metal/metal oxides dopants[140-142,155-160]. In turn, both rGO and NGO have been widely explored and reported as potentially excellent supporting mateirals for various catalytic systems as well as EDLC materials[137, 161-165]. A highly promising earth-abundant transition metal oxide, cobalt oxide (Co_3O_4)-based nanomaterials have gained prominence in recent years due to their relatively good ORR activities in alkaline conditions along with outstanding pseudo-capacitance capabilities[139,159,160,162,166]. To this

end, much recent research has been devoted in assembly of Co_3O_4 nanoparticles (NPs), nanorods (NRs), and nanosheets into rGO/NGO to form hybrid nanocomposites (HNCs)[159-160]. The inherent strong coupling and consequent synergistic effects between the metal oxide nanostructures and rGO/NGO result in larger effective electrochemical surface areas and higher electron conductivity for the faradaic reactions to take place[167-171]. This in turn promotes a higher and more stable ORR catalytic activity as well as an enhanced capacitive capability that facilitates their behaviors as both EDLC and pseudocapacitors[159]. However, simple physical mixing of metal oxides and rGO/NGO would inevitably impede the charge transfer processes across the composite material for both ORR and capacitive performances due to the high electron resistivity at the interface[172-173]. To address the abovementioned issue, researchers have typically resorted to chemical synthesis routes to assemble various heteronanostructures chemisorbed and/or embedded into 2-D matrices such as graphene, GO, MoS_2 etc[171-174]. While such routes have been successfully used in the past to synthesize HNCs, they almost always involve complex multiple steps[175-176], and sometimes unwanted/harsh chemical and surfactants[177] that can be left behind as residues, thereby degrading the active interfacial areas for catalytic and charge transport pathways. This chapter addresses the use of LASiS in conjunction with two different post-treatments to incorporate three types of cobalt oxide nanostructures into rGO/NGO sheets for synthesizing tailored HNCs, as illustrated in Fig. 4.1.

Experimental procedure

Laser-based synthesis of Co_3O_4/rGO-NGO Hybrid Nanocomposites
All chemicals were purchased from Sigma-Aldrich. GO suspension was prepared by following the commonly practiced improved Hummers method[189]. Co pellets were bought from Kurt J. Lesker (99.95% purity, 1/4" diameter×1/4" height). LASiS experiments were carried in the experimental system previously described. Specifically, the freshly prepared GO solution with the concentration of 20 mg/L was bath-sonicated for 30 min before transferring into the LASiS reactor cell. The target metal was ablated using the unfocused 1064 nm pulsed Nd-YAG for 3 min. The products were collected by centrifuging at 4700
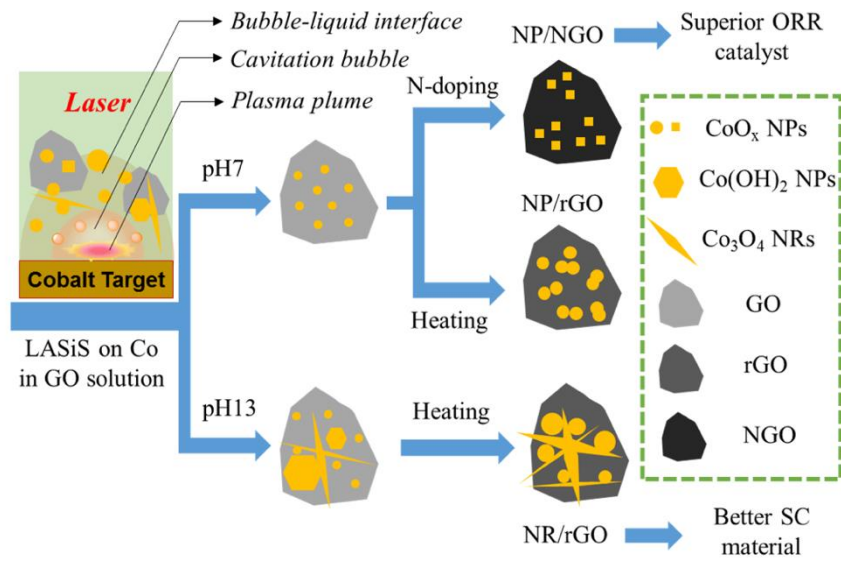
Figure 4.1. Graphical abstract of the synthesis of Co_3O_4/rGO and Co_3O_4/NGO HNCs *via* LASiS.

rpm for 15 min and decanted after washing with DI-water for two times. For LASiS in alkaline conditions, KOH (99.5%) was used to tune the solution pH to the desired alkaline condition (pH13).

Post-treatments: For the synthesis of all Co_3O_4/rGO HNCs, the products from centrifugation were heated at 250°C under vacuum for 3 hours. For production of all Co_3O_4/NGO HNCs, the products from centrifugation were re-suspended in 25 mL of deionized (DI) water, urea was then added at the ratio 300:1 (Urea: GO). The mixture was sealed in a 50 mL Teflon-lined autoclave and held at 180°C for 3 hours. The products were filtered and washed several times with DI-water. Finally, the dark powder obtained from the filtration was dried at 80°C for 3 hours.

Characterizations

For the detailed morphological characterization of the final products, a Zeiss Libra 200MC monochromated transmission electron microscope (TEM) was used with an accelerating voltage of 200 kV for regular TEM characterizations along with selected area electron diffraction (SAED) and energy dispersive X-ray spectroscopy (EDX). The scanning electron microscopy (SEM) images were acquired using a Philips XL-30ESEM equipped with an energy dispersive X-ray spectroscopy. A Zetasizer (Make: Malvern; Model: nano ZS) was used for measuring zeta potentials of the colloidal solutions. The Cobalt metal concentrations in the composites under study were measured via inductively coupled plasma optical emission spectroscopy (ICP-OES) (Make: Perkin Elmer; Model: Optima 4300 DV) and the in-house developed quantitative laser-induced breakdown spectroscopy (Q-LIBS) as described elsewhere[190-191]. X-ray diffraction (XRD) was carried out on a Phillips X'Pert-Pro diffractometer equipped with a Cu Ka source at 45 kV and 40 mA. The Fourier transformed infrared (FTIR) spectrum was obtained using a Nicolet 6700 FT-IR Spectrometer at the wavenumber range of 400 to 3000 cm^{-1}. Raman spectra were acquired using an NT-MDT NTEGRA spectrum with a 532 nm laser beam. Thermogravimetric analysis (TGA) were carried out under an air atmosphere using a Perkin Elmer Thermal Analyzer at a heating rate of 5°C min^{-1}. AFM images were collected in the tapping mode on a Dimension ICON instrument from Veeco.

55

Electrochemical tests

The rotating disk electrode (RDE) setup was purchased from Pine instruments, LLC. A conventional, three-compartment electrochemical cell comprising a saturated double junction Ag/AgCl electrode as the reference electrode, and a platinum coil as the counter electrode were used for all the EC tests. All potentials in this work are reported in reference to the reference hydrogen electrode (RHE).

Oxygen Reduction Reaction (ORR) tests

A glassy carbon RDE with a diameter of 5 mm was used as the working electrode, 1 M KOH solution was used as the electrolyte. 20% Pt/C from BASF was used as the standard catalyst for all comparisons. For preparing the working electrode, 2 mg of the synthesized hybrid NCs (HNCs) after the above-mentioned post-treatments were suspended in 0.5 mL ethanol and 25 μL of 5 wt% Nafion solution (Sigma-Aldrich, density 0.874 g·mL^{-1}) *via* 30 min of ultrasonication. Thereafter, 25 μL of the prepared catalyst ink was coated on the RDE where the catalyst loading density was calculated to be ~30 μg·cm^{-2}. For all ORR experiments, stable voltammogram curves were recorded after scanning for 15 cycles in the corresponding potential region. The dynamics of the electron transfer process in ORR were analyzed through the rotating disk voltammetry (RDV) at different speeds based on the Koutecky–Levich (KL) equation:

$$\frac{1}{J} = \frac{1}{J_K} + \frac{1}{J_L} = \frac{1}{J_K} + \frac{1}{B\omega^{\frac{1}{2}}}$$

$$B = 0.62nFC_0D_0^{2/3}v^{-1/6}$$

Where J, J_K, and J_L are the measured, kinetic and diffusion limiting current densities respectively, n is the electron transfer number, F is the Faraday constant, C_0 and D_0 are the dissolved O_2 concentration the O_2 diffusion coefficient in the electrolyte respectively, v is the kinematic viscosity of the electrolyte, ω is the angular rotation of the electrode and B is the

Levich constant. All Tafel plots were generated using the kinetic current J_K as determined from:

$$J_K = \frac{J \times J_L}{J_L - J}$$

Supercapacitance measurements

The working electrode was prepared from the desired mixture of the Co_3O_4/rGO and/or Co_3O_4/NGO HNC samples (after post-treatments), acetylene black (Cabot), and polyvinylidene difluoride (PVDF, Aldrich) blend with a weight ratio of 8:1:1. The electrodes were fabricated by loading the blend onto the surface of nickel foam sheets, drying at 80°C for 8 hrs, and pressing under 10 MPa for 5 s. The typical mass loading of the electrode active material was about ~3-5 mg. 6 M KOH solution was used as the electrolyte. Cyclic voltammetry (CV) measurements were conducted in a potential window of -0.15−0.35 V at the scanning rate of 20 mV/s. The charge−discharge tests were carried out at different current densities over a potential range of -0.1 to 0.35 V. Electrochemical impedance spectroscopy (EIS) was carried out on the same electrochemistry workstation in the frequency range from 0.05 Hz to 100 kHz for an open-circuit potential with 5 mV as the amplitude potential. The specific capacitance was calculated from the following equation:

$$C = \frac{I \times \Delta t}{\Delta V \times m} (Fg^{-1})$$

Where C is the specific capacitance, I is the current density during discharging, m is the weight loading of the electroactive material.

Results and discussion

The GO flakes synthesized via the improved Hummer's method presented lateral dimensions of ~1 μm, as shown in both AFM and SEM images in Fig. 4.2.a and 4.2c respectively. The height profile in Fig. 4.2b for the corresponding cross-section (marked

as the red line in Fig. 4.2a) indicates the average flake thickness to be ~1 nm that corresponds to 2-3 GO layers. Fig. 4.2d reveals a uniform dispersion for the as-synthesized GO flakes in the aqueous suspension, which aggregates instantly after the LASiS process (Fig. 4.2e) and in turn easily precipitates upon centrifugation (Fig. 4.2f). Such aggregation arises largely due to the oppositely charged surfaces for the Co/CoO_x NPs and GO flakes, as seen from the zeta potential measurements shown in Fig. 4.3.

Specifically, the Co/CoO_x NPs from LASiS carry net effective positive charges in the Stern layer (a positive zeta potential of ~+32 mV), while the GO flakes carry net effective negative Stern layer charges (a negative zeta potential of ~-55 mV). Hence, the two species quickly attract each other during the LASiS step to neutralize the interfacial charges and in turn, form fluffy aggregates due to lack of charge stabilization. It needs to be borne in mind that the zeta potentials for both pure GO flakes and CoO_x NPs being >+30 mV and <-30 mV respectively allow for the electrostatic stabilization of their respective aqueous suspensions. In order to make better electrochemical supporting materials, the conductivity of the GO sheets in the as-synthesised CoO_x/GO nanocomposites are improved via two different reduction processes namely, 1) direct heating at 250°C, and 2) nitrogen-doping (N-doping) to generate rGO and NGO respectively as the supporting matrices for the various Co_3O_4 nanostructures (as described in detail in the experimental section).

It needs to be mentioned here that the initial products from LASiS on Co are the metastable CoO and/or $Co(OH)_2$ crystals, both of which transform into Co_3O_4 NPs as the final product upon aging or heating as also noted in earlier works.[45] The SEM and TEM images in Fig. 4.4a-e indicate the various morphologies for the Co_3O_4/rGO HNCs made from the direct heating routes. For the pH7 case, Fig 4.4a,b indicates the formation of uniformly distributed NPs in GO sheets. Here, the crystalline structures from electron diffraction pattern (inset in Fig. 4.4b) and lattice fringes from high-resolution TEM (HRTEM) images (Fig. 4.4c) confirm the NPs to be Co_3O_4. In contrast, for the pH13 case, Fig. 4.4d-f indicate the formation of a mixture of Co_3O_4 NPs and nanorods (NRs) uniformly distributed on rGO matrices (also indicated by the inset in Fig. 4.4e). Such formation of Co_3O_4 NRs is attributed to the breakdown of $Co(OH)_2$ hexagonal single crystals, as discussed in detail in previous works[45]. Besides, the EDX mappings in Fig. 4.4g-j for the Co_3O_4 NP/rGO HNC
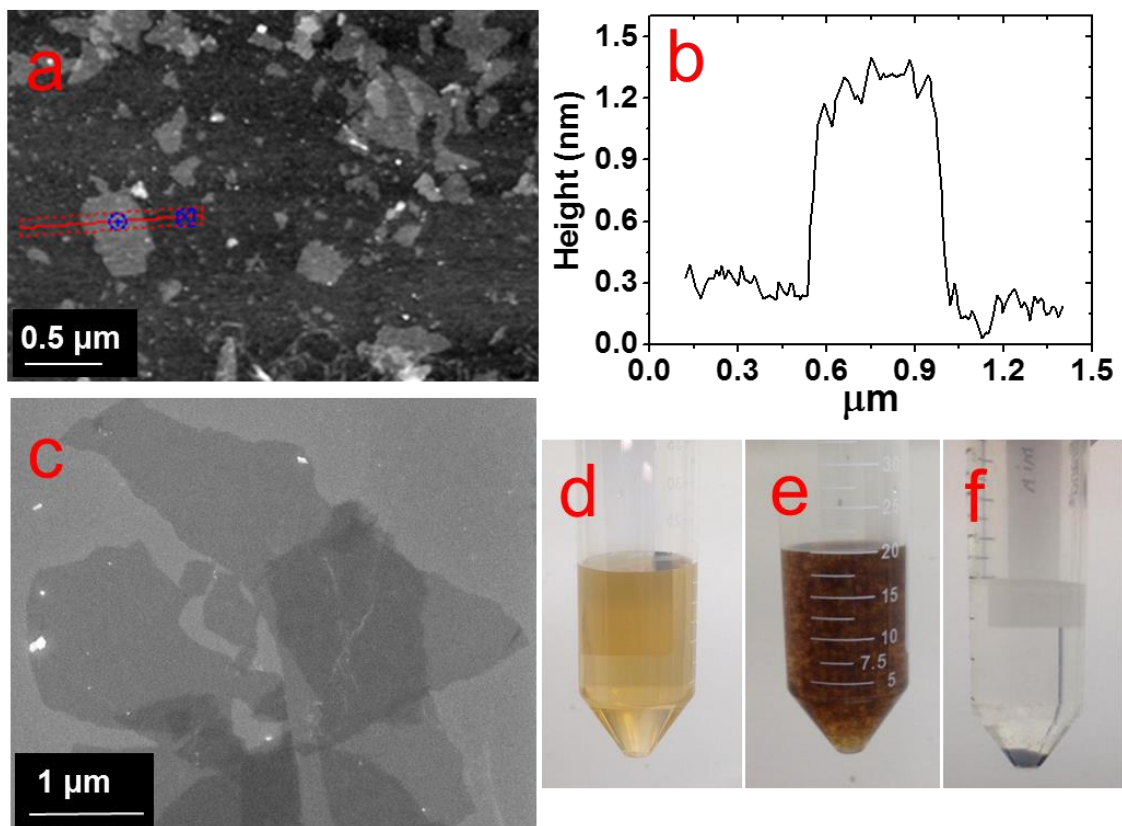
Figure 4.2. AFM (a) and SEM (c) images of GO flakes prepared by improved Hummer's method. (b) height profile of one flake across the red line marked in (a); Pictures of (d) Pure GO suspension, (e) NP/rGO suspension right after LASiS, and (f) Sample (e) after centrifugation.
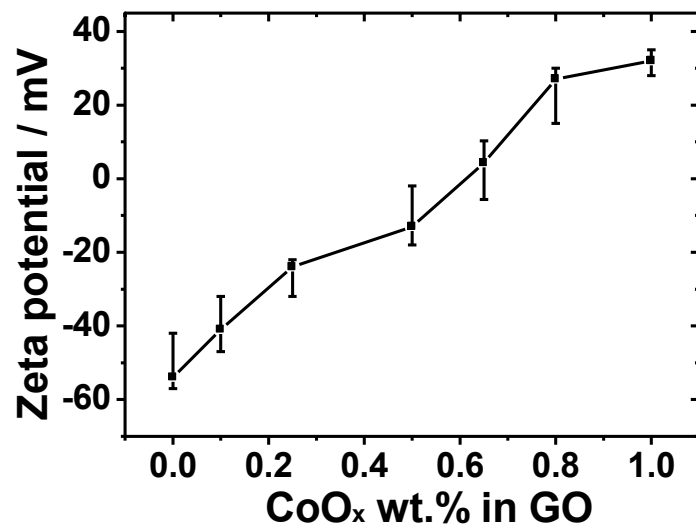
Figure 4.3. Zeta potential measurement for the nanocomposites of CoO_x and GO at different ratios.
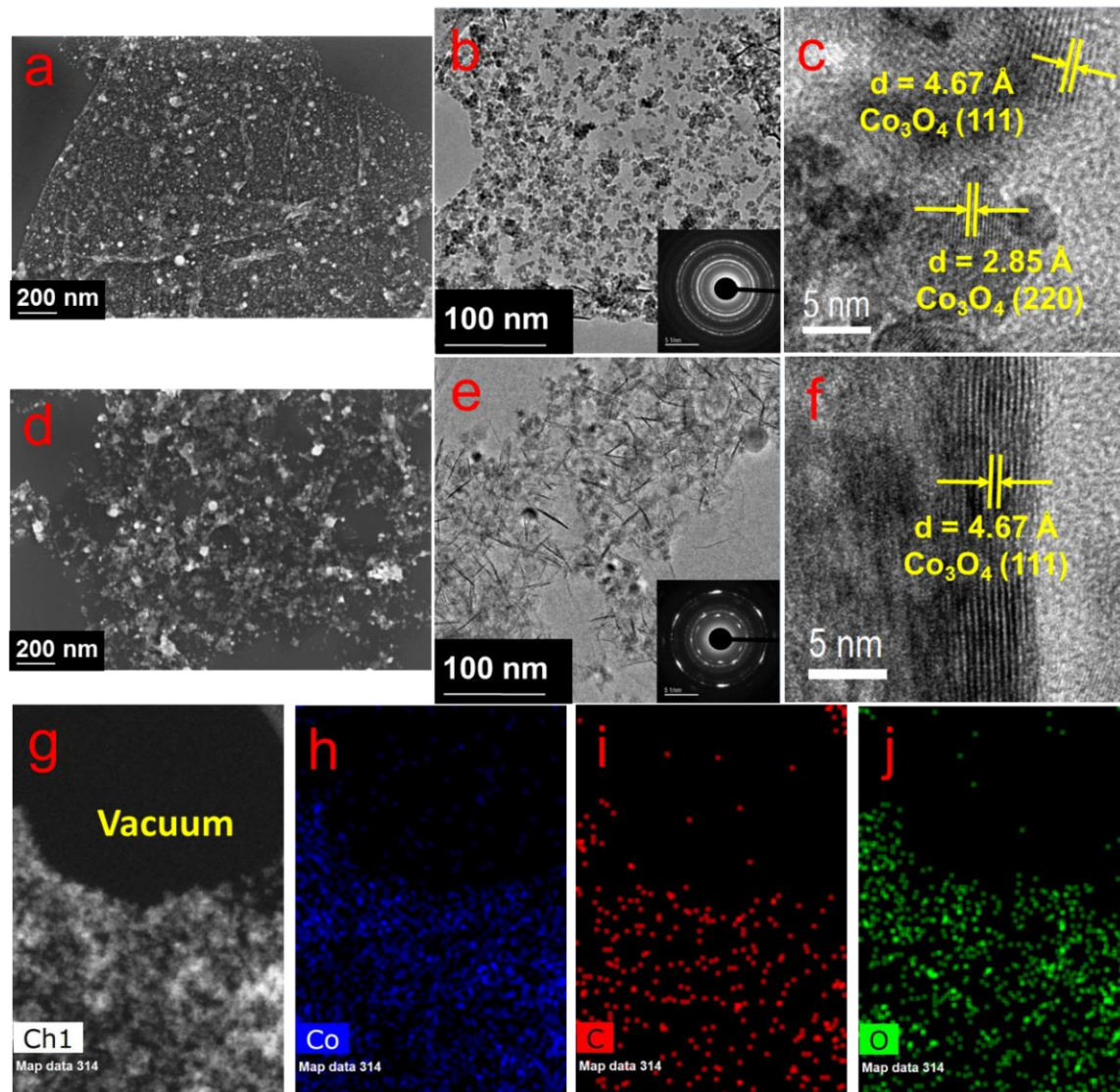
Figure 4.4. SEM (a,d) and TEM/HRTEM (b,c,e,f) images for the Co_3O_4 NP/rGO HNCs prepared at pH7 (a,b,c) and Co_3O_4 NR/rGO HNCs prepared at pH13 (b,e,f) conditions. The insets in (b,e) reveal the corresponding SAED patterns. (g-j) STEM image of the Co_3O_4 NP/rGO sample prepared at pH7 (g) and the corresponding EDX mappings for Co (h), C (i) and O (j) elements.

samples further confirm the even distribution of each element/species in the HNCs. In the second reduction route, the N-doping procedure (as detailed in experimental section) on the CoO_x/GO samples made from LASiS at pH7 conditions generates NH_3 molecules that quickly react with surface functional groups on the GO and consequently induce the formation of Co_3O_4/NGO HNCs.

Specifically, in this case, it is clearly observed from Fig. 4.5a-c that during the N-doping process, some of the spherical CoO NPs get structurally re-arranged into Co_3O_4 nanocubes indicating relatively less agglomeration. These observations are attributed to the possible spatial confinement of the NPs within ~5-6 layers of the NGO, as seen from HRTEM images in Figs.4.5 b-c, that re-distributes the surface energy during the crystalline growth of the Co_3O_4 NPs. Such spatial confinements from few layers of graphitic shells have also been reported by previous literature[192]. Meanwhile, it should also be pointed out that in this case the NPs show a relatively poorer coverage on NGO (Fig. 4.5a) as compared to the surface coverage for the Co_3O_4/rGO HNCs. For ease of understanding, from here onwards, the aforementioned three products will be referred as NP/rGO (pH7), NR/rGO (pH13) and NP/NGO (pH7, N-doping) respectively. The weight ratios of Co_3O_4:C were estimated from Q-LIBS measurements and confirmed by ICP-OES to be 3:1 for both NP/rGO and NP/NGO, and 3:2 for NR/rGO.

In terms of crystallographic information, the XRD patterns for the various HNC products under study are shown in Fig. 4.6. The pure GO exhibits a distinct peak at ~12°, which corresponds to GO (002) and implies an interlayer spacing of about 0.76 nm, while the two small peaks at ~34° and 45° are due to trace amounts of impurities. The absence of the GO (002) peak after the incorporation of Co_3O_4 nanostructures (NPs/NRs) suggest a disruption of the GO lattice stacking as well as partial reduction during the reaction with seeding Co NPs. After the N-doping process, a broad peak located at ~25° is exhibited for the NP/NGO sample, suggesting a successful reduction of GO. The NP/rGO samples before heating (NP/rGO-RT) indicate very weak peaks for $Co(OH)_2$ (001) at ~19°, which quickly disappears after calcination at 250℃ (NP/rGO-250) due to the relative instability of $Co(OH)_2$ at high temperatures.

Similar phenomenon is also observed for the NR/rGO samples, except that a $Co(OH)_2$
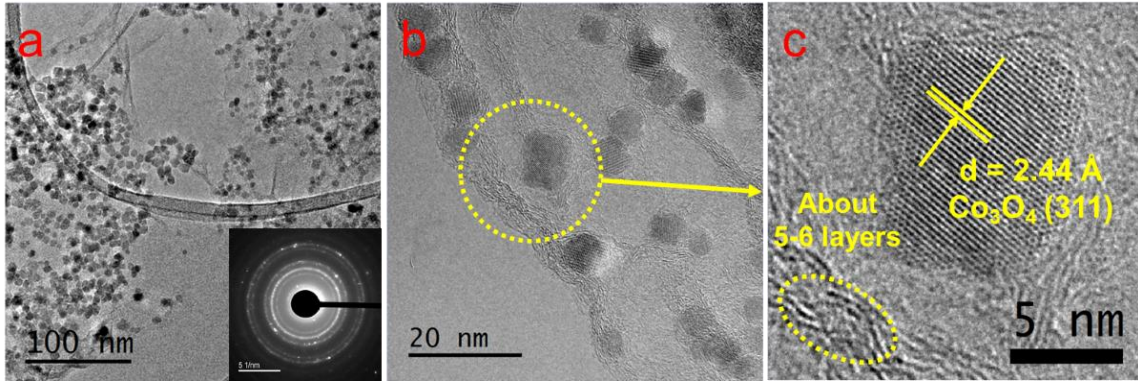
Figure 4.5. TEM (a) and HRTEM (b,c) images of the Co_3O_4 NP/NGO HNCs. The inset in (a) reveals the corresponding SAED patterns.
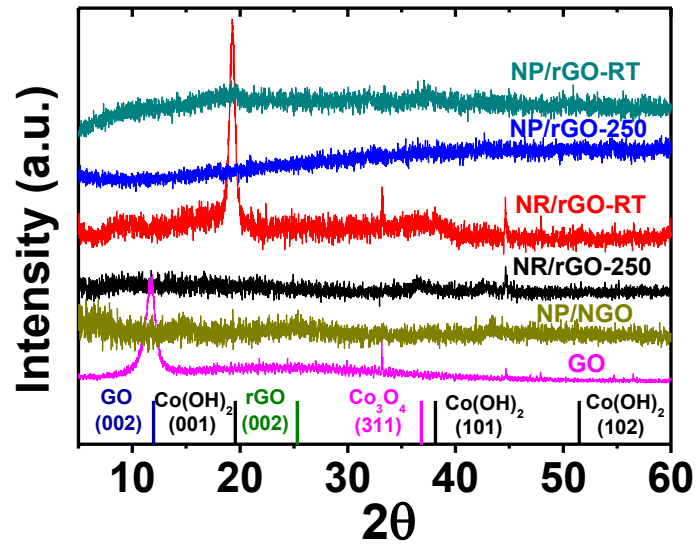
Figure 4.6. Comparison of XRD patterns for various HNC samples under study. The standard peak position for each species is shown by the vertical lines at the bottom.

(001) peak appears before the heating (NR/rGO-RT). This is clearly attributed to the reaction between the seeding Co NPs from LASiS and the concentrated solution phase OH$^-$ from the alkaline conditions (pH13). The transformation of these metastable $Co(OH)_2$ nanocrystals into Co_3O_4 under alkaline conditions lead to their selective crystalline growth as nanorods. In consequence, the emergence of a Co_3O_4 (311) peak is seen after heating the samples to 250°C (NR/rGO-250). These observations have also been reported and explained in details in earlier works.[45] Finally, it is worth to mention that neither NP/rGO nor NP/NGO samples show any Co_3O_4 peaks in the XRD pattern due to the relatively small NP sizes as well as the weak crystallization processes, which is as a result of the non-equilibrium ultrafast quenching of the laser-induced plasma plume in water where the NPs are generated.

Interfacial characterization

In this section, the formations of rGO/NGO and Co_3O_4 in the aforementioned HNC samples along with their interfaces are further investigated by FTIR and Raman spectroscopy. The FTIR spectra of NP/rGO and NR/rGO at different heating temperatures are recorded in Fig. 4.7a and 4.7b respectively. Both as-synthesized samples (RT case) exhibit a broad peak at ~3400 cm^{-1} that correspond to the O-H stretching vibration, along with several sharp peaks located at 1650 cm^{-1}, 1391 cm^{-1} 1250 cm^{-1}, 1060 cm^{-1} representing C=C, COOH, C-O-C and C-O bonding respectively.[34,42,65] The last two peaks located at lower wavenumbers, i.e., 665 and 570 cm^{-1} are assigned to the stretching vibration of Co^{3+}-O and Co^{2+}-O bonds.[34,42,65] Upon heating (150°C and 250°C cases), the O-H, COOH and C-O peaks disappear, while the C=C peak is found to shift to a lower wavenumber of ~1610 cm^{-1}, and a small C-O-C peak starts to emerge at 1060 cm^{-1}. Such observations indicate and confirm the thermal reduction of GO. The Co-O peaks, however, indicate a successive reduction of the 665 and 570 cm^{-1} stretching peaks along with the formation of a tail at ~500 cm^{-1} after the heating, which is possibly due to the solid phase reaction between Co/CoO and GO that forms a more complex structure. For the sake of comparison, a second set of HNC sample was prepared by carrying out LASiS on Co in water first, followed by heating the solution overnight until CoO_x gets fully oxidized into Co_3O_4, and then
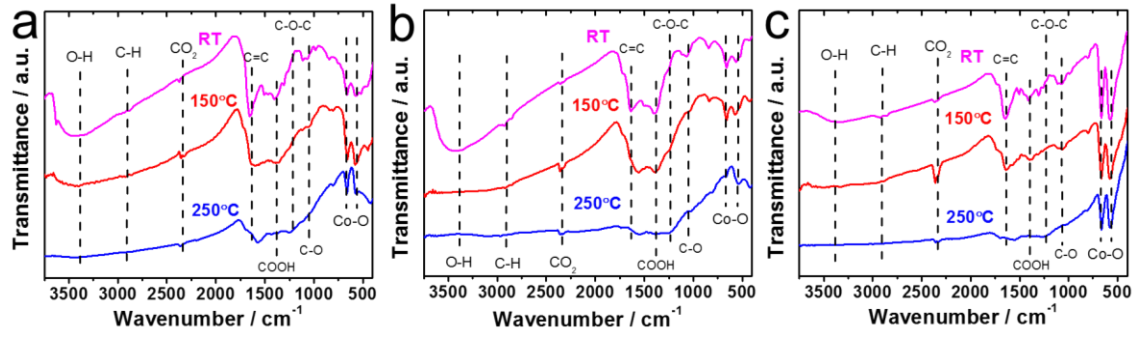
Figure 4.7. FTIR results for (a) NP/rGO, (b) NR/rGO, and (c) physically mixed HNCs heated to different temperatures.

physically mixing it with GO at the same Co_3O_4:GO weight ratio as the NP/rGO sample (3:1). With this technique, no chemical reaction occurs between Co_3O_4 and GO. The FTIR result for this sample is shown in Fig. 4.7c. Clearly, much stronger peaks for the Co-O bonding is seen with no tail after heating, suggesting that the Co_3O_4 NPs are only physically absorbed onto GO. This confirms the earlier hypothesis regarding the possible reactions between Co/CoO and GO during both the LASiS step and the subsequent vacuum heating that result in the formation of more complex Co-rGO structures exhibiting lower intensities for the Co-O stretching.

The Raman spectra in Fig. 4.8a for all the Co_3O_4-containing HNC samples detect the four distinct peaks at 677, 517, 470 and 193 cm^{-1} that correspond to the A_{1g} and F_{2g} modes of Co_3O_4.[37,66,67] Alternately, all the GO-containing HNC samples exhibit two broad peaks at 1351 and 1604 cm^{-1} that are assigned to the carbon D band and G band vibrations for GO. Specifically, the D peak is related to the mode of the k-point phonons of A_{1g} symmetry while the G peak corresponds to the E_{2g} phonon of C_{sp2} atoms.[34,36,42] The D/G intensity ratios (I_D/I_G) for all the HNC samples were calculated and summarized in Fig. 4.8b, where a high value indicates better exfoliation[137], more disorder/defects[196] and reduced oxygenated functional groups[175]. It is clearly seen that both thermal reduction and N-doping effectively increases the I_D/I_G, with the NP/NGO sample showing the highest value of 1.16.

Functional characterization

Two types of electrochemical properties, namely, ORR electrocatalytic activity and supercapacitive property are evaluated and compared for the as-synthesized HNCs. The ORR polarization curves in Fig. 4.9a indicates that the NP/NGO HNC exhibits the best ORR activity among all the samples in terms of the onset potential and diffusion-limited current, followed by the NP/rGO, Co_3O_4/C, and NR/rGO samples. Specifically, the onset potential and diffusion-limited current for NP/NGO HNCs (-0.15 V vs. SHE, and -5 mA/cm^2 respectively) are very close to the corresponding values for commercial Pt/C ORR catalysts (-0.08 V vs. SHE, and -5.6 mA/cm^2). Furthermore, the Tafel plots in Fig. 4.9b for the kinetic-diffusion region of the ORR polarization curves indicate the Tafel slope for
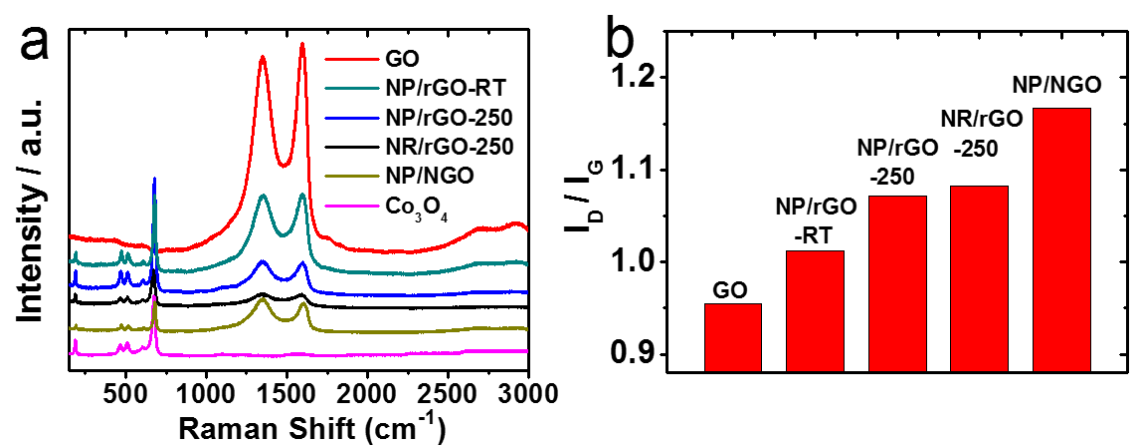
Figure 4.8. (a) Raman spectra of the as-synthesized products; **(b)** the fitting results of the intensity ratios of D-band (~1350 cm^{-1}) to G-band (~1650 cm^{-1}) from (a).

NP/NGO samples (~45 mv/dec) to be even lower than that for Pt/C (48 mv/dec) samples. This suggests a faster charge transfer rate for the ORR kinetics of the NP/NGO HNC samples. Typical Koutecky-Levich plots extracted from rotating disk voltammograms at different rotation speeds, as shown in Fig. 4.9c and the inset enable quantification of electron transfer numbers for the ORR catalysis by the NP/NGO HNCs. The results clearly indicate a near four electron transport process in the mixed kinetic-diffusion region with the potential ranging from -0.29 V to -0.37 V. Finally, the NP/NGO HNC electrocatalyst is also found to be more stable than the Pt/C. As shown in Fig. 4.9d, the chronoamperometry test run for 10000s at -0.25 V indicate negligible changes in the current density for the NP/NGO samples, whereas the standard Pt/C samples sees a dramatic decline by ~16% from the starting point value. The superior ORR activity for NP/NGO can be attributed to the N-doping process that endows NGO with ultrahigh electron mobility along with less agglomerated Co_3O_4 NPs that are devoid of any interfacial contaminants from surfactants/ligand, thereby providing a larger electroactive surface area.

$$Co_3O_4 + H_2O + OH^- \Leftrightarrow 3CoOOH + e^-$$

$$CoOOH + OH^- \Leftrightarrow CoO_2 + H_2O + e^-$$
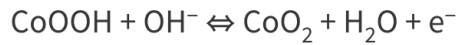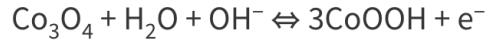
Fig. 4.10b reveals the discharge curves at 1A/g from -0.1 to 0.35 V for various samples under study. All HNCs exhibit longer discharge time, i.e., better capacitive performance than both pure Co_3O_4 (159 F/g) and rGO (68.4 F/g), with NR/rGO showing the largest capacitance of 269 F/g, followed by NP/NGO (213 F/g) and NP/rGO (196 F/g). Fig. 4.10c illustrates the complete charge-discharge curves for NR/rGO at different scan rates. The curves are found to be symmetrical which exhibit the typical characteristics for an ideal supercapacitor.

Finally, in terms of the the electrode-electrolyte interface properties, the characterizations via EIS measurements (see experimental section) with the resultant Nyquist plots shown in Fig. 4.10d. At the high-frequency region, the intercept at real part (Z') denotes the intrinsic resistance of the electrode, electrolyte as well as their contact resistance (R_e).[36,38]
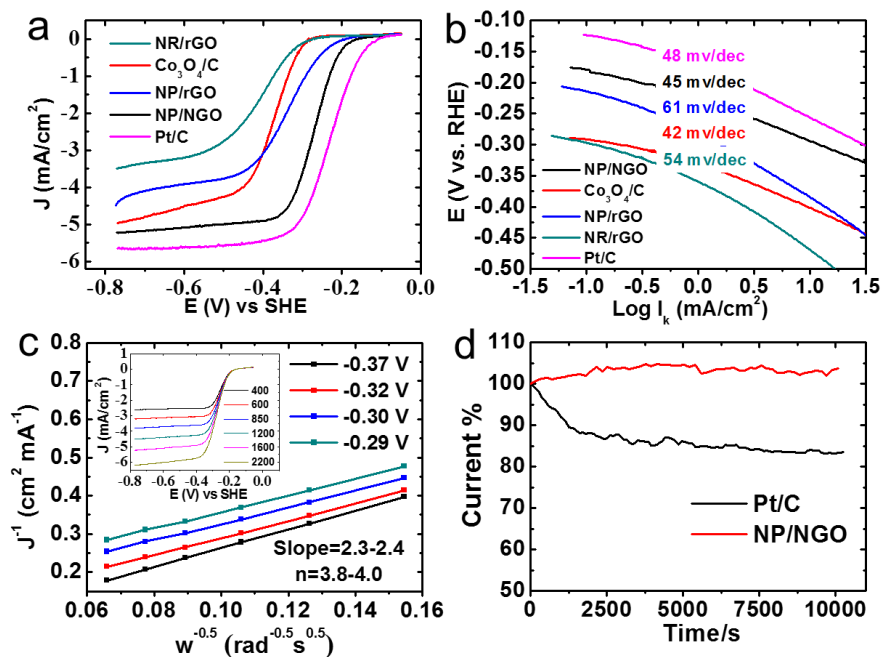
Figure 4.9. Electrochemistry data for the as-synthesized HNCs compared to standard Pt/C for ORR electrocatalytic activities using: (a) ORR polarization curves in 0.1 M KOH electrolyte saturated with dissolved O_2 at 1600 rpm and scan rate of 10 mV/s; (b) Tafel plots from (a); (c) Koutecky-Levich plots from RDV data (inset) for the NP/NGO HNC at different potentials (0.29-0.37 V) indicate four electron transport process; (e) Stability comparison for NP/NGO HNC and standard Pt/C via CA tests.
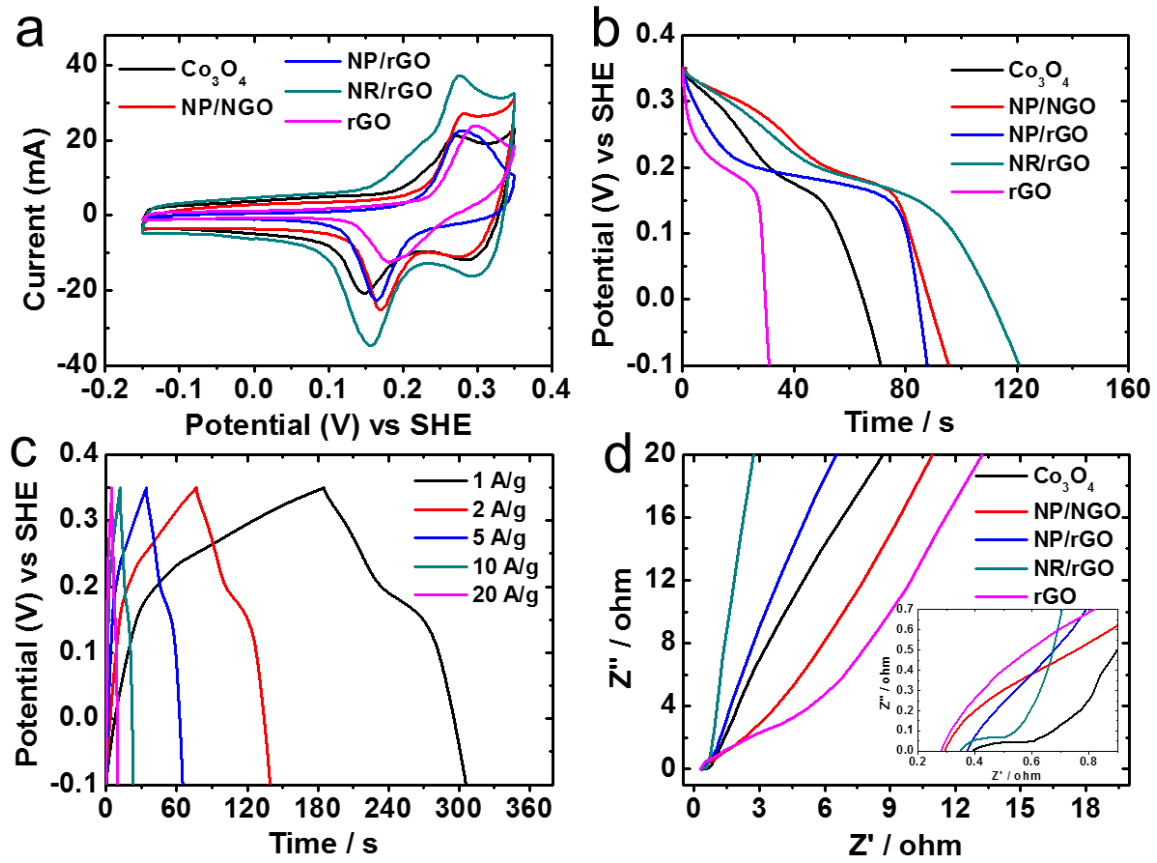
Figure 4.10. Electrochemistry data showing capacitive properties for the as-synthesized products. (a) CV scans at 20 mV/s; (b) Comparison of discharge curves at the scan rate of 1 A/g; (c) Charge-discharge curves for NR/rGO at various rates (A/g); (d) Nyquist plots

Pure Co_3O_4 is found to exhibit the largest R_e among all the samples, thereby impairing its specific capacitance. R_{ct} stands for charge-transfer resistance, which is affected by the aforementioned Faradaic reactions. NR/rGO exhibits the lowest R_{ct} of 0.37Ω, followed by Co_3O_4 (0.52Ω), NP/rGO (0.87Ω), NP/NGO (1.43Ω), and rGO (4.31Ω). The linear part of the low-frequency region of the Nyquist plot corresponds to the Warburg impedance, which represents the diffusion of electrolyte to the electrode materials. NR/rGO exhibits the most vertical slope, indicating the best electrolyte diffusion efficiency.[36,38] Thus, the better supercapacitive properties for NR/rGO, when compared to the other samples studied here, can be possibly ascribed to its interconnecting nanostructures comprising both NRs and NPs that lower the charge-transfer resistance and meanwhile promote the electrolyte diffusion rate at the interface. Qualitatively, it can be deduced from Fig. 4.10d that although NP/NGO shows the smallest R_e among all HNCs that promotes the charge transfer for ORR catalysis, the larger R_{ct} hinders their capacitive capabilities. This is probably due to the relatively poorer coverage of Co_3O_4 NPs on NGO, resulting in more NGO exposing to the surface, as demonstrated earlier in the TEM images in Fig. 4.5. In comparison NP/rGO shows the expected intermediate activities for both ORR and supercapacitance.

Synthesis-structure relations: a discussion

In general, laser ablation induces the formation of Co plasma which nucleates within the propagating cavitation bubble. Once the bubble collapses, the seeding Co NPs go through ultrasonic quenching at the liquid-bubble interface and meanwhile react with both water and GO flakes. This results in the formation of cobalt oxides embedded in GO with primary reduction. The embedding process could be both chemically and charge driven, as demonstrated earlier in the FTIR and Raman results. The initial metal products from LASiS in the alkaline condition (pH13) involve a mixture of CoO NPs, Co_3O_4 NRs and $Co(OH)_2$ hexagonal NPs, which further transform into interconnecting nanostructures comprising Co_3O_4 NPs and NRs upon thermal heating, and lead to much-enhanced supercapacitance. At pH7 condition, only CoO NPs form initially, which are found to transfer into Co_3O_4 with a more uniform distribution on rGO upon heating than through the N-doping, although with higher degree of agglomeration. The N-doping process endows the NGO with a higher

71

conductivity, meanwhile, partially reshapes the metastable CoO NPs into Co_3O_4 nanocubes with less agglomeration, therefore benefit the ORR catalytic activity.

Conclusions

In summary, three types of 0D-2D interfaced HNCs, namely, NP/rGO, NR/rGO and NP/NGO were manufactured *via* laser ablation synthesis in solution (LASiS) in tandem with two different post-treatments. The synthesized HNC samples were systematically characterized for their selective applications as ORR catalysts and/or supercapacitive materials. Detailed structural and interfacial characterizations reveal the embedment of the nanomaterials into GO to be both chemically and charge driven. Functional characterizations indicate that the NP/NGO HNC samples exhibit the best ORR activity that is comparable to the commercial Pt/C. This is ascribed to the higher electron mobility and conductivity arising from the N-doped GO (NGO) matrix along with the dispersion of isolated Co_3O_4 NPs devoid of any interfacial surfactants/ligands that provide enhanced electroactive surface areas. On the other hand, the NR/rGO samples indicate the highest supercapacitive activities resulting from interpenetrating nanostructures in the rGO matrix that benefit both charge transfer and electrolyte diffusion at the electrode interface. Finally, as expected from the aforementioned observations, the NP/rGO samples display mediocre bi-functional activities for both the applications. The ability to tune selective bi-functionalities in such tailored HNCs provide future pathways for the rational design of efficient fuel cell and/or battery electrodes from 0D–2D interfaced nanomaterials.

CHAPTER FIVE
HYBRID NANOCOMPOSITES OF NANOSTRUCTURED MANGANESE OXIDE INTERFACED WITH REDUCED GRAPHENE-OXIDE WITH ENHANCED SUPERCAPACITIVE PROPERTIES

Introduction

Despite our remarkable technological advancements throughout the past centuries, a number of critical issues still impose significant challenges, from many perspectives, for the fast development of revolutionary materials needed in our current technology-driven society. In terms of energy distribution, for instance, recent studies estimate that 11% of the current world's population still lacks access to electricity[197], revealing a precarious technology gap and its presumable serious socioeconomic consequences. In addition to that, the rapid expansion in the global population coupled with increasing urbanization processes is expected to significantly raise the global energy demand over the next decades, consequently requiring urgent materials developments as enablers for wide-scale access to efficient, reliable, yet inexpensive energy sources. To this end, renewable energy alternatives have gained tremendous attention in recent years owing to their wide availability, environmental compatibility, and especially inexhaustible power supply. However, the temporal variability inherent to many of these energy sources generally result in challenges for many of its intended applications. In this scenario, energy storage methodologies could represent an effective solution to the aforementioned concerns, potentially bridging the gap between renewable energy sources and technological progress. In this regard, faradaic supercapacitors have attracted much interest in view of their outstanding power-density along with their enhanced energy storage capacity, and yet, when compared to traditional energy storage systems, the range of application of these devices is still considered limited. To tackle these issues, many researchers have

investigated the design and application of novel functional materials as electrodes for supercapacitive systems[198]. The high theoretical specific capacitance (up to 1370 F g^{-1})[199] of Manganese Oxide (Mn_xO_y, where x = 1–3; y = 1–4) positions it as a potential candidate for the design of supercapacitors with superior performance. Additionally, when compared to commonly known high performing oxides of rare metals, such as Ruthenium oxides (RuO), Manganese is abundantly available, inexpensive and environment-friendly[200]. Graphene, on the other hand, exhibits a theoretical capacitance of 550 F g^{-1} resulting from its purely electrostatic capacitive nature[201]. But, due to its intrinsic high-conductivity, graphene can synergistically contribute to the enhancements of the capacitive properties of Mn_xO_y species by facilitating improved charge transport properties[202]. To this end, as summarized in Fig. 5.1, this chapter focuses on the use of LASiS coupled with a post-treatment for the design of hybrid nanocomposites composed of manganese-oxide dispersed onto reduced graphene-oxide (rGO) and their applications as superior electrode materials for supercapacitor devices.

Experimental procedure

Laser-based synthesis of Mn_3O_4/rGO hybrid nanocomposites

All chemicals were purchased from Sigma-Aldrich. GO suspension was prepared by following the commonly practiced improved Hummer's method[188]. Mn pellets were purchased from Kurt J. Lesker (99.95% purity, 1/4" diameter×1/4" height). LASiS experiments were carried in the experimental system previously described. Specifically, the freshly prepared GO solution with the concentration of 20 mg/L was bath-sonicated for 30 min before transferring into the LASiS reactor cell. The target metal was ablated using the unfocused 1064 nm pulsed Nd-YAG for the desired ablation time. The products were collected by centrifuging at 4700 rpm for 15 min and decanted after washing with DI-water for two times. For LASiS in alkaline conditions, KOH (99.5%) was used to adjust the solution pH to the selected alkaline condition (pH13).

Post-treatments: For the synthesis of all Mn_3O_4/rGO HNCs, the products from centrifugation were heated at 250°C under vacuum for 3 hours.
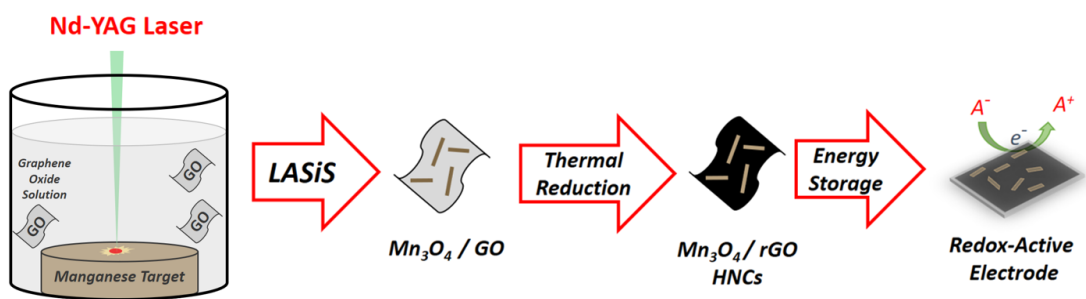
Figure 5.1. Graphical abstract of the LASiS-based hybrid nanocomposites of nanostructured manganese oxide interfaced with reduced-graphene oxide with enhanced supercapacitive properties.

Characterizations

The scanning electron microscopy (SEM) images were acquired using a Philips XL-30ESEM equipped with an energy dispersive X-ray spectroscopy. A Zetasizer (Make: Malvern; Model: nano ZS) was used for measuring zeta potentials of the colloidal solutions. X-ray diffraction (XRD) was carried out on a Phillips X'Pert-Pro diffractometer equipped with a Cu Ka source at 45 kV and 40 mA.

Electrochemical tests

The rotating disk electrode (RDE) setup was bought from Pine instrument company, LLC. A conventional, three-compartment electrochemical cell comprising of a saturated double junction Ag/AgCl electrode as the reference electrode, and a platinum coil as the counter electrode was used for all the EC tests.

Supercapacitance measurements

A 3-electrode system was used, where the working electrode was prepared from the desired mixture of the Mn_3O_4/rGO, acetylene black (Cabot), and polyvinylidene difluoride (PVDF, Aldrich) blend with a weight ratio of 8:1:1. The working electrodes were fabricated by loading the blend onto the surface of nickel foam sheets, drying at 80°C for 8 hrs, and pressing under 10 MPa for 5 s. The typical mass loading of the active electrode material was about ~3-5 mg. 0.5M Na_2So_4 solution was used as the electrolyte. Cyclic voltammetry (CV) measurements were conducted in a potential window of -0.10 to 0.90 V at the scanning rate of 20mV/s. The charge−discharge characterizations were carried out at different current densities over a potential range of -0.10 to 0.90 V. The specific capacitance was calculated from the following equation:

$$C = \frac{I \times \Delta t}{\Delta V \times m} (Fg^{-1})$$

Where C is the specific capacitance of device, I is the current density during discharging, m is the weight loading of the electroactive material in the working electrode.

Results and discussion

Structural and morphological characterizations of the LASiS-based nanocomposites

The SEM images of the products of each ablation time are depicted in Fig 5.2. These micrographs indicate the various morphologies observed in the synthesized Mn_3O_4/rGO HNCs following the direct heating post-treatment routes. In general, the images exhibited in Fig 5.2 indicate the formation of uniformly distributed nanorods throughout the rGO sheets, with a minor presence of spherical nanoparticles. The presence of 1D nanorods in the hybrid nanocomposite can be rationalized considering formation mechanisms proposed by Xiao et al during the hydrothermal synthesis route; the initially formed layered structures of δ-MnO_2 undergo a rolling mechanism, induced by the high pressure in the system, that result in rod-like seeding sites, thereby giving rise to the observed nanorods[205]. As previously discussed, considering that the nucleation phenomenon in LASiS is initiated inside the laser-induced plasma plume, the extreme pressures originating from the liquid-confinement is likely to promote the rolling of the initially formed δ-MnO_2 that give rise to the appearance rod-like seeding sites serving as the template for the growth of the Mn-rich phases. Once in solution, the Mn-rich species can undergo faradaic reactions, resulting in the formation of Mn_3O_4 as the final products. The presence of spherical NPs in Fig. 5.2 could be attributed to the secondary laser fragmentation of the metal target.

In order to further elucidate these observations, Fig 5.3 exhibits the XRD patterns of the samples obtained under 8 min ablation. The significant observation of the characteristic Mn_3O_4 diffraction patterns confirms the massive presence of these species in the synthesized composites. The other weak peak observed at $2\theta \simeq 51.2$ is attributed to the (411) plane of α-Mn, suggesting the presence of metallic Mn in the composites. The observation of metallic Mn species can be attributed to laser-induced fragmentation of the metal target; Mn species are ejected into the solution as a result of the fragmentation and further stabilized upon the formation of an oxide passivation layer on their surface, therefore preserving the metallic core.
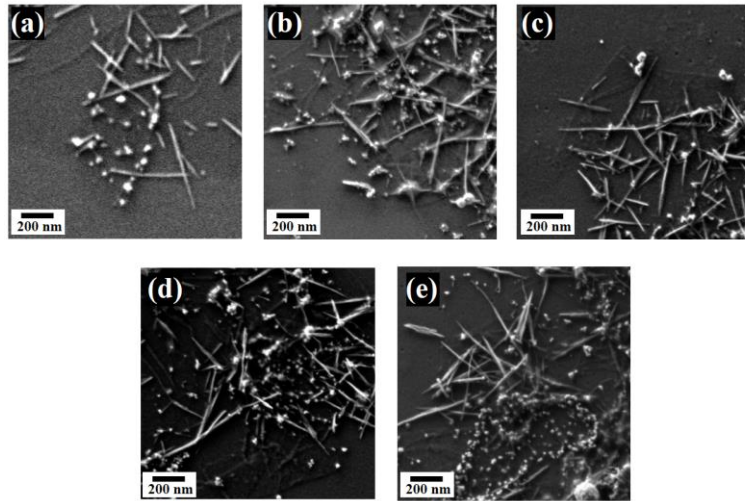
Figure 5.2. SEM images of Mn_3O_4-rGO hybrid nanocomposites prepared under (a) 6 min (b) 7 min (c) 8 min (d) 9 min and (e) 10 min ablation time
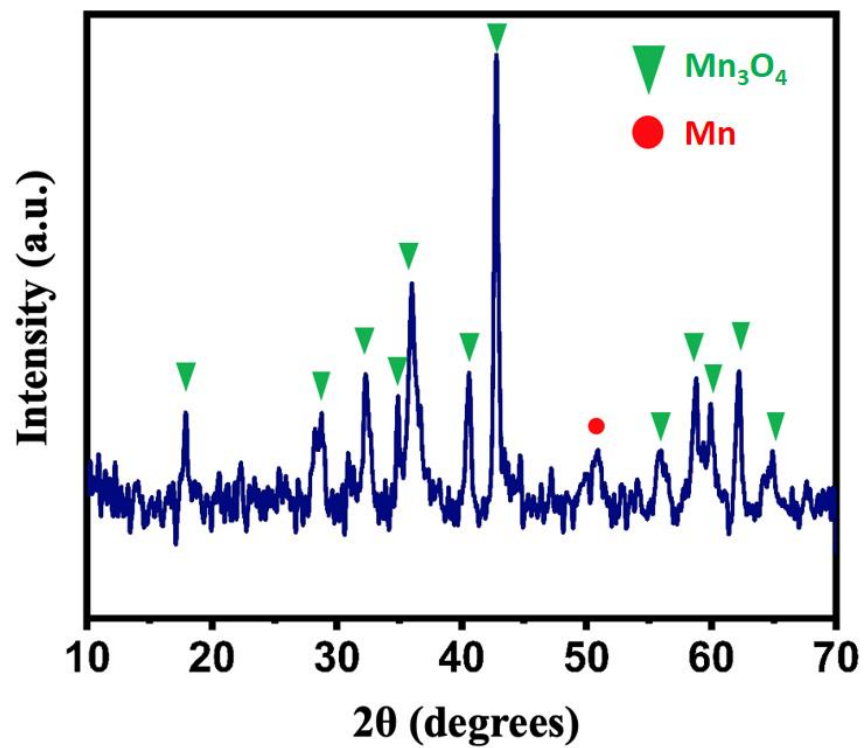
Figure 5.3. XRD pattern of the Mn_3O_4-rGO hybrid nanocomposite prepared under 8 min ablation time

Functional characterizations

In order to estimate the capacitive properties of the as-synthesized Mn_3O_4-rGO hybrid nanocomposites, cyclic voltammetry analyses were carried out at 20 mV/s from -0.1 to 0.95 V. Fig 5.4a exhibits the CV curve for the various Mn_3O_4-rGO samples made with different ablation times as different synthesis conditions. It is evident that for the composite samples made up to an ablation time of 8 mins, the capacitance values increase rapidly followed by a sharp drop in their values higher ablation times. In order to obtain a quantitative analysis, discharge curves were obtained at 2 A/g, as shown in Fig 5.4b. The discharge curves clearly exhibit longer discharge times for the composites synthesized under 7, 8 and 9 min of ablation time, and a rapid decay in the discharge times for the composites obtained under 6 and 10 min of ablation. The respective capacitance values for each of the samples, as estimated from these analyses, are plotted in Fig 5.4c that indicate good agreement with CV curves; the highest capacitance was obtained for the Mn_3O_4-rGO HNCs synthesized under 8 min (318 F/g), followed by 7 min (248 F/g), 9 min (154 F/g) and lastly 10 min (46 F/g) and (24 F/g). In fact, these results demonstrate the critical role of ablation time during LASiS in tuning the capacitive properties of these HNCs; such influence can be rationalized considering the relative density of the Mn_3O_4 phases with respect to the rGO species in the samples. A higher density of Mn_3O_4 results in an increased rate of faradaic reactions with the electrolyte that can allow more charges to be stored. However, at certain critical concentrations, the relatively low conductive nature of the oxide species is likely to compromise the charge-transfer processes through the nanocomposites, thereby hindering the redox-reaction pathways. In fact, the conductive nature arising from the presence of rGO is essential for improving the supercapacitive properties of these HNCs. The rapid charge transfer arising from the conductive sp^2 carbon network provided by the rGO nanosheets suppresses charge accumulation on the Mn_3O_4 nanorod surfaces which, in turn enhances the rate of faradic reactions and results in higher power outputs. On the other hand, the Mn_3O_4 nanorods being the redox-active species in the HCNs, the presence of such phases is directly responsible for the faradaic reactions that can promote the charge storage mechanism. To this end, it is only reasonable to assume that an optimal Mn_3O_4 to rGO ratio would ideally promote their capacitive behaviour

without compromising either the charge-transfer mechanisms or the rate of faradaic reactions – bearing in mind that both play equally important roles for architecting the supercapacitive properties of the aforesaid HNCs. Indeed, such a hypothesis is clearly corroborated by the results shown in Fig. 5.4, along with the micrographs obtained from the SEM analyses (Fig. 5.2). There is a clear correlation between the density of nanorods and ablation time in the micrographs presented in Fig 5.2; a higher amount of nanorods is observed as the ablation time increases from 6 min to 10 min. These results point toward our hypothesis that , among the evaluated ablation times, the architecture of HNCs formed under 8 min ablation comprises an optimal ratio for the relative concentrations of Mn_3O_4 to rGO species, resulting in a cooperative behaviour between faradaic and conductive effects, that might be synergistically contributing to the observed outstanding capacitive properties from the as-manufactured HNCs here. Future continued studies providing direct correlations between structure, composition and faradaic/conductive contributions from these HNC materials would tremendously benefit the directed and rational design of HNC architectures with tunable supercapacitive properties.

Conclusions

In summary, Mn_3O_4 interfaced reduced graphene-oxide were manufactured *via* laser ablation synthesis in solution (LASiS) at different ablation times (6-10 min) in tandem with a thermal post-treatment procedure. The as-synthesized HNC samples were systematically characterized for their suitability as supercapacitive materials. Detailed structural characterizations revealed that the nanomaterials embedded on to GO primarily comprised Mn_3O_4 nanorods, with minor presence of metallic Mn species. Functional characterizations demonstrated the influence of ablation time during the LASiS process on the capacitive behaviors of the HNCs via tailored optimization of the Mn_3O_4 to rGO species concentration ratios. The HNCs samples prepared under 8 min ablation exhibited the highest supercapacitive activities. We ascribe these superior activities to the interpenetrating 1-D Mn_3O_4 nanostructures in the rGO matrix that are responsible for striking a synergistic balance between faradaic activities and charge transfer properties coupled with electrolyte
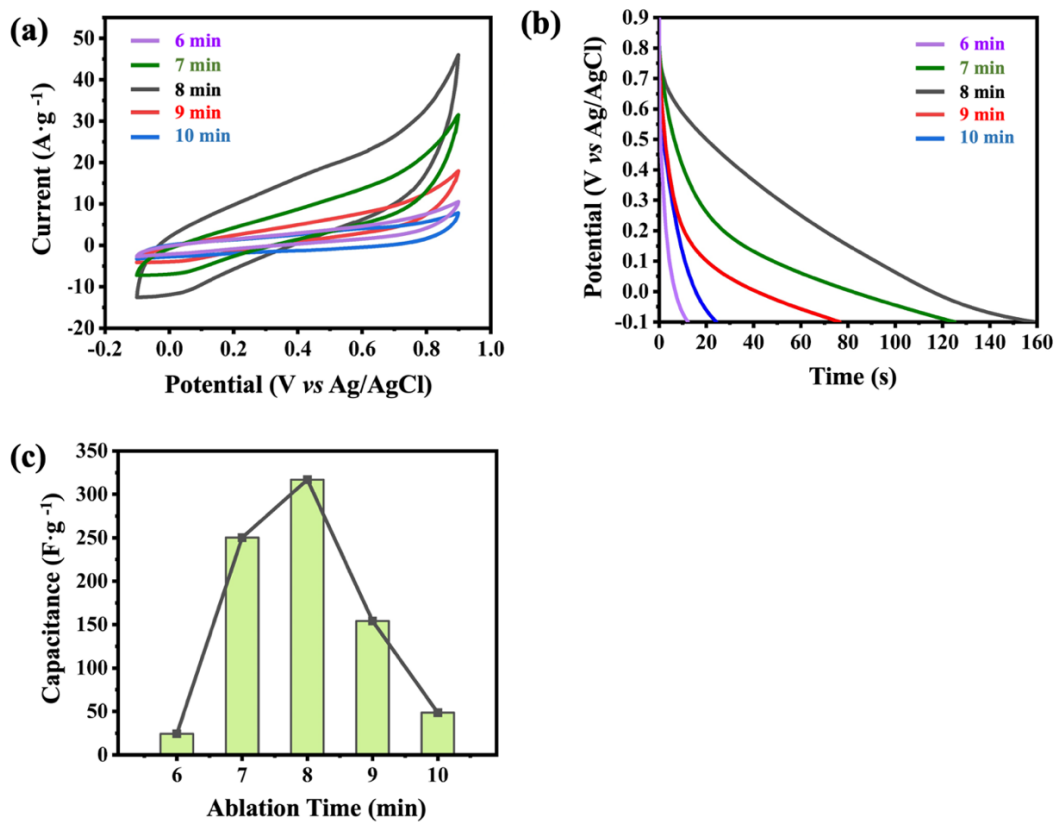
Figure 5.4. (a) CV curves for the Mn_3O_4-rGO HNCs composites in 0.5 M Na_2So_4 (b) discharge curves at 2 A/g and (c) calculated capacitance

diffusion at the electrode interfaces. The ability to tune the capacitive functionalities in such tailored HNCs demonstrates the promising potential of LASiS in the efficient and rational design and synthesis of advanced composite nanomaterials for future fabrication of electrochemical energy storage systems.

CHAPTER SIX
CONCLUSIONS AND FUTURE DIRECTIONS

Conclusions

This dissertation investigated the fabrication of functional carbon-based hybrid nanocomposites *via* Laser Ablation Synthesis in Solution (LASiS), specifically focusing on the systematic synthesis–structure–property characterizations and their relationship in the performance of these materials for applications in selected electrochemical energy storage and conversion systems, namely Oxygen Reduction Reaction (ORR) electrocatalysis and Faradaic Supercapacitive devices. The present study is based on two main synthesis routes: (1) Synthesis of Metal-Organic Frameworks (MOFs) and their functional composites, (2) fabrication of reduced (rGO)/N-doped graphene-oxide and metal-oxide hybrid nanocomposites. For each case, the analyses developed herein aimed towards the fundamental understanding regarding the role of solution-phase parameters (*e.g.*, reagents concentration and temperature) along with laser properties in driving the chemistry for the formation processes during LASiS. Furthermore, structural, elemental and morphological characterizations were systematically analyzed in order to gain a comprehensive understanding of the synthesis–structure–property relationship of the final products.

Specifically, during the LASiS-driven manufacturing of MOF structures, the Zeolitic Imidazole Frameworks (ZIF)-67 was adopted as a model system, providing the tools necessary for the systematic analysis of the role of laser parameters along with solution conditions in tailoring the size and morphology of the resulting frameworks. The findings presented in chapter two indicated that while the average MOF size is controlled by varying the organic linker, 2-methylimidazolate (Hmim), to LASiS-generated metal ion stoichiometric ratio, tailoring of its morphology occurs *via* precise control of synthesis temperature and duration of ablation. Additionally, a mechanistic picture for MOF formation *via* LASiS was presented in order to elucidate the experimental observations; the proposed sequence of reaction pathways during the

LASiS technique is initiated by high-energy laser-driven ablation of a metal target resulting in the nucleation of metal NPs that subsequently undergo solution-phase oxidation to generate Co^{2+} ions. The large population of the metal ions in the solution-phase coordinates with the active sites in the Hmim molecules, which combined to the Hmim deprotonation reactions, enable the oligomerization processes, leading to the MOF crystal nucleation and subsequent growth phenomena.

The findings arising from the LASiS-induced synthesis of ZIF-67 structures laid the ground for the application of this technique as a methodology during the fabrication of MOF-derived functional nanocomposites (NCs). More precisely, LASiS in tandem with Galvanic Replacement Reaction (LASiS-GRR) was employed along with post-processing pyrolysis treatments for the fabrication of low-Pt loading NCs comprising Pt-Co bimetallic nanoparticles encapsulated in a Co_3O_4-infused carbonaceous matrix. The results depicted in chapter three demonstrated the ability of this technique to originate a series of well-orchestrated laser-driven reaction pathways, enabling the coordination-complexation events that gave rise to the formation of Pt-Co alloyed nanoparticles embedded in well-defined ZIF-67 matrices. Subsequent systematic pyrolysis of such scaffolds led to thermal decomposition of the MOF structures, resulting in the formation of unique nano-architectures while preserving the Pt-Co alloyed nanoparticles. Detailed structural, morphological and elemental analyses revealed the formation of an interconnecting carbonaceous matrix decorated with ultra-small Co_3O_4 crystallites and dispersed Pt-Co alloyed nanoparticles, which are in turn, partially coated by a highly graphitized carbon shell. Functional characterizations revealed the outstanding ORR electrocatalytic activities of these structures in a harsh alkaline media. LASiS-based NCs obtained *via* three distinct Pt-precursor initial concentrations were evaluated as ORR electrocatalysts, demonstrating an astonishing 5-fold increase for the mass activities of NCs synthesized in 125 mg/L K_2PtCl_4 as compared to the state-of-art commercial Pt catalysts. Such remarkable performances were attributed to the electrocatalytic enhancements arising from the Pt-Co nano-alloyed configurations along with co-catalytic co-operations resulting from the unique synergistic spill-over effects facilitated by the Co_3O_4 crystallites present in the carbon matrix support.

Similarly, this dissertation explored the use of LASiS as a methodology for the design of functional hybrid nanocomposites (HNCs) characterized by nanostructured metal-oxide species interfaced with reduced and N-doped graphene oxide. Primarily, the ablation of a cobalt target was carried out in a graphene oxide (GO) solution, followed by two different post-treatments, to manufacture three types of HNCs: (1) Co_3O_4 nanoparticle (NP)/reduced graphene oxide (rGO), (2) Co_3O_4 nanorods (NR)/rGO, and (3) Co_3O_4 NP/nitrogen-doped graphene oxide (NGO). Detailed analyses based on Scanning Electron Microscopy (SEM), Transmission Electron Microscopy (TEM) and High-Resolution TEM (HRTEM), along with Energy X-ray spectroscopy (EDX) and Selected Area Electron Diffraction (SAED) of the aforementioned products revealed the ability of the LASiS technique to selectively tailor these HNCs morphology. Additionally, analysis *via* Fourier Transform Infrared (FTIR) and Raman spectroscopic studies indicated that both chemical and charge-driven interactions are partially responsible for embedding the Co_3O_4 NPs/NRs into the GO sheets. In fact, further analyses have also shown the ability to tune the functionality of the as-synthesized HNCs by tailoring their structure–property relationships. The nitrogen doping in the NP/NGO HNC samples, for instance, promotes higher electron conductivity while suppressing the aggregation between 0D CoO NPs that are partially reshaped into Co_3O_4 nanocubes due to induced surface strain energies. The results presented in chapter four demonstrated that such interfacial energetics and arrangements led to superior ORR electrocatalytic activities. On the other hand, the interconnecting 1D nanostructures in the NR/rGO HNCs enhances charge transport and electrolyte diffusion at the electrode–electrolyte interfaces, thereby promoting their supercapacitive properties.

In a similar manner, the ablation of a Mn target in a GO solution was carried out along with a thermal post-treatment to produce a series HNCs consisting of nanostructured Mn_3O_4 species interfaced with reduced graphene-oxide. Detailed structural characterizations revealed that the morphology of the embedded nanomaterials into GO sheets was primarily composed of Mn_3O_4 nanorods, with minor presence of Mn fragments. The formation of such unique architectures were attributed to the high temperature-high pressure conditions arising from the extreme interiors of the liquid-confined plasma plume during the LASiS process. Functional characterizations demonstrated the influence of the ablation time on

these HNCs capacitive properties. The different functional behaviors of the HNCs produced under different times of ablation were attributed to the relative ratio of Mn_3O_4 to rGO arising from each synthesis conditions. The relative presence of these species modulate the magnitude of faradaic and conductive properties in the resulting HNCs, consequently affecting their supercapacitive behavior. Among all the samples, the Mn_3O_4/rGO HNCs prepared under 8 min of ablation exhibited the highest supercapacitive performance, which was ascribed to the presence of the interconnecting metal-oxide 1-D nanostructures, which is closely interfaced with the rGO matrix, enabling efficient charge transfer processes, along with electrolyte diffusion at the electrode interfaces. Such ability of tailoring the capacitive functionalities through synthesis parameters demonstrates the promising role of LASiS in the efficient design of advanced materials for applications in electrochemical energy storage systems.

Proposed future work

The results from the fabrication of the HNCs based on nanostructured Co_3O_4 and Mn_3O_4 interfaced with rGO have shown the ability of LASiS to selectively tune the functionality of these HNCs by tailoring their structure–property relationships, providing future pathways for the rational design of efficient fuel cell and/or supercapacitor electrodes based on metal-oxide/carbon hybrid 0D–2D interfaced nanomaterials. For this specific synthesis route, our secondary goal is to expand the fabrication of these materials beyond laboratory-scale and evaluate their integration and performance in next-generation devices for cutting-edge engineering applications. In order to achieve that, our group has established an ongoing collaboration with the Center for Nanotechnology from the National Aeronautics and Space Administration (NASA), this initiative is part of NASA in-space-manufacturing program which aims to explore three dimensional (3D) printing technology outside of planetary atmosphere with the purpose of producing on-demand devices for future space exploration missions. Currently, NASA is concentrating efforts towards the Mars 2020 mission: a long-term effort of robotic exploration in the red planet. Nevertheless, a central issue faced in this mission is regarding the aspect of energy management; many of the energy generation

methodologies currently being considered have an intermittent nature (e.g. photovoltaics, and wind power harvesting), requiring an efficient energy storage system for their reliable utilization. To this end, this thesis focuses on applying the fundamental understanding acquired from the fabrication of the LASiS-based HNCs rGO produce an all 3-D printed solid-state faradaic supercapacitor by utilizing LASiS-produced Mn_3O_4/rGO HNCs. The selection of Mn_3O_4 as the HNC's metal oxide component, as previously discussed on chapter 5, was based on the environmental-friendly nature of this oxides along with their high active electrochemical activity, which results in high specific capacitances and their wide utilization as electrodes for supercapacitive applications.

Preliminary experiments applying a commercially available graphene / Mn_3O_4 composite as the faradaic active material have enabled the optimization of the printing parameters, including solvent-selection, ink composition and printing conditions. These initial analyses were based on two types of supercapacitors; electrochemical double-layer capacitor (EDLC) and pseudocapacitor (PsC), developed with activated carbon and graphene-Mn_3O_4 nanocomposite -based active layers, respectively. A comprehensive analysis of the optimization of the printing conditions can be found in detail in our recent publication[206]. These initial results demonstrated the ability of such end-to-end printing techniques to efficiently fabricate solid-state supercapacitors devices, including the substrate, current collector, active layers and a gel polymer electrolyte. In the future, the replacement of the commercial by the LASiS-manufactured nanocomposite is likely to enable significant enhancements in terms of performance and provide further fundamental understanding regarding the LASiS-based HNCs synthesis–structure–property relationship in these complex solid-state application systems.

LIST OF REFERENCES

1. Jeevanandam J, Barhoum A, Chan YS, Dufresne A, Danquah MK. Review on nanoparticles and nanostructured materials: history, sources, toxicity and regulations. Beilstein J Nanotechnol. 2018;9:1050-74.

2. Kolahalam LA, Kasi Viswanath IV, Diwakar BS, Govindh B, Reddy V, Murthy YLN. Review on nanomaterials: Synthesis and applications. Materials Today: Proceedings. 2019;18:2182-90.

3. Sri Abirami Saraswathi MS, Nagendran A, Rana D. Tailored polymer nanocomposite membranes based on carbon, metal oxide and silicon nanomaterials: a review. Journal of Materials Chemistry A. 2019;7(15):8723-45.

4. Burrow GM, Gaylord TK. Multi-Beam Interference Advances and Applications: Nano-Electronics, Photonic Crystals, Metamaterials, Subwavelength Structures, Optical Trapping, and Biomedical Structures. Micromachines. 2011;2(2):221-57.

5. Chen A, Chatterjee S. Nanomaterials based electrochemical sensors for biomedical applications. Chem Soc Rev. 2013;42(12):5425-38.

6. Oh W-K, Kwon OS, Jang J. Conducting Polymer Nanomaterials for Biomedical Applications: Cellular Interfacing and Biosensing. Polymer Reviews. 2013;53(3):407-42.

7. Chen X, Li C, Gratzel M, Kostecki R, Mao SS. Nanomaterials for renewable energy production and storage. Chem Soc Rev. 2012;41(23):7909-37.

8. Zhang Q, Huang JQ, Qian WZ, Zhang YY, Wei F. The road for nanomaterials industry: a review of carbon nanotube production, post-treatment, and bulk applications for composites and energy storage. Small. 2013;9(8):1237-65.

9. Zhang Q, Uchaker E, Candelaria SL, Cao G. Nanomaterials for energy conversion and storage. Chem Soc Rev. 2013;42(7):3127-71.

10. Zhao X, Sanchez BM, Dobson PJ, Grant PS. The role of nanomaterials in redox-based supercapacitors for next generation energy storage devices. Nanoscale. 2011;3(3):839-55.

11. Huang Q, Zhu Y. Printing Conductive Nanomaterials for Flexible and Stretchable Electronics: A Review of Materials, Processes, and Applications. Advanced Materials Technologies. 2019;4(5).

12. Park J, Hwang JC, Kim GG, Park JU. Flexible electronics based on one-dimensional and two-dimensional hybrid nanomaterials. InfoMat. 2019;2(1):33-56.

13. Gao K, Wang B, Tao L, Cunning BV, Zhang Z, Wang S, et al. Efficient Metal-Free Electrocatalysts from N-Doped Carbon Nanomaterials: Mono-Doping and Co-Doping. Adv Mater. 2019;31(13):e1805121.

14. Li Z, Wang L, Li Y, Feng Y, Feng W. Carbon-based functional nanomaterials: Preparation, properties and applications. Composites Science and Technology. 2019;179:10-40.

15. Zhang R-S, Jiang J-W. The art of designing carbon allotropes. Frontiers of Physics. 2018;14(1).

16. Jia D, Jiang D, Zheng Y, Tan H, Cao X, Liu F, et al. Electrochemical synthesis of NiCo layered double hydroxide nanosheets decorated on moderately oxidized graphene films for energy storage. Nanoscale. 2019;11(6):2812-22.

17. Ullah S, Hasan M, Ta HQ, Zhao L, Shi Q, Fu L, et al. Synthesis of Doped Porous 3D Graphene Structures by Chemical Vapor Deposition and Its Applications. Advanced Functional Materials. 2019;29(48).

18. Lawal AT. Graphene-based nano composites and their applications. A review. Biosens Bioelectron. 2019;141:111384.

19. Mohd Abdah MAA, Azman NHN, Kulandaivalu S, Sulaiman Y. Review of the use of transition-metal-oxide and conducting polymer-based fibres for high-performance supercapacitors. Materials & Design. 2020;186.

20. Walker JM, Akbar SA, Morris PA. Synergistic effects in gas sensing semiconducting oxide nano-heterostructures: A review. Sensors and Actuators B: Chemical. 2019;286:624-40.

21. Mavrantzas VG, Pratsinis SE. The impact of molecular simulations in gas-phase manufacture of nanomaterials. Current Opinion in Chemical Engineering. 2019;23:174-83.

22. Wu Z, Yang X, Wang Z. Size effect on the spontaneous coalescence of nanowires. Nanotechnology. 2019;30(24):245601.

23. Li T, Wang J, Wang F, Zhang L, Jiang Y, Arandiyan H, et al. The Effect of Surface Wettability and Coalescence Dynamics in Catalytic Performance and Catalyst Preparation: A Review. ChemCatChem. 2019;11(6):1576-86.

24. Kankla P, Limtrakul J, Green MLH, Chanlek N, Luksirikul P. Electrooxidation of formic acid enhanced by surfactant-free palladium nanocubes on surface modified graphene catalyst. Applied Surface Science. 2019;471:176-84.

25. Kanitz A, Kalus MR, Gurevich EL, Ostendorf A, Barcikowski S, Amans D. Review on experimental and theoretical investigations of the early stage, femtoseconds to microseconds processes during laser ablation in liquid-phase for the synthesis of colloidal nanoparticles. Plasma Sources Science and Technology. 2019;28(10).

26. Amans D, Cai W, Barcikowski S. Status and demand of research to bring laser generation of nanoparticles in liquids to maturity. Applied Surface Science. 2019;488:445-54.

27. Rafique M, Rafique MS, Kalsoom U, Afzal A, Butt SH, Usman A. Laser ablation synthesis of silver nanoparticles in water and dependence on laser nature. Optical and Quantum Electronics. 2019;51(6).

28. Dresselhaus MS, Terrones M. Carbon-Based Nanomaterials From a Historical Perspective. Proceedings of the IEEE. 2013;101(7):1522-35.

29. Kim H, Abdala AA, Macosko CW. Graphene/Polymer Nanocomposites. Macromolecules. 2010;43(16):6515-30.

30. Sharma N, Ojha H, Bharadwaj A, Pathak DP, Sharma RK. Preparation and catalytic applications of nanomaterials: a review. RSC Advances. 2015;5(66):53381-403.

31. Hu, S.; Melton, C.; Mukherjee, D., A facile route for the synthesis of nanostructured oxides and hydroxides of cobalt using laser ablation synthesis in solution (LASIS). *Physical Chemistry Chemical Physics* 2014, *16* (43), 24034-24044.

32. Hu, S.; Cheng, K. M.; Ribeiro, E. L.; Park, K.; Khomami, B.; Mukherjee, D., A facile and surfactant-free route for nanomanufacturing of tailored ternary nanoalloys as superior oxygen reduction reaction electrocatalysts. *Catalysis Science & Technology* 2017, *7* (10), 2074-2086.

33. Hu, S.; Tian, M.; Ribeiro, E. L.; Duscher, G.; Mukherjee, D., Tandem laser ablation synthesis in solution-galvanic replacement reaction (LASiS-GRR) for the production of PtCo nanoalloys as oxygen reduction electrocatalysts. *Journal of Power Sources* 2016, *306*, 413-423.

34. Hu, S.; Goenaga, G.; Melton, C.; Zawodzinski, T. A.; Mukherjee, D., PtCo/CoOx nanocomposites: Bifunctional electrocatalysts for oxygen reduction and evolution reactions synthesized via tandem laser ablation synthesis in solution-galvanic replacement reactions. *Applied Catalysis B: Environmental* 2016, *182*, 286-296.

35. Mukherjee, D.; Hu, S. Compositions, Systems and Methods for Producing Nanoalloys, and/or Nanocomposites using tandem Laser Ablation Synthesis in Solution-Galvanic Replacement Reaction. Patent No: 20170296997A1, April 19, 2016.

36. Kim BK, Sy S, Yu A, Zhang J. Electrochemical Supercapacitors for Energy Storage and Conversion. Handbook of Clean Energy Systems2015. p. 1-25.

37. Niakolas DK, Daletou M, Neophytides SG, Vayenas CG. Fuel cells are a commercially viable alternative for the production of "clean" energy. Ambio. 2016;45 Suppl 1:S32-7.

38. Dekel DR. Review of cell performance in anion exchange membrane fuel cells. Journal of Power Sources. 2018;375:158-69.

39. González A, Goikolea E, Barrena JA, Mysyk R. Review on supercapacitors: Technologies and materials. Renewable and Sustainable Energy Reviews. 2016;58:1189-206.

40. Hagesteijn KFL, Jiang S, Ladewig BP. A review of the synthesis and characterization of anion exchange membranes. Journal of Materials Science. 2018;53(16):11131-50.

41. Tammeveski K, Zagal JH. Electrocatalytic oxygen reduction on transition metal macrocyclic complexes for anion exchange membrane fuel cell application. Current Opinion in Electrochemistry. 2018;9:207-13.

42. Gülzow E. Alkaline Fuel Cells. Fuel Cells. 2004;4(4):251-5.

43. Jeon MK, Lee CH, Park GI, Kang KH. Combinatorial search for oxygen reduction reaction electrocatalysts: A review. Journal of Power Sources. 2012;216:400-8.

44. Sui S, Wang X, Zhou X, Su Y, Riffat S, Liu C-j. A comprehensive review of Pt electrocatalysts for the oxygen reduction reaction: Nanostructure, activity, mechanism and carbon support in PEM fuel cells. Journal of Materials Chemistry A. 2017;5(5):1808-25.

45. Chen Z, Higgins D, Yu A, Zhang L, Zhang J. A review on non-precious metal electrocatalysts for PEM fuel cells. Energy & Environmental Science. 2011;4(9)

46. Zou C, Zhang L, Hu X, Wang Z, Wik T, Pecht M. A review of fractional-order techniques applied to lithium-ion batteries, lead-acid batteries, and supercapacitors. Journal of Power Sources. 2018;390:286-96.

47. Salanne M, Rotenberg B, Naoi K, Kaneko K, Taberna PL, Grey CP, et al. Efficient storage mechanisms for building better supercapacitors. Nature Energy. 2016;1(6).

48. Jiang Y, Liu J. Definitions of Pseudocapacitive Materials: A Brief Review. Energy & Environmental Materials. 2019;2(1):30-7.

49. Muzaffar A, Ahamed MB, Deshmukh K, Thirumalai J. A review on recent advances in hybrid supercapacitors: Design, fabrication and applications. Renewable and Sustainable Energy Reviews. 2019;101:123-45.

50. S. Iro Z. A Brief Review on Electrode Materials for Supercapacitor. International Journal of Electrochemical Science. 2016:10628-43.

51. Liu L, Zhao H, Lei Y. Review on Nanoarchitectured Current Collectors for Pseudocapacitors. Small Methods. 2019;3(8).

52. Najib S, Erdem E. Current progress achieved in novel materials for supercapacitor electrodes: mini review. Nanoscale Advances. 2019;1(8):2817-27.

53. Vangari M, Pryor T, Jiang L. Supercapacitors: Review of Materials and Fabrication Methods. Journal of Energy Engineering. 2013;139(2):72-9.

54. Zhi M, Xiang C, Li J, Li M, Wu N. Nanostructured carbon-metal oxide composite electrodes for supercapacitors: a review. Nanoscale. 2013;5(1):72-88.

55. Zhong C, Deng Y, Hu W, Qiao J, Zhang L, Zhang J. A review of electrolyte materials and compositions for electrochemical supercapacitors. Chem Soc Rev. 2015;44(21):7484-539.

56. Ferey, G., Hybrid porous solids: past, present, future. *Chem Soc Rev* 2008, *37* (1), 191-214.

57. Stavila, V.; Talin, A. A.; Allendorf, M., MOF-based electronic and opto-electronic devices. *Chemical Society Reviews* 2014, *43* (16), 5994-6010.

58. Farha, O. K.; Eryazici, I.; Jeong, N. C.; Hauser, B. G.; Wilmer, C. E.; Sarjeant, A. A.; Snurr, R. Q.; Nguyen, S. T.; Yazaydın, A. O. z. r.; Hupp, J. T., Metal–organic framework materials with ultrahigh surface areas: is the sky the limit? *Journal of the American Chemical Society* 2012, *134* (36), 15016-15021.

59. Furukawa, H.; Ko, N.; Go, Y. B.; Aratani, N.; Choi, S. B.; Choi, E.; Yazaydin, A. Ö.; Snurr, R. Q.; O'Keeffe, M.; Kim, J., Ultrahigh porosity in metal-organic frameworks. *Science* 2010, *329* (5990), 424-428.

60. Furukawa, H.; Cordova, K. E.; O'Keeffe, M.; Yaghi, O. M., The chemistry and applications of metal-organic frameworks. *Science* 2013, *341* (6149), 1230444.

61. Furukawa, H.; Yaghi, O. M., Storage of hydrogen, methane, and carbon dioxide in highly porous covalent organic frameworks for clean energy applications. *Journal of the American Chemical Society* 2009, *131* (25), 8875-8883.

62. Farrusseng, D., *Metal-organic frameworks: applications from catalysis to gas storage*. John Wiley & Sons: 2011.

63. Li, S.-L.; Xu, Q., Metal–organic frameworks as platforms for clean energy. *Energy & Environmental Science* 2013, *6* (6), 1656.

64. Farrusseng, D.; Aguado, S.; Pinel, C., Metal–organic frameworks: opportunities for catalysis. *Angewandte Chemie International Edition* 2009, *48* (41), 7502-7513.

65. Heine, J.; Müller-Buschbaum, K., Engineering metal-based luminescence in coordination polymers and metal–organic frameworks. *Chemical Society Reviews* 2013, *42* (24), 9232-9242.

66. So, M. C.; Wiederrecht, G. P.; Mondloch, J. E.; Hupp, J. T.; Farha, O. K., Metal–organic framework materials for light-harvesting and energy transfer. *Chemical Communications* 2015, *51* (17), 3501-3510.

67. Chen, B.; Yang, Z.; Zhu, Y.; Xia, Y., Zeolitic imidazolate framework materials: recent progress in synthesis and applications. *J. Mater. Chem. A* 2014, *2* (40), 16811-16831.

68. Cravillon, J.; Nayuk, R.; Springer, S.; Feldhoff, A.; Huber, K.; Wiebcke, M., Controlling Zeolitic Imidazolate Framework Nano- and Microcrystal Formation: Insight into Crystal Growth by Time-Resolved In Situ Static Light Scattering. *Chemistry of Materials* 2011, *23* (8), 2130-2141.

69. Thompson, J. A.; Blad, C. R.; Brunelli, N. A.; Lydon, M. E.; Lively, R. P.; Jones, C. W.; Nair, S., Hybrid Zeolitic Imidazolate Frameworks: Controlling Framework Porosity and Functionality by Mixed-Linker Synthesis. *Chemistry of Materials* 2012, *24* (10), 1930-1936.

70. Park, K. S.; Ni, Z.; Cote, A. P.; Choi, J. Y.; Huang, R.; Uribe-Romo, F. J.; Chae, H. K.; O'Keeffe, M.; Yaghi, O. M., Exceptional chemical and thermal stability of zeolitic imidazolate frameworks. *Proc Natl Acad Sci U S A* 2006, *103* (27), 10186-10191.

71. Kida, K.; Okita, M.; Fujita, K.; Tanaka, S.; Miyake, Y., Formation of high crystalline ZIF-8 in an aqueous solution. *CrystEngComm* 2013, *15* (9).

72. Wagia, R.; Strashnov, I.; Anderson, M. W.; Attfield, M. P., Insight and Control of the Crystal Growth of Zeolitic Imidazolate Framework ZIF-67 by Atomic Force Microscopy and Mass Spectrometry. *Crystal Growth & Design* 2018, *18* (2), 695-700.

73. Bao, Q.; Lou, Y.; Xing, T.; Chen, J., Rapid synthesis of zeolitic imidazolate framework-8 (ZIF-8) in aqueous solution via microwave irradiation. *Inorganic Chemistry Communications* 2013, *37*, 170-173.

74. Stock, N.; Biswas, S., Synthesis of metal-organic frameworks (MOFs): routes to various MOF topologies, morphologies, and composites. *Chem Rev* 2012, *112* (2), 933-69.

75. Friščić, T., Metal-Organic Frameworks: Mechanochemical Synthesis Strategies. In *Encyclopedia of Inorganic and Bioinorganic Chemistry*, 2014; pp 1-19.

76. Amendola, V.; Meneghetti, M., What controls the composition and the structure of nanomaterials generated by laser ablation in liquid solution? *Phys Chem Chem Phys* 2013, *15* (9), 3027-46.

77. Lu, G.; Li, S.; Guo, Z.; Farha, O. K.; Hauser, B. G.; Qi, X.; Wang, Y.; Wang, X.; Han, S.; Liu, X.; DuChene, J. S.; Zhang, H.; Zhang, Q.; Chen, X.; Ma, J.; Loo, S. C.; Wei, W. D.; Yang, Y.; Hupp, J. T.; Huo, F., Imparting functionality to a metal-organic framework material by controlled nanoparticle encapsulation. *Nat Chem* 2012, *4* (4), 310-6.

78. Ozturk, Z.; Filez, M.; Weckhuysen, B. M., Decoding Nucleation and Growth of Zeolitic Imidazolate Framework Thin Films with Atomic Force Microscopy and Vibrational Spectroscopy. *Chemistry* 2017, *23* (45), 10915-10924.

79. Saliba, D.; Ammar, M.; Rammal, M.; Al-Ghoul, M.; Hmadeh, M., Crystal Growth of ZIF-8, ZIF-67, and Their Mixed-Metal Derivatives. *J Am Chem Soc* 2018, *140* (5), 1812-1823.

80. LaMer, V. K.; Dinegar, R. H., Theory, Production and Mechanism of Formation of Monodispersed Hydrosols, *J. Am. Chem. Soc*., 1950, *72,* 4847–4854.

81. LaMer, V. K.; Nucleation in Phase Transitions, *Ind. Eng. Chem.* 1952, *44*, 1270–1277.

82. Sugimoto, T.; Shiba, F.; Sekiguchi, T.; Itoh, H. Spontaneous Nucleation of Monodisperse Silver Halide Particles from Homogeneous Gelatin Solution I: Silver Chloride. *Colloids Surf., A* 2000, *164*, 183−203.

83. Chu, D. B. K., et al., Nucleation and Growth Kinetics from LaMer Burst Data. *J Phys Chem A*. 2017, *121(40)*, 7511-7517.

84. Andrews J, Shabani B. Re-envisioning the role of hydrogen in a sustainable energy economy. International Journal of Hydrogen Energy. 2012;37(2):1184-203.

85. Bilan Y, Streimikiene D, Vasylieva T, Lyulyov O, Pimonenko T, Pavlyk A. Linking between Renewable Energy, CO2 Emissions, and Economic Growth: Challenges for Candidates and Potential Candidates for the EU Membership. Sustainability. 2019;11(6).

86. Zafar MW, Shahbaz M, Hou F, Sinha A. From nonrenewable to renewable energy and its impact on economic growth: The role of research & development expenditures in Asia-Pacific Economic Cooperation countries. Journal of Cleaner Production. 2019;212:1166-78.

87. Dekel DR. Review of cell performance in anion exchange membrane fuel cells. Journal of Power Sources. 2018;375:158-69.

88. Gottesfeld S, Dekel DR, Page M, Bae C, Yan Y, Zelenay P, et al. Anion exchange membrane fuel cells: Current status and remaining challenges. Journal of Power Sources. 2018;375:170-84.

89. Pan ZF, An L, Zhao TS, Tang ZK. Advances and challenges in alkaline anion exchange membrane fuel cells. Progress in Energy and Combustion Science. 2018;66:141-75.

90. Liang Z, Zheng H, Cao R. Importance of Electrocatalyst Morphology for the Oxygen Reduction Reaction. ChemElectroChem. 2019;6(10):2600-14.

91. Osmieri L, Pezzolato L, Specchia S. Recent trends on the application of PGM-free catalysts at the cathode of anion exchange membrane fuel cells. Current Opinion in Electrochemistry. 2018;9:240-56.

92. Ercolano G, Cavaliere S, Rozière J, Jones DJ. Recent developments in electrocatalyst design thrifting noble metals in fuel cells. Current Opinion in Electrochemistry. 2018;9:271-7.

93. Stamenkovic VR, Mun BS, Arenz M, Mayrhofer KJ, Lucas CA, Wang G, et al. Trends in electrocatalysis on extended and nanoscale Pt-bimetallic alloy surfaces. Nat Mater. 2007;6(3):241-7.

94. Chaikittisilp W, Ariga K, Yamauchi Y. A new family of carbon materials: synthesis of MOF-derived nanoporous carbons and their promising applications. J Mater Chem A. 2013;1(1):14-9.

95. Zhang H, Nai J, Yu L, Lou XW. Metal-Organic-Framework-Based Materials as Platforms for Renewable Energy and Environmental Applications. Joule. 2017;1(1):77-107.

96. Kirchon A, Feng L, Drake HF, Joseph EA, Zhou HC. From fundamentals to applications: a toolbox for robust and multifunctional MOF materials. Chem Soc Rev. 2018;47(23):8611-38.

97. Rocio-Bautista P, Pacheco-Fernandez I, Pasan J, Pino V. Are metal-organic frameworks able to provide a new generation of solid-phase microextraction coatings? - A review. Anal Chim Acta. 2016;939:26-41.

98. Baumann AE, Burns DA, Liu B, Thoi VS. Metal-organic framework functionalization and design strategies for advanced electrochemical energy storage devices. Communications Chemistry. 2019;2(1).

99. Dai S, You Y, Zhang S, Cai W, Xu M, Xie L, et al. In situ atomic-scale observation of oxygen-driven core-shell formation in Pt3Co nanoparticles. Nat Commun. 2017;8(1):204.

100. Dai S, Hou Y, Onoue M, Zhang S, Gao W, Yan X, et al. Revealing Surface Elemental Composition and Dynamic Processes Involved in Facet-Dependent Oxidation of Pt3Co Nanoparticles via in Situ Transmission Electron Microscopy. Nano Letters. 2017;17(8):4683-8.

101. Kharissova OV, Kharisov BI. Variations of interlayer spacing in carbon nanotubes. RSC Adv. 2014;4(58):30807-15.

102. Lindgren P, Hallis L, Hage FS, Lee MR, Parnell J, Plan A, et al. A TEM and EELS study of carbon in a melt fragment from the Gardnos impact structure. Meteoritics & Planetary Science. 2019;54(11):2698-709.

103. Menon NK, Krivanek OL. Synthesis of Electron Energy Loss Spectra for the Quantification of Detection Limits. Microscopy and Microanalysis. 2002;8(3):203-15.

104. Córdoba R, Fernández-Pacheco R, Fernández-Pacheco A, Gloter A, Magén C, Stéphan O, et al. Nanoscale chemical and structural study of Co-based FEBID structures by STEM-EELS and HRTEM. Nanoscale Research Letters. 2011;6(1):592.

105. Khan A, Ali M, Ilyas A, Naik P, Vankelecom IFJ, Gilani MA, et al. ZIF-67 filled PDMS mixed matrix membranes for recovery of ethanol via pervaporation. Separation and Purification Technology. 2018;206:50-8.

106. Aloqayli S, Ranaweera CK, Wang Z, Siam K, Kahol PK, Tripathi P, et al. Nanostructured cobalt oxide and cobalt sulfide for flexible, high performance and durable supercapacitors. Energy Storage Materials. 2017;8:68-76.

107. Qin T, Dang S, Hao J, Wang Z, Li H, Wen Y, et al. Carbon fabric supported 3D cobalt oxides/hydroxide nanosheet network as cathode for flexible all-solid-state asymmetric supercapacitor. Dalton Trans. 2018;47(33):11503-11.

108. Schwan J, Ulrich S, Batori V, Ehrhardt H, Silva SRP. Raman spectroscopy on amorphous carbon films. Journal of Applied Physics. 1996;80(1):440-7.

109. Letzel A, Gökce B, Wagener P, Ibrahimkutty S, Menzel A, Plech A, et al. Size Quenching during Laser Synthesis of Colloids Happens Already in the Vapor Phase of the Cavitation Bubble. The Journal of Physical Chemistry C. 2017;121(9):5356-65.

110. Ibrahimkutty S, Wagener P, dos Santos Rolo T, Karpov D, Menzel A, Baumbach T, et al. A hierarchical view on material formation during pulsed-laser synthesis of nanoparticles in liquid. Sci Rep. 2015;5:16313.

111. Lam J, Amans D, Chaput F, Diouf M, Ledoux G, Mary N, et al. gamma-Al2O3 nanoparticles synthesised by pulsed laser ablation in liquids: a plasma analysis. Phys Chem Chem Phys. 2014;16(3):963-73.

112. Tamura A, Matsumoto A, Fukami K, Nishi N, Sakka T. Simultaneous observation of nascent plasma and bubble induced by laser ablation in water with various pulse durations. Journal of Applied Physics. 2015;117(17).

113. Kumar B, Yadav D, Thareja RK. Growth dynamics of nanoparticles in laser produced plasma in liquid ambient. Journal of Applied Physics. 2011;110(7).

114. Ribeiro EL, Davari SA, Hu S, Mukherjee D, Khomami B. Laser-induced synthesis of ZIF-67: a facile approach for the fabrication of crystalline MOFs with tailored size and geometry. Materials Chemistry Frontiers. 2019.

115. Cacciuto A, Auer S, Frenkel D. Onset of heterogeneous crystal nucleation in colloidal suspensions. Nature. 2004;428(6981):404-6.

116. Tang J, Wang T, Sun X, Guo Y, Xue H, Guo H, et al. Effect of transition metal on catalytic graphitization of ordered mesoporous carbon and Pt/metal oxide synergistic electrocatalytic performance. Microporous and Mesoporous Materials. 2013;177:105-12.

117. Jin W, Du H, Zheng S, Xu H, Zhang Y. Comparison of the Oxygen Reduction Reaction between NaOH and KOH Solutions on a Pt Electrode: The Electrolyte-Dependent Effect. The Journal of Physical Chemistry B. 2010;114(19):6542-8.

118. Ge X, Sumboja A, Wuu D, An T, Li B, Goh FWT, et al. Oxygen Reduction in Alkaline Media: From Mechanisms to Recent Advances of Catalysts. ACS Catalysis. 2015;5(8):4643-67.

119. Molina-García MA, Rees NV. Effect of catalyst carbon supports on the oxygen reduction reaction in alkaline media: a comparative study. RSC Advances. 2016;6(97):94669-81.

120. Seo MH, Choi SM, Seo JK, Noh SH, Kim WB, Han B. The graphene-supported palladium and palladium–yttrium nanoparticles for the oxygen reduction and ethanol oxidation reactions: Experimental measurement and computational validation. Applied Catalysis B: Environmental. 2013;129:163-71.

121. Mefford JT, Kurilovich AA, Saunders J, Hardin WG, Abakumov AM, Forslund RP, et al. Decoupling the roles of carbon and metal oxides on the electrocatalytic reduction of oxygen on La1-xSrxCoO3-delta perovskite composite electrodes. Phys Chem Chem Phys. 2019;21(6):3327-38.

122. Fabbri E, Mohamed R, Levecque P, Conrad O, Kötz R, Schmidt TJ. Composite Electrode Boosts the Activity of Ba0.5Sr0.5Co0.8Fe0.2O3-δ Perovskite and Carbon toward Oxygen Reduction in Alkaline Media. ACS Catalysis. 2014;4(4):1061-70.

123. Dai L, Xue Y, Qu L, Choi HJ, Baek JB. Metal-free catalysts for oxygen reduction reaction. Chem Rev. 2015;115(11):4823-92.

124. Wang L, Zeng Z, Ma C, Xu F, Giroux M, Chi M, et al. Migration of Cobalt Species within Mixed Platinum-Cobalt Oxide Bifunctional Electrocatalysts in Alkaline Electrolytes. Journal of The Electrochemical Society. 2019;166(7):F3093-F7.

125. Khomyakov PA, Giovannetti G, Rusu PC, Brocks G, van den Brink J, Kelly PJ. First-principles study of the interaction and charge transfer between graphene and metals. Physical Review B. 2009;79(19).

126. Sharma M, Jang J-H, Shin DY, Kwon JA, Lim D-H, Choi D, et al. Work function-tailored graphene via transition metal encapsulation as a highly active and durable catalyst for the oxygen reduction reaction. Energy & Environmental Science. 2019;12(7):2200-11.

127. Zhao J, Fu N, Liu R. Graphite-Wrapped Fe Core-Shell Nanoparticles Anchored on Graphene as pH-Universal Electrocatalyst for Oxygen Reduction Reaction. ACS Appl Mater Interfaces. 2018;10(34):28509-16.

128. Mahata A, Nair AS, Pathak B. Recent advancements in Pt-nanostructure-based electrocatalysts for the oxygen reduction reaction. Catalysis Science & Technology. 2019;9(18):4835-63.

129. Wu D, Shen X, Pan Y, Yao L, Peng Z. Platinum Alloy Catalysts for Oxygen Reduction Reaction: Advances, Challenges and Perspectives. ChemNanoMat. 2019;6(1):32-41.

130. Yue Q, Zhang K, Chen X, Wang L, Zhao J, Liu J, et al. Generation of OH radicals in oxygen reduction reaction at Pt-Co nanoparticles supported on graphene in alkaline solutions. Chem Commun (Camb). 2010;46(19):3369-71.

131. Marković, N.M., Schmidt, T.J., Stamenković, V. and Ross, P.N. (2001), Oxygen Reduction Reaction on Pt and Pt Bimetallic Surfaces: A Selective Review. Fuel Cells, 1: 105-116

132. Zhao Y, Liu J, Zhao Y, Wang F. Composition-controlled synthesis of carbon-supported Pt-Co alloy nanoparticles and the origin of their ORR activity enhancement. Phys Chem Chem Phys. 2014;16(36):19298-306.

133. Lima FHB, Ticianelli EA. Oxygen electrocatalysis on ultra-thin porous coating rotating ring/disk platinum and platinum–cobalt electrodes in alkaline media.

Electrochimica Acta. 2004;49(24):4091-9. Wang L, Zeng Z, Ma C, Xu F, Giroux M, Chi M, et al. Migration of Cobalt Species within Mixed Platinum-Cobalt Oxide Bifunctional Electrocatalysts in Alkaline Electrolytes. Journal of The Electrochemical Society. 2019;166(7):F3093-F7.

134. Liao, Q. Y., Li, N., Jin, S. X., Yang, G. W. & Wang, C. X. All-Solid-State Symmetric Supercapacitor Based on Co3O4 Nanoparticles on Vertically Aligned Graphene. Acs Nano 9, 5310-5317, doi:10.1021/acsnano.5b00821 (2015).

135. Hu, S. et al. The impact of selective solvents on the evolution of structure and function in solvent annealed organic photovoltaics. RSC Advances 4, 27931-27938, doi:10.1039/c4ra02257b (2014).

136. Zhi, M., Xiang, C., Li, J., Li, M. & Wu, N. Nanostructured carbon-metal oxide composite electrodes for supercapacitors: a review. Nanoscale 5, 72-88, doi:10.1039/c2nr32040a (2013).

137. Yan, H. et al. Graphene homogeneously anchored with Ni(OH)(2) nanoparticles as advanced supercapacitor electrodes. Crystengcomm 15, 10007-10015, doi:10.1039/c3ce41361f (2013).

138. Wu, S. P. et al. Graphene-Containing Nanomaterials for Lithium-Ion Batteries. Advanced Energy Materials 5, doi:10.1002/aenm.201500400 (2015).

139. Odedairo, T. et al. Nanosheets Co3O4 Interleaved with Graphene for Highly Efficient Oxygen Reduction. Acs Applied Materials & Interfaces 7, 21373-21380, doi:10.1021/acsami.5b06063 (2015).

140. Jiang, Z. J. & Jiang, Z. Interaction Induced High Catalytic Activities of CoO Nanoparticles Grown on Nitrogen-Doped Hollow Graphene Microspheres for Oxygen Reduction and Evolution Reactions. Sci Rep 6, 27081, doi:10.1038/srep27081 (2016).

141. Li, X. L. et al. Simultaneous Nitrogen Doping and Reduction of Graphene Oxide. Journal of the American Chemical Society 131, 15939-15944, doi:10.1021/ja907098f (2009).

142. Pendashteh, A., Palma, J., Anderson, M. & Marcilla, R. NiCoMnO4 nanoparticles on N-doped graphene: Highly efficient bifunctional electrocatalyst for oxygen

reduction/evolution reactions. Applied Catalysis B-Environmental 201, 241-252, doi:10.1016/j.apcatb.2016.08.044 (2017).

143. Hou, Y. et al. An Advanced Nitrogen-Doped Graphene/Cobalt-Embedded Porous Carbon Polyhedron Hybrid for Efficient Catalysis of Oxygen Reduction and Water Splitting. Adv Funct Mater 25, 872-882, doi:10.1002/adfm.201403657 (2015).

144. Qiao, Y. et al. A modified solvothermal synthesis of porous Mn3O4 for supercapacitor with excellent rate capability and long cycle life. Journal of Alloys and Compounds 660, 416-422, doi:10.1016/j.jallcom.2015.11.163 (2016).

145. Tang, Z., Tang, C.-h. & Gong, H. A High Energy Density Asymmetric Supercapacitor from Nano-architectured Ni(OH)2/Carbon Nanotube Electrodes. Adv Funct Mater 22, 1272-1278, doi:10.1002/adfm.201102796 (2012).

146. Zhou, X. et al. Hollow Fluffy Co3O4 Cages as Efficient Electroactive Materials for Supercapacitors and Oxygen Evolution Reaction. Acs Applied Materials & Interfaces 7, 20322-20331, doi:10.1021/acsami.5b05989 (2015).

147. Yu, P., Zhang, X., Chen, Y., Ma, Y. & Qi, Z. Preparation and pseudo-capacitance of birnessite-type MnO2 nanostructures via microwave-assisted emulsion method. Materials Chemistry and Physics 118, 303-307, doi:10.1016/j.matchemphys.2009.07.057 (2009).

148. Wang, H., Yi, H., Chen, X. & Wang, X. Facile synthesis of a nano-structured nickel oxide electrode with outstanding pseudocapacitive properties. Electrochimica Acta 105, 353-361, doi:10.1016/j.electacta.2013.05.031 (2013).

149. Fisher, R. A., Watt, M. R. & Jud Ready, W. Functionalized Carbon Nanotube Supercapacitor Electrodes: A Review on Pseudocapacitive Materials. ECS Journal of Solid State Science and Technology 2, M3170-M3177, doi:10.1149/2.017310jss (2013).

150. Feng, Q. X., Li, X. G., Wang, J. & Gaskov, A. M. Reduced graphene oxide (rGO) encapsulated Co3O4 composite nanofibers for highly selective ammonia sensors. Sensors and Actuators B-Chemical 222, 864-870, doi:10.1016/j.snb.2015.09.021 (2016).

151. Zheng, Y. L., Li, P., Li, H. B. & Chen, S. H. Controllable Growth of Cobalt Oxide Nanoparticles on Reduced Graphene Oxide and its Application for Highly Sensitive Glucose Sensor. International Journal of Electrochemical Science 9, 7369-7381 (2014).

152. Liu, Y. G. et al. Mesoporous Co3O4 sheets/3D graphene networks nanohybrids for high-performance sodium-ion battery anode. Journal of Power Sources 273, 878-884, doi:10.1016/j.jpowsour.2014.09.121 (2015).Wang, L., Wang, D. L., Zhu, J. S. & Liang, X. S. Preparation of Co3O4 nanoplate/graphene sheet composites and their synergistic electrochemical performance. Ionics 19, 215-220, doi:10.1007/s11581-012-0699-7 (2013).

153. Zhou, X. Y. et al. Microwave irradiation synthesis of Co3O4 quantum dots/graphene composite as anode materials for Li-ion battery. Electrochimica Acta 143, 175-179, doi:10.1016/j.electacta.2014.08.023 (2014).

154. Liang, Y. Y. et al. Co3O4 nanocrystals on graphene as a synergistic catalyst for oxygen reduction reaction. Nature Materials 10, 780-786, doi:10.1038/nmat3087 (2011).

155. Cui, X. J. et al. Synthesis and Characterization of Iron-Nitrogen-Doped Graphene/Core-Shell Catalysts: Efficient Oxidative Dehydrogenation of N-Heterocycles. Journal of the American Chemical Society 137, 10652-10658, doi:10.1021/jacs.5b05674 (2015).

156. Kumar, K. et al. Effect of the Oxide-Carbon Heterointerface on the Activity of Co3O4/NRGO Nanocomposites toward ORR and OER. J Phys Chem C 120, 7949-7958, doi:10.1021/acs.jpcc.6b00313 (2016).

157. Lai, L. F. et al. Exploration of the active center structure of nitrogen-doped graphene-based catalysts for oxygen reduction reaction. Energy & Environmental Science 5, 7936-7942, doi:10.1039/c2ee21802j (2012).

158. Liu, T. et al. CoO nanoparticles embedded in three-dimensional nitrogen/sulfur co-doped carbon nanofiber networks as a bifunctional catalyst for oxygen reduction/evolution reactions. Carbon 106, 84-92, doi:10.1016/j.carbon.2016.05.007 (2016).

159. Sun, T. T. et al. Cobalt-nitrogen-doped ordered macro-/mesoporous carbon for highly efficient oxygen reduction reaction. Applied Catalysis B-Environmental 193, 1-8, doi:10.1016/j.apcatb.2016.04.006 (2016).

160. Li, Q., Mahmood, N., Zhu, J. H., Hou, Y. L. & Sun, S. H. Graphene and its composites with nanoparticles for electrochemical energy applications. Nano Today 9, 668-683, doi:10.1016/j.nantod.2014.09.002 (2014).

161. Wang, H.-W. et al. Preparation of reduced graphene oxide/cobalt oxide composites and their enhanced capacitive behaviors by homogeneous incorporation of reduced graphene oxide sheets in cobalt oxide matrix. Materials Chemistry and Physics 130, 672-679, doi:10.1016/j.matchemphys.2011.07.043 (2011).

162. Xu, J. M. et al. Co3O4 nanocubes homogeneously assembled on few-layer graphene for high energy density lithium-ion batteries. Journal of Power Sources 274, 816-822, doi:10.1016/j.jpowsour.2014.10.106 (2015).

163. Ke, Q., Liao, Y., Yao, S., Song, L. & Xiong, X. A three-dimensional TiO2/graphene porous composite with nano-carbon deposition for supercapacitor. Journal of Materials Science 51, 2008-2016, doi:10.1007/s10853-015-9510-2 (2016).

164. Yang, J. L. et al. LiFePO4-graphene as a superior cathode material for rechargeable lithium batteries: impact of stacked graphene and unfolded graphene. Energy & Environmental Science 6, 1521-1528, doi:10.1039/c3ee24163g (2013).

165. Nguyen, V. H. & Shim, J. J. The 3D Co3O4/graphene/nickel foam electrode with enhanced electrochemical performance for supercapacitors. Materials Letters 139, 377-381, doi:10.1016/j.matlet.2014.10.128 (2015).

166. Nguyen, T. T. et al. Facile synthesis of cobalt oxide/reduced graphene oxide composites for electrochemical capacitor and sensor applications. Solid State Sciences 53, 71-77, doi:10.1016/j.solidstatesciences.2016.01.006 (2016).

167. He, G. Y. et al. Hydrothermal preparation of Co3O4@graphene nanocomposite for supercapacitor with enhanced capacitive performance. Materials Letters 82, 61-63, doi:10.1016/j.matlet.2012.05.048 (2012).

168. Xiang, C. C., Li, M., Zhi, M. J., Manivannan, A. & Wu, N. Q. A reduced graphene oxide/Co3O4 composite for supercapacitor electrode. Journal of Power Sources 226, 65-70, doi:10.1016/j.jpowsour.2012.10.064 (2013).

169. Wang, B., Wang, Y., Park, J., Ahn, H. & Wang, G. X. In situ synthesis of Co3O4/graphene nanocomposite material for lithium-ion batteries and supercapacitors with high capacity and supercapacitance. Journal of Alloys and Compounds 509, 7778-7783, doi:10.1016/j.jallcom.2011.04.152 (2011).

170. Zou, Y. Q., Kinloch, I. A. & Dryfe, R. A. W. Mesoporous Vertical Co3O4 Nanosheet Arrays on Nitrogen-Doped Graphene Foam with Enhanced Charge-Storage Performance. Acs Applied Materials & Interfaces 7, 22831-22838, doi:10.1021/acsami.5b05095 (2015).

171. Faraji, S. & Ani, F. N. Microwave-assisted synthesis of metal oxide/hydroxide composite electrodes for high power supercapacitors - A review. Journal of Power Sources 263, 338-360, doi:10.1016/j.jpowsour.2014.03.144 (2014).

172. Wang, H. & Dai, H. Strongly coupled inorganic-nano-carbon hybrid materials for energy storage. Chemical Society Reviews 42, 3088-3113, doi:10.1039/c2cs35307e (2013).

173. Liang, D. et al. MoS2 nanosheets decorated with ultrafine Co3O4 nanoparticles for high-performance electrochemical capacitors. Electrochimica Acta 182, 376-382, doi:10.1016/j.electacta.2015.09.085 (2015).

174. Ujjain, S. K., Singh, G. & Sharma, R. K. Co3O4@Reduced Graphene Oxide Nanoribbon for high performance Asymmetric Supercapacitor. Electrochimica Acta 169, 276-282, doi:10.1016/j.electacta.2015.03.141 (2015).

175. Choi, S. M., Seo, M. H., Kim, H. J. & Kim, W. B. Synthesis and characterization of graphene-supported metal nanoparticles by impregnation method with heat treatment in H2 atmosphere. Synthetic Metals 161, 2405-2411, doi:10.1016/j.synthmet.2011.09.008 (2011).

176. Pocklanova, R. et al. Gold nanoparticle-decorated graphene oxide: Synthesis and application in oxidation reactions under benign conditions. Journal of Molecular Catalysis A: Chemical 424, 121-127, doi:10.1016/j.molcata.2016.07.047 (2016).

107

177. Li, R. Z. et al. High-rate in-plane micro-supercapacitors scribed onto photo paper using in situ femtolaser-reduced graphene oxide/Au nanoparticle microelectrodes. Energy Environ. Sci., doi:10.1039/c5ee03637b (2016).

178. Lam, J. et al. Dynamical study of bubble expansion following laser ablation in liquids. Applied Physics Letters 108, 074104, doi:10.1063/1.4942389 (2016).

179. Matsumoto, A. et al. Transfer of the Species Dissolved in a Liquid into Laser Ablation Plasma: An Approach Using Emission Spectroscopy. The Journal of Physical Chemistry C 119, 26506-26511, doi:10.1021/acs.jpcc.5b07769 (2015).

180. Liu, P., Cui, H., Wang, C. X. & Yang, G. W. From nanocrystal synthesis to functional nanostructure fabrication: laser ablation in liquid. Physical chemistry chemical physics : PCCP 12, 3942-3952, doi:10.1039/b918759f (2010).

181. Liu, X. et al. Co3O4/C nanocapsules with onion-like carbon shells as anode material for lithium ion batteries. Electrochimica Acta 100, 140-146, doi:10.1016/j.electacta.2013.03.179 (2013).

182. Zeng, H. B. et al. Nanomaterials via Laser Ablation/Irradiation in Liquid: A Review. Adv Funct Mater 22, 1333-1353 (2012).

183. Jiménez, E., Abderrafi, K., Abargues, R., Valdés, J. L. & Martínez-Pastor, J. P. Laser-ablation-induced synthesis of SiO2-capped noble metal nanoparticles in a single step. Langmuir 26, 7458-7463, doi:10.1021/la904179x (2010).

184. Scaramuzza, S., Zerbetto, M. & Amendola, V. Synthesis of Gold Nanoparticles in Liquid Environment by Laser Ablation with Geometrically Confined Configurations: Insights To Improve Size Control and Productivity. The Journal of Physical Chemistry C 120, 9453-9463, doi:10.1021/acs.jpcc.6b00161 (2016).

185. Scaramuzza, S., Agnoli, S. & Amendola, V. Metastable alloy nanoparticles, metal-oxide nanocrescents and nanoshells generated by laser ablation in liquid solution: influence of the chemical environment on structure and composition. Phys. Chem. Chem. Phys., doi:10.1039/C5CP00279F (2015).

186. Povarnitsyn, M. E., Itina, T. E., Levashov, P. R. & Khishchenko, K. V. Mechanisms of nanoparticle formation by ultra-short laser ablation of metals in liquid environment. Phys Chem Chem Phys 15, 3108, doi:10.1039/c2cp42650a (2013).

187. Semaltianos, N. G. et al. Laser ablation in water: A route to synthesize nanoparticles of titanium monoxide. Chemical Physics Letters 496, 113-116, doi:10.1016/j.cplett.2010.07.023 (2010).

188. Marcano, D. C. et al. Improved Synthesis of Graphene Oxide. ACS Nano 4, 4806-4814, doi:10.1021/nn1006368 (2010).

189. Davari, S. A.; Hu, S.; Ribeiro, E. L.; Mukherjee, D., Rapid elemental composition analysis of intermetallic ternary nanoalloys using calibration-free quantitative Laser Induced Breakdown Spectroscopy (LIBS). *MRS Advances* 2017, 1-6.

190. Davari, S. A.; Hu, S.; Mukherjee, D., Calibration-free quantitative analysis of elemental ratios in intermetallic nanoalloys and nanocomposites using Laser Induced Breakdown Spectroscopy (LIBS). *Talanta* 2017, *164*, 330-340.

191. Roy, S., Bajpai, R., Koratkar, N. & Misra, D. S. Localized transformation of few-layered graphene producing graphitic shells with nanoparticle cores for catalytic applications. Carbon 85, 406-413, doi:10.1016/j.carbon.2014.12.106 (2015).

192. Huang, S. O., Jin, Y. H. & Jia, M. Q. Preparation of graphene/Co3O4 composites by hydrothermal method and their electrochemical properties. Electrochimica Acta 95, 139-145, doi:10.1016/j.electacta.2013.01.045 (2013).

193. Sun, X. L. et al. Facile synthesis of Co3O4 with different morphologies loaded on amine modified graphene and their application in supercapacitors. Journal of Alloys and Compounds 685, 507-517, doi:10.1016/j.jallcom.2016.05.282 (2016).

194. Kim, H., Seo, D. H., Kim, S. W., Kim, J. & Kang, K. Highly reversible Co3O4/graphene hybrid anode for lithium rechargeable batteries. Carbon 49, 326-332, doi:10.1016/j.carbon.2010.09.033 (2011).

195. Saha, S. et al. Hydrothermal synthesis of Fe3O4/RGO composites and investigation of electrochemical performances for energy storage applications. Rsc Advances 4, 44777-44785, doi:10.1039/c4ra07388f (2014).

196. ESMAP. 2020. Off-grid Market Trends Report. Washington, DC: World Bank. Liu H, Liu X, Wang S, Liu H-K, Li L. Transition metal based battery-type electrodes in hybrid supercapacitors: A review. Energy Storage Materials. 2020;28:122-45.

197. Hu Y, Wu Y, Wang J. Manganese-Oxide-Based Electrode Materials for Energy Storage Applications: How Close Are We to the Theoretical Capacitance? Adv Mater. 2018;30(47):e1802569.

198. Lee H, Jin S, Yim S. Titanium oxide nanoparticle-embedded mesoporous manganese oxide microparticles for supercapacitor electrodes. Journal of Physics and Chemistry of Solids. 2020;138.

199. Cossutta M, Vretenar V, Centeno TA, Kotrusz P, McKechnie J, Pickering SJ. A comparative life cycle assessment of graphene and activated carbon in a supercapacitor application. Journal of Cleaner Production. 2020;242.

200. Jadhav S, Kalubarme RS, Terashima C, Kale BB, Godbole V, Fujishima A, et al. Manganese dioxide/ reduced graphene oxide composite an electrode material for high-performance solid state supercapacitor. Electrochimica Acta. 2019;299:34-44. Liu H, Liu X, Wang S, Liu H-K, Li L. Transition metal based battery-type electrodes in hybrid supercapacitors: A review. Energy Storage Materials. 2020;28:122-45.

201. Hu Y, Wu Y, Wang J. Manganese-Oxide-Based Electrode Materials for Energy Storage Applications: How Close Are We to the Theoretical Capacitance? Adv Mater. 2018;30(47):e1802569.

202. Lee H, Jin S, Yim S. Titanium oxide nanoparticle-embedded mesoporous manganese oxide microparticles for supercapacitor electrodes. Journal of Physics and Chemistry of Solids. 2020;138.

203. Cossutta M, Vretenar V, Centeno TA, Kotrusz P, McKechnie J, Pickering SJ. A comparative life cycle assessment of graphene and activated carbon in a supercapacitor application. Journal of Cleaner Production. 2020;242.

204. Jadhav S, Kalubarme RS, Terashima C, Kale BB, Godbole V, Fujishima A, et al. Manganese dioxide/ reduced graphene oxide composite an electrode material for high-performance solid state supercapacitor. Electrochimica Acta. 2019;299:34-44.

205. Wang, X. and Li, Y. (2003), Synthesis and Formation Mechanism of Manganese Dioxide Nanowires/Nanorods. Chemistry – A European Journal, 9: 300-306.

206. Seol M-L, Nam I, Ribeiro EL, Segel B, Lee D, Palma T, et al. All-Printed In-Plane Supercapacitors by Sequential Additive Manufacturing Process. ACS Applied Energy Materials. 2020;3(5):4965-73.

VITA

Erick Leonardo Ribeiro was born on March 21st, 1991 in Santos, Brazil. From 2006 to 2008 he attended the São Paulo State Technical School "Adolpho Berezin" where he graduated high-school with a technical certification in computer science. After graduation, Erick was awarded the ProUni - Brazilian Presidential Scholarship to attend the Chemical Engineering undergraduate program at the University Center of FEI. In 2012, Erick represented the University Center of FEI in a nation-wide competition, where he was awarded the Science Mobility Scholarship, sponsored by the Brazilian Ministry of Education, allowing him to attend the 2012-2013 academic year as an exchanged student at the University of Tennessee, Knoxville. Additionally, in 2013, as part of the Science Mobility Program, Erick served for one semester as a research assistant at the Nanomaterials in the Environment, Agriculture, and Technology Organized Research Unit (NEAT-ORU) at the University of California, Davis, where he worked under the supervision of Dr. Ricardo Castro on the development of nanostructured materials for sensing applications. In 2014, upon receiving the Bachelor of Science degree in Chemical Engineering, Erick was selected as one of the recipients of the LASPAU/CAPES Science without Borders Scholarship, receiving a 4-years long grant to pursue a doctoral degree in the United States. In the fall of 2014, Erick then joined the Chemical and Biomolecular Engineering Ph.D. program at the University of Tennessee, Knoxville to work under the supervision of Dr. Bamin Khomami. In 2018, Erick had the opportunity to serve as a graduate research fellow in the National Aeronautics and Space Administration (NASA) I^2 program, working under the conjoint supervision of Dr. Jin-Woo Han and Dr. Meyya Meyyappan on the development of nanomaterials for electronics.